Surface Mixed Layer Heat and Salinity Budget in the Central Equatorial Indian Ocean

Nan-Hsun Chi

A dissertation

submitted in partial fulfillment of the

requirements for the degree of

Doctor of Philosophy

University of Washington

2018

Reading Committee:

Ren-Chieh Lien, Chair

Eric A. D'Asaro, Co-Chair

Michael J. McPhaden

Program Authorized to Offer Degree:

School of Oceanography

University of Washington

Abstract

Surface Mixed Layer Heat and Salinity Budget in the Central Equatorial Indian Ocean

Nan-Hsun Chi

Chair of the Supervisory Committee:
Senior Scientist Ren-Chieh Lien
Senior Scientist Eric A. D'Asaro
Applied Physics Laboratory

The oceanic surface mixed layer (ML) heat and salinity budgets in the central equatorial Indian Ocean are estimated using measurements taken from two DYNAMO and two RAMA moorings during September 2011 to January 2012. The broader central to eastern tropical ML salinity (MLS) budget in boreal fall and winter between 2011 to 2015 is also evaluated using satellite and data products. The ML heat variation is mostly modulated by 1-D processes while MLS is modulated by 3-D processes at intraseasonal to seasonal time scales. During MJO active phases, ML is cooled by the net surface heat flux and the turbulent heat flux at the bottom of the ML. During MJO suppressed phases, ML is heated by the net surface heat flux. MLS does not vary greatly between different phases of MJOs since 1-D processes largely compensate each other and leaves the MLS increasing by horizontal advection. A barrier layer exerts control on the turbulent fluxes. This study provides a new measure of barrier layer strength by a "barrier layer

potential energy (BLPE)," which depends on the thickness of the barrier layer, the thickness of the ML, and the density stratification across the isothermal layer. In boreal fall the MLS increases due to horizontal advection and turbulent mixing, yet the precipitation that often associated with MJOs events freshens the MLS. In boreal winter the mooring MLS decreases due to zonal advection and precipitation at the equator, and by meridional advection and precipitation at 1.5°S. The MLS budget estimated using multi-year satellite and data products yields qualitatively consistent results as that computed using mooring measurements. The maximal increase (decrease) of MLS at central and eastern equatorial Indian Ocean resembles the eastward development (westward retreat) of the equatorial salty tongue in boreal fall (winter). The horizontal advection acts to transport spicier, i.e., warmer and saltier, water mass from the northwest. The vertical cooling dominates the ML heat budget so that the ML becomes cooler and saltier and therefore denser. The advective and turbulent fluxes at the base of ML vary greatly in the central equatorial Indian Ocean at O (100 km) horizontal scales, and between different phases of MJOs and seasons, suggesting the important and complicated roles of oceanic processes in the surface ML heat and salinity budgets. Therefore, models should properly estimate the oceanic BLPE, background shear and surface forcing for ML heat variation, and the strength and timing of the equatorial currents as well as the salinity gradients at least on 100-km resolution every few days for MLS variation.

TABLE OF CONTENTS

LIST OF FIGURES

LIST OF TABLES

ACKNOWLEDGEMENTS

The journey in the School of Oceanography at the University of Washington has been a very special phase of my life. I would like to express my sincere gratitude to my advisor Dr. Ren-Chieh Lien and Dr. Eric D'Asaro for the continuous support, for their vast patience, immense knowledge and encouragements throughout my ups and downs in the years of study. I could not have imagined having better advisors and mentors for my graduate study.

Besides my advisor, I would like to give big thanks to the rest of my academic committee: Dr. Michael McPhaden, LuAnne Thompson, and Mark Warner, for their insightful comments, patience and encouragements throughout the years. My sincere thanks also go to Dr. James Moum, Sally Warner and Dr. Kandaga Pujiana who provided me an opportunity to learn more about the turbulent mixing techniques. I also thank Dr. Chidong Zhang, Dr. Meghan Cronin, Dr. Daehyun Kim, Dr. Ramsey Harcourt, Dr. Elizabeth Thompson and Dr. Toshiaki Shinoda for their insightful discussions and encouragements during my graduate study.

I would like to thank the funding support from National Science Foundation (NSF) who provides me great opportunities to study these interesting projects. I would like to thank all the crew members and the scientists on DYNAMO experiments, and the opportunity to work with them during and after the field experiment. I would also like to thank my cohort in the School of Oceanography at University of Washington for friendship and care during the past years.

Finally, I would like to thank God who places my husband, my parents, my family and my friends in my life and through all the circumstances and opportunities that mold me as who I am.

Chapter 1. INTRODUCTION

Not until recently has the importance of Indian Ocean on climate variability to medium-range atmospheric and marine weather forecast has been recognized and widely accepted. Previous studies discovered profound interannual variabilities of the sea surface temperature (SST) in the tropical Indian Ocean referred to as Indian Ocean dipole (IOD) [e.g., Saji et al., 1999]. It indicates that the tropical Indian Ocean plays an important climatic role both within the region and in other part of the globe. Recent studies also find the corresponding sea surface salinity (SSS) interannual variabilities associated with the IOD and the tight relationship between decadal SSS trend and the changes in atmospheric circulation [e.g., Du and Zhang, 2015; Zhang et al., 2018]. Other than the indirect connections through the atmospheric circulation with other ocean basins, Indian Ocean has a low-latitude exchange route connecting to the global ocean circulation through the Indonesian Throughflow (ITF) [e.g., Godfrey, 1996] across many shallow pathways of the Indonesian Archipelago.

The tropical Indian Ocean is greatly influenced by the largest monsoon system over the globe. The surface prevailing wind directions alternate with seasons and flow in the opposite directions between the Southwest summer and Northeast winter monsoon [e.g., Schott et al., 2009]. Along the equatorial Indian Ocean, the warm and salty (spicy) [e.g., Schneider, 2000, Li et al., 2015] pulses of surface water are transported eastward twice a year along the equator by the narrow Wyrtki jets during monsoon transitional seasons, namely in spring and fall [e.g., Wyrtki, 1973]. The Intertropical Convergence Zone (ITCZ) in the tropical Indian ocean sector also varies with season. Double ITCZ is sometimes identified over the Indian Ocean in late boreal fall [Zhang, 2001]. The ITCZ consolidates and shifts southward off the equator in boreal winter and moves northward in boreal spring. On the other hand, the dominant component of the tropical

intraseasonal variabilities, the Madden-Julian Oscillation (MJO), mainly initiates over the tropical Indian Ocean [e.g., Zhang, 2005; Zhang, 2013]. The MJOs, characterized by the large scale coupled pattern in atmospheric circulation and heavy precipitation with strong surface westerly winds, play an important role in regulating the upper ocean temperature and salinity in tropical Indian and Pacific Oceans over the different phases of the MJO cycle as well as the evolution of ENSO [e.g., Roundy and Kiladis, 2006; Matthews et al., 2010; Webber et al., 2010; Drushka et al., 2012; McPhaden and Foltz, 2013]. Therefore, the upper ocean temperature and salinity in Indian Ocean are foreseen to be driven by complex processes and are variable at multiple different time scales.

The oceanic density depends on both temperature and salinity, of which the volume per unit mass expands with increasing temperature (thermal expansion) while contracts with increasing salinity (haline contraction). The small variation in upper ocean density is very important to the general ocean circulation, oceanic mixing and the ocean buoyancy in the upper ocean. In the deep tropics (refer to as 5°S~5°N) of the Indian Ocean, the sea-surface temperature stays consistently warm year-round (above 28°C) as it sits on the western flank of the Indo-Pacific warm pool, while the upper ocean salinity varies greatly with season owing to the monsoon activities and river inflows (Figure 1.1, 1.2). Previous studies suggest that the upper ocean salinity not only dominates the spatial contrasts, but also dominates the seasonal to intraseasonal changes in upper ocean density for a large portion of the tropical Indian Ocean [e.g., Guan et al., 2014; Köhler et al., 2018]. This suggests that the variation of buoyancy fluxes as part of the exchanges of heat and freshwater between the ocean and atmosphere could be dominant by different mechanisms on seasonal to intraseasonal time scales. In the past decade, several large international collaborative field experiments targeting the tropical Indian Ocean (e.g., Cooperative Indian Ocean experiment on Intraseasonal Variability (CINDY), Dynamics of the Madden-Julian Oscillation

(DYNAMO), The Bay of Bengal boundary Layer Experiment (BoBBLE), Years of the Maritime Continent (YMC)) and the emergence of sea surface salinity satellite products (e.g., Soil Moisture and Ocean Salinity (SMOS), Aquarius/SAC-D mission, Soil Moisture Active Passive (SMAP)) open doors to understanding the variation of the oceanic surface buoyancy and the resulting mixed layer variation in a holistic manner.

Therefore, in this study we employ the in-situ observations and satellite and data products to identify mechanisms that causes the mixed layer heat (temperature) and salinity variation in central equatorial Indian Ocean from seasonal to intraseasonal time scales.

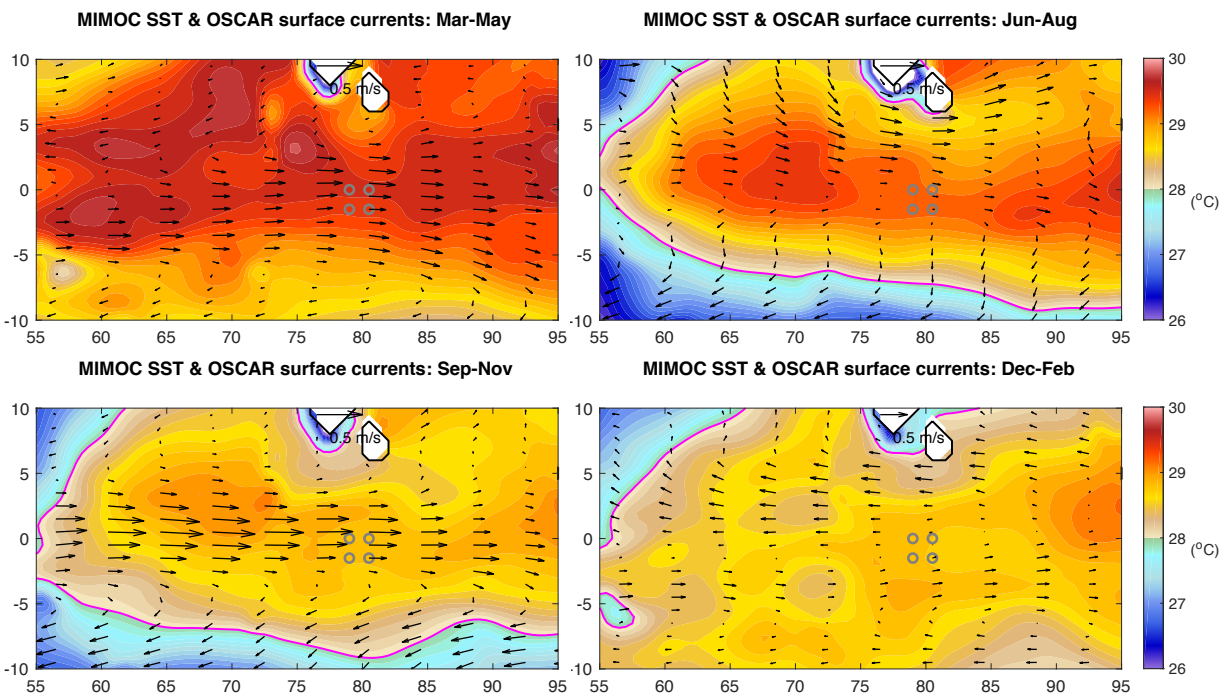

Figure 1.1. The seasonal mean MIMOC SST and OSCAR currents.

The seasonal mean sea surface temperature by Monthly Isopycnal / Mixed-layer Ocean Climatology (MIMOC) (color shading) and the near surface current velocities by Ocean Surface Current Analysis Real-time (OSCAR) (vectors) over the tropical Indian Ocean. MIMOC is based mostly on Argo CTD data and supplemented by shipboard and Ice-Tethered Profiler CTD data. A reference velocity vector of 0.5 m s^{-1} is shown. The magenta contour shows 28°C sea surface temperature.

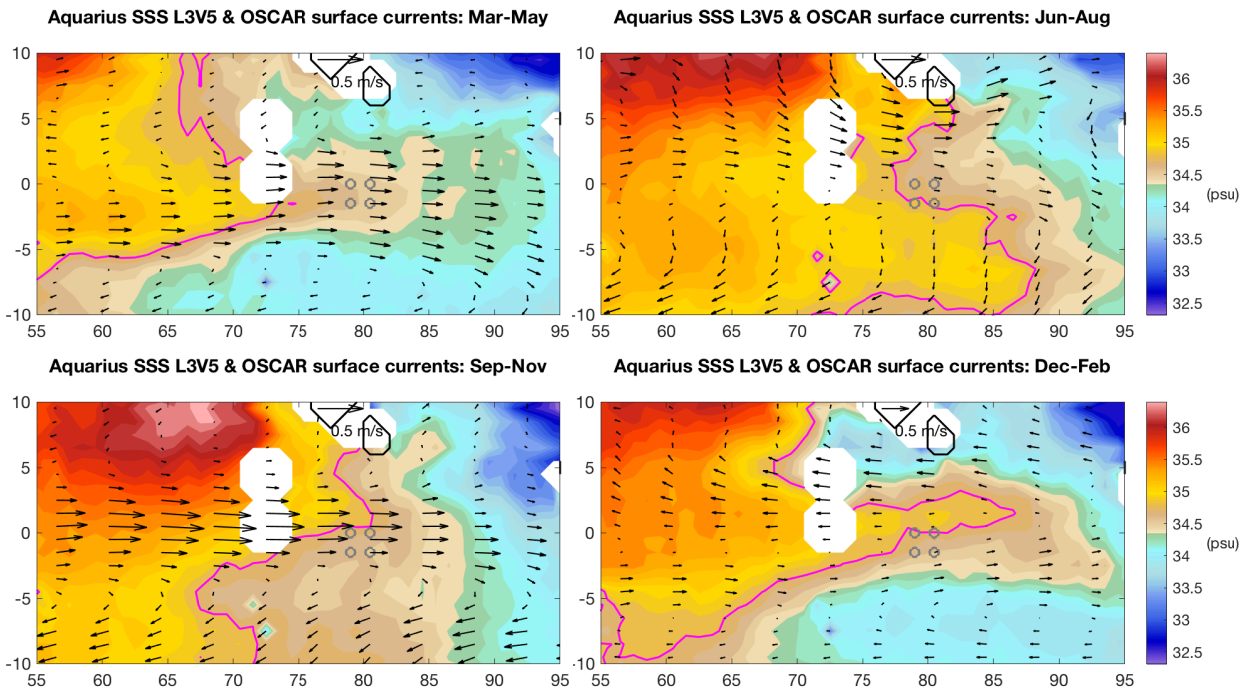

Figure 1.2. The seasonal mean Aquarius L3V5 satellite SSS and OSCAR currents.

The seasonal mean Aquarius L3V5 satellite sea surface salinity (color) and OSCAR near surface current velocities (vectors) over the tropical Indian Ocean. A reference velocity vector of 0.5 ms^{-1} is shown. The magenta contour shows 34.8 psu sea surface salinity.

Chapter 2. SURFACE MIXED LAYER HEAT BUDGET FROM MOORING OBSERVATIONS IN THE CENTRAL EQUATORIAL INDIAN OCEAN

The oceanic surface mixed layer heat budget in the central equatorial Indian Ocean is calculated from observations at two mooring sites (0°S 79°E and 1.5°S 79°E) during three active and calm phases of Madden–Julian Oscillation (MJO) events between September 2011 and January 2012. At both mooring locations, the surface mixed layer is generally heated during MJO calm phases. During MJO active phases at both mooring locations, the surface mixed layer is always cooled by the net surface heat flux and also sometimes by the turbulent heat flux at the bottom of the surface mixed layer. The turbulent heat flux at the bottom of the surface mixed layer, however, varies greatly among different MJO active phases and between the two mooring locations. A barrier layer exerts control on the turbulent heat flux at the base of the surface mixed layer; we quantify this barrier layer strength by a "barrier layer potential energy," which depends on the thickness of the barrier layer, the thickness of the surface mixed layer, and the density stratification across the isothermal layer. During one observed MJO active phase, a strong turbulent heat flux into the mixed layer was diagnosed, despite the presence of a 10-20 m thick barrier layer. This was due to the strong shear across the barrier layer driven by the westerly winds, which provided sufficient available kinetic energy to erode the barrier layer. To better simulate and predict net surface heat fluxes and the MJO, models must simulate the oceanic barrier layer potential energy, background shear, stratification, and surface forcing accurately.

2.1 INTRODUCTION

The Madden–Julian Oscillation (MJO) is a dominant component of the intraseasonal (30–90 days) variability in the tropical atmosphere [e.g., Madden and Julian, 1971; 1972; 1994; Zhang, 2005].

It consists of large-scale coupled patterns in atmospheric circulation and deep convection associated with heavy precipitation and often with surface westerly wind bursts. An MJO generally originates in the central equatorial Indian Ocean, develops as it propagates eastward at a typical speed of 5 m s^{-1}, and weakens in the eastern equatorial Pacific [e.g., Wheeler and Hendon, 2004]. It interacts with weather and climate systems, modulating the variability of rainfall over the monsoonal regions, the formation of tropical cyclones in the Indo-Pacific Ocean and Caribbean Sea, and the evolution of the El Niño-Southern Oscillation [Zhang, 2005; Liebmann et al., 1994].

Strong oceanic responses to MJO atmospheric forcings are expected. The equatorial westerlies associated with the MJO may trigger or enhance the eastward equatorial Wyrtki jet in the Indian Ocean during the transition periods between the two monsoon seasons [Wyrtki, 1973; Nagura and McPhaden, 2008; Schott et al., 2009]. Observations in the Indian Ocean show a strong eastward current in the upper 80 m, strongest between 60°E and 90°E, and a westward undercurrent below 120 m [Wyrtiki, 1973; Iskandar et al., 2009; Moum et al., 2013; McPhaden et al., 2015]. The accompanying westward thermocline uplift at the western origin and sinking at its eastern end of the Wyrtki jet along the equator may have profound effects in changing the mass structure in the ocean [Wyrtki, 1973].

The strong wind bursts and rain associated with the MJO leads to reduced insolation and increased latent heat flux, cooling the upper ocean and fluxing fresh water into the ocean [Cronin and McPhaden, 1997]. Atmospheric convection on intraseasonal timescales, including the MJO, may also be modified by intraseasonal perturbations in SST and the SST gradient [Flatau et al., 1997]. Understanding the surface mixed layer heat budget, the associated SST variations, and its relationship to atmospheric forcing is important to improve the understanding and prediction of the MJO.

Many in situ studies on air–sea interactions and oceanic responses to intraseasonal variability have been done in the western Pacific as a part of the TOGA COARE or TAO experiments [e.g., Cronin and McPhaden, 1997; McPhaden, 2002, Wijesekera and Gregg, 1996], but comparatively fewer in the poorly observed Indian Ocean [e.g., McPhaden et al., 2009; Horii et al., 2011]. Equatorial SST variability on intraseasonal timescales is most significantly influenced by local net surface heat flux in the western Pacific, zonal advection in the central Pacific, and vertical advection and entrainment in the eastern Pacific [McPhaden, 2002]. The atmospheric and oceanic background conditions are different among ocean basins. For example, during the Indian monsoon transitional season the background moisture structure and the direction of currents in the equatorial Indian Ocean differ from those in the equatorial western Pacific [e.g., Tian et al., 2006; Iskhandar et al., 2009]. The oceanic responses to MJO events are expected to vary with basin.

A study of ocean mixed layer responses to MJO events in the central equatorial Indian Ocean suggests that the barrier layer may limit the turbulent heat flux between the surface mixed layer and the thermocline [McPhaden and Foltz, 2013], but does not discuss how the energetics of the barrier layer modulate the turbulent heat flux. Here, we present the surface mixed layer heat budget in the central Indian Ocean at the equator and 1.5°S during three MJO events in 2011 and discuss the effect of the barrier layer and background shear on turbulent heat flux at the base of the surface mixed layer. We quantify the barrier layer strength in modulating turbulent heat flux by measuring its background potential energy, which depends on the barrier layer thicknesses, the surface mixed layer depth, and the density variations across the entire isothermal layer.

We review the definitions of the barrier layer and introduce the concept of the barrier layer potential energy, the available kinetic energy of the background shear, and the available mixing energy in section 2.2. The observational experiment and data are described in section 2.3. Method of the surface mixed layer heat budget is in section 2.4. Results are presented in section 2.5. The

summary and discussion are presented in section 2.6. The details of the surface mixed layer heat budget, error estimates, the sensitivity of the surface mixed layer heat budget with different mixed layer depth definitions and different low-pass filtering time scales are described in the Appendix.

2.2 EQUATIONS

2.2.1 Definitions

The layer separating the top of the thermocline (or the base of the isothermal layer) and the base of the surface mixed layer is referred to as the barrier layer (Figure 2.1). The presence of a barrier layer implies the existence of a strong halocline above the thermocline [e.g., Lukas and Lindstrom, 1991; Sprintall and Tomczak, 1992].

In this study, the mixed layer depth (MLD) is defined using a density threshold method following Foltz et al. [2010] by specifying a density increment from a reference depth near the surface:

$$\sigma_t(z = MLD) = \sigma_t(z = reference\ depth) + \Delta\sigma_t, \quad (1)$$

where σ_t is the potential density, and $\sigma_t = 0.1\ kg\ m^{-3}$ the prescribed density increment. We chose 5 m as the reference depth instead of the shallowest instrument depth (~1 m) to avoid salinity noise due to sharp vertical movement of the surface buoys. The isothermal layer depth (ILD) is computed using the temperature difference equivalence to 0.1 kg m^{-3} of density increase from the reference depth with the salinity observed at the reference depth. The barrier layer thickness (BLT) is defined as ILD–MLD when ILD > MLD. The barrier layer is absent when ILD < MLD. Broad interest in the processes in the upper ocean has resulted in various definitions of MLD, ILD, and BLT. Holte and Talley [2009] developed a hybrid method for finding the MLD that looks for subsurface property anomalies. This method offers an improvement in high latitude oceans and finds similar MLD as that by the density threshold method in places with strong,

sustained temperature gradients beneath the surface mixed layer, such as at the DYNAMO mooring sites (Figure 2.4c).

The presence of a barrier layer can suppress turbulent heat flux at the base of the surface mixed layer by decoupling the communication between the surface mixed layer and the thermocline. A temperature inversion, commonly associated with the barrier layer, could even warm the surface mixed layer by entraining warmer water from below. McPhaden and Foltz [2013] report that a barrier layer may limit the turbulent heat flux at the base of the surface mixed layer in the central equatorial Indian Ocean, using barrier layer thickness as the only proxy for its strength and effects.

We propose a different measure of barrier layer strength to assess its effects on turbulent heat flux at the base of the surface mixed layer. To couple the surface mixed layer with the thermocline, the surface mixed layer water needs to be mixed down to the ILD, i.e., the barrier layer must be eroded. Therefore, the change of potential energy after the erosion of the barrier layer would be a proper measure of the layer's strength.

2.2.2 Barrier Layer Potential Energy: Barrier Layer Strength

We compute the barrier layer potential energy (BLPE) as the difference between the integral of the observed density profile from the surface to the ILD (PE_0) and the same integral using the vertically averaged, i.e., fully mixed, density (PE_{mix}):

$$PE_0 = -g\int_{Z_{ILD}}^{0}\rho(z)zdz = -g\left(\int_{Z_{MLD}}^{0}\rho(z)zdz + \int_{Z_{ILD}}^{Z_{MLD}}\rho(z)zdz\right) \qquad (2)$$

$$PE_{mix} = -g\int_{Z_{ILD}}^{0}\overline{\rho(z)}zdz = -\frac{1}{2}\cdot g\overline{\rho(z)}\cdot h_{ILD}^{2} \quad , \qquad (3)$$

where $\rho(z)$ is the observed potential density, $\overline{\rho(z)}$ the vertically averaged potential density of the isothermal layer, g the gravitational acceleration, z the depth, and h_{ILD} the thickness of the isothermal layer. Because the integrated potential energy when fully mixed is larger than the

integrated potential energy of the observed density profile ($PE_{mix} > PE_0$), the difference, BLPE = $PE_{mix} - PE_0$, represents the increase of potential energy after the erosion of the barrier layer, i.e., the barrier layer strength. The BLPE is governed by the thickness of the surface mixed layer and the barrier layer, as well as the density variation across the entire isothermal layer. It is stronger for a thicker surface mixed layer, a thicker barrier layer, and stronger density stratification in the isothermal layer.

Figure 2.1 presents two barrier layer examples with similar thickness but very different BLPE. The BLPE in Figure 2.1a is much less than in Figure 2.1b because of thinner surface mixed layer and weaker density stratification within the isothermal layer.

2.2.3 Shear Mixing

Energy is needed to mix the surface mixed layer water with the heavier water below. Two major sources of energy from surface forcing that may erode the barrier layer are wind driven turbulent mixing and buoyancy driven convective mixing [Lombardo and Gregg, 1989]. Another source is the interior vertical shear instability. The vertical shear observed in the central equatorial Indian Ocean is a combined consequence of the large-scale background shear (i.e., the Wyrtki jet), the undercurrent, the equatorial waves, and the local surface wind forcing.

One measure of shear instability is the gradient Richardson number, Ri, a dimensionless number that evaluates the relative importance of static stability and dynamic instability [Turner, 1973]. When $Ri < 1/4$ in a high Reynolds number flow, shear instability can occur, with small perturbations growing, breaking, and causing turbulent mixing.

We define the available kinetic energy (AKE) of the surface boundary layer as the observed kinetic energy integrated between the surface and the ILD (KE_0), minus the same integral using the depth averaged velocities (KE_{mix}):

$$KE_0 = \frac{1}{2}\int_{z_{ILD}}^{0} \rho(z)\cdot(u(z)^2 + v(z)^2)\cdot dz\,, \quad (4)$$

$$KE_{mix} = \frac{1}{2}\int_{z_{ILD}}^{0} \bar{\rho}\cdot(\bar{u}^2 + \bar{v}^2)\cdot dz \quad (5)$$

The overbars represent the mean of the physical parameters averaged from the surface to the ILD. Because $KE_{mix} < KE_0$, the difference, $AKE = KE_0 - KE_{mix}$, represents the decrease in kinetic energy due to complete mixing of the barrier layer.

2.2.4 Available Mixing Energy

During the shear instability process, only a fraction of kinetic energy is transformed to potential energy while the rest is dissipated to heat. The energy available to drive mixing is $\Gamma \times AKE$, where Γ is the mixing efficiency. The laboratory values of Γ range from 0.1 to 0.3 [Thorpe, 2005]. We define available mixing energy (AME) as

$$AME = \Gamma\, AKE - BLPE \quad (6)$$

If AME > 0, the AKE provided by the vertical shear is sufficient to completely mix the isothermal layer. If AME < 0, the barrier layer can be eroded partially, but the surface mixed layer remains decoupled from the thermocline, and the turbulent heat flux at the base of the surface mixed layer is suppressed.

In summary, the BLPE quantifies the barrier layer's ability to suppress the turbulent heat flux at the base of the surface mixed layer, while Γ AKE quantifies the shear's ability to mix the barrier layer. When AME > 0 while Ri $< 1/4$, we expect that the barrier layer can be eroded by the shear, thereby reducing its ability to suppress the turbulent heat flux.

2.3 DYNAMO Experiment and Data

DYNAmics of the **M**adden–Julian **O**scillation (DYNAMO) was an international field campaign during October 2011 – March 2012 to enhance the understanding of processes key to MJO

initiation and to improve simulation and prediction of the MJO in the tropical Indian Ocean [Yoneyama et al., 2013]. As part of the DYNAMO field campaign, three pairs of DYNAMO surface moored buoys and subsurface moorings were deployed in mid-September 2011 and recovered in late January 2012 (Figure 2.2). The array was within the larger DYNAMO radar-sounding array, consisting of two ships (the R/V Revelle and the R/V Mirai) and two islands stations (Gan Island and Diego Garcia). The surface moorings were located at (1) 0°S 78°56'E, (2) 1°30'S 78°45'E, and (3) 9°44'S 78°31'E and the subsurface moorings were 5–15 km away. The mooring at 9°44'S broke off during the experiment. Only the equator and 1.5°S mooring measurements are used in this study.

Standard meteorological variables were measured every 10 min at 2–3 m above the sea surface. Subsurface conductivity-temperature-depth (CTD) measurements were taken every 2 min at 1 m, 5 m, 10 m, 15 m, 20 m, 30 m, 40 m, 50 m, 60 m, 70 m, 80 m, 90 m, 101 m, 150 m, 200 m, 300 m, and 500 m. Oceanic currents were measured every 2 min by an upward-looking 300-kHz Acoustic Doppler Current Profiler (ADCP) at 100 m depth, an upward-looking 1200-kHz ADCP at 19 m depth, a Doppler Volume Sampler (DVS) at 8 m depth, a DVS at 3 m depth on the surface moorings and an upward-looking 75-kHz ADCP at 600 m depth on the subsurface moorings. Meteorological sensors on the equatorial buoy were vandalized and the CTD sensor at 1 m depth was damaged on 20 November 2011. The 300-kHz ADCP at 100 m at 1.5°S failed on 9 November 2011; velocity between 22 and 54 m depth was linearly interpolated thereafter. The vertical resolution of the oceanic current observation is 0.5 m for the DVS and 1200-kHz ADCP, 2 m for the 300-kHz ADCP, and 8 m for the 75-kHz ADCP. DYNAMO mooring measurements have fair vertical resolution to quantify BLPE and AKE.

Optimum interpolated (OI) SST products blended by TMI carried on the TRMM satellite and AMSR-E carried on the Aqua satellite are used to compute the horizontal gradient of the

surface mixed layer temperature. The daily OI SST dataset is available on a regular 0.25° longitude and latitude grid.

2.4 Method for Surface Mixed Layer Heat Budget

We consider a simplified version of the surface mixed layer heat budget as presented by Foltz et al. [2010]:

$$\rho c_p h \frac{\partial T_a}{\partial t} = -\rho c_p h \vec{u}_a \frac{\partial T_a}{\partial x} - \rho c_p h \vec{v}_a \frac{\partial T_a}{\partial y} + Q_0 + R\,. \qquad (7)$$

where $h = Z_{MLD}$ is the MLD, T_a the average surface mixed layer temperature, $\vec{v}_a$ the average surface mixed layer currents, C_p the heat capacity, and ρ the sea water density. The terms in (7) represent, from left to right, the surface mixed layer heat storage rate, zonal and meridional advective heat flux, the net surface heat flux (corrected for the penetration of shortwave radiation through the base of the surface mixed layer), and the residual flux including the horizontal divergence of eddy heat flux within the layer, the turbulent heat flux across the base of the surface mixed layer, and errors in the estimation of other terms in (7) [Moisan and Niiler, 1998]. All the heat flux components are averaged daily to match the finest temporal resolution of satellite derived SST, whose spatial gradients are used to compute the advective heat flux in the surface mixed layer. Details of the net surface heat flux estimates, heat budget error estimates and sensitivity of MLD definition to the mixed layer heat budget are described in the Appendix A, B and C respectively.

2.5 Results

2.5.1 Atmospheric and Oceanic Background Condition during DYNAMO

Intraseasonal variations of westerly wind, rain, and near surface sea temperature were observed at the equator and 1.5°S (Figure 2.3). Three MJO active phases at the mooring locations are

defined based on the duration of eastward propagating rain event at the mooring longitude observed by satellite: 25 October – 1 November for MJO1, 23 November – 1 December for MJO2, and 19 December – 24 December for MJO3. Because the rain events in late September 2011 did not propagate eastward, they are not considered as an MJO event. The calm phases are defined as 3 days after the preceding MJO active phases (or local wind/rain event for the MJO1 calm phase) to 3 days before the beginning of the subsequent active phases: 6–22 October for MJO1, 4–20 November for MJO2, and 4–16 December for MJO3. The calm phases are usually longer than the active phases. Changing the length of each MJO calm phases does not change the main findings reported here.

The DYNAMO moorings recorded the meteorology and upper ocean properties from the beginning of the monsoon transition period to the boreal winter monsoon. The increasing westerlies often accompanied by heavy precipitation (Figure 2.3) accelerate the near surface eastward currents, the Wyrtki jet, extending to nearly 100 m depth (Figure 2.4a). The SST was heated during the calm periods with light winds and rain, and cooled during strong westerly wind bursts and rain events (Figures 2.3d, 2.4c). Salinity in the surface mixed layer increased gradually starting in late September and then abruptly in mid-November, coincident with the increasing SST during the MJO2 calm phase (Figure 2.4c, d). After the MJO2 active phase, large salinity variations at time scales of O (4 days) were observed that might be caused by the north–south advection, associated with equatorial waves, of the positive meridional salinity gradient [Webber et al., 2014]. Salinity budgets are discussed separately in chapter 3.

2.5.2 Temporal and Spatial Variations of the Heat Budgets

Estimates of the surface mixed layer heat budget (7) at the equator and 1.5°S mooring locations (Figure 2.5) show a surface mixed layer generally warmed by net surface heat flux during MJO calm phases, except during MJO3. The surface mixed layer is cooled significantly during MJO

active phases by the net surface heat flux and sometimes by the residual flux. Tables 2.1 and 2.2 summarize the mean heat fluxes and corresponding cumulative surface mixed layer temperature changes throughout the three MJO calm and active phases at the equator and 1.5°S. The net surface heat flux generally warms the surface mixed layer during MJO calm phases and cools the surface mixed layer during active phases. During local (non-MJO) wind/rain events in late September, the net surface heat flux also cooled the surface mixed layer at a rate similar to that by the MJO events. The advective heat flux increases after the MJO2 active phase because of the strong Wyrtki Jet and possibly the equatorial waves. During the MJO2 active phase at the equator and MJO3 active phase at 1.5°S, the residual flux is significantly negative. The estimated errors vary with time (Appendix B). The mean error of the 7-day low-pass filtered heat flux is 5 W m^{-2} for net surface heat flux, 7 W m^{-2} for advective heat flux, 68 W m^{-2} for the surface mixed layer heat storage rate, and 69 W m^{-2} for residual flux. The largest error for the surface mixed layer heat storage rate is due to the uncertainty of the estimation of MLD under the pessimistic assumption that error contributions are correlated in the worst possible way.

Figures 2.6 and 2.7 summarize the mean surface mixed layer heat budget during the respective MJO calm and active phases. During the MJO active phases, the net surface heat flux at both mooring locations accounted for 1/3 to 2/3 of the surface mixed layer heat storage rate. The ratio is the magnitude of the net surface heat flux over the sum of the individual magnitude of all heat fluxes in (7). The advective heat flux accounted for no more than 40% and the residual flux could account for 15–60% of the heat budget at the equator and 0–50% at 1.5°S. During the calm phases, the magnitude of all the heat fluxes on the right side of (7) is suppressed compared to those in the active phases. Averaging over the entire 4-month DYNAMO observation period, at the equator the surface mixed layer is cooled by the net surface heat flux and the residual flux.

At 1.5°S the surface mixed layer heat content remains nearly unchanged because the net surface heat flux is balanced by the advective warming and the residual flux cooling (not shown).

Interestingly, the stronger warming of the surface mixed layer during the MJO2 calm phase is followed by a stronger MJO active phase (MJO2) [Moum et al., 2013], stronger westerly wind bursts, and stronger cooling of the surface mixed layer during the MJO2 active phase. Our results highlight differences between the heat budgets at the equator and 1.5°S, as well as the strong variability of the residual and advective heat fluxes. The complexity of advective and residual heat fluxes underscores the importance of oceanic processes in response to the atmospheric MJO forcing.

2.5.3 Barrier Layer Effects on the Turbulent Heat Flux at the Base of the Surface Mixed Layer

Lacking proper observations, we cannot estimate the horizontal divergence of the eddy heat flux, one of the terms in the residual flux in (7). Gill and Niiler (1973) report that the horizontal divergence of the eddy heat flux has a very small seasonal signal. In the following discussion, we approximate the residual flux as the sum of the turbulent heat flux at the base of the surface mixed layer and estimation errors.

2.5.3.1 Barrier Layer Potential Energy (BLPE)

The barrier layer, as thick as 35 m in December 2011, is present at both mooring locations for a substantial period of the DYNAMO observations (Figure 2.8a). The BLPE at the equator was small before MJO2 active phase, increased after MJO2 active phase, and showed bursts of strong BLPE events for several days afterward (Figure 2.8b). The increase of BLPE soon after the MJO2 active phase is due to a combination of increasing MLD and increasing density stratification across the entire isothermal layer. After early December, the rising BLPE is also due to the increase of the barrier layer thickness. The BLPE at 1.5°S is generally similar but

slightly greater than at the equator after the calm phase of MJO3 through mid-January 2012 due to a stronger vertical salinity gradient above the ILD that increases the stratification (not shown). The increase in BLPE raises the threshold of energy needed to entrain/mix the cold water from below the ILD.

Below the MLD, 30% of the vertical temperature profiles at the equator and 12% at 1.5°S have a temperature inversion. Half of the temperature inversions occur during daytime when there is ample shortwave heating suggesting that the daytime shortwave heating is not strong enough to completely eliminate the temperature inversion in the barrier layer. The temperature inversion below the MLD changes the sign of the turbulent heat flux at the base of the surface mixed layer, i.e., heating the surface mixed layer by entraining warmer water from below. The turbulent heat flux at the base of the surface mixed layer then mixes the warmer water in the barrier layer with the cooler water in the surface mixed layer and may eliminate the temperature inversion in the barrier layer. During the MJO2 and MJO3 calm phases, the barrier layer is generally thicker than the subsequent active phases and more occurrence of temperature inversion is observed. This is a favorable condition for SST heating and atmospheric deep convection.

2.5.3.2 Available Kinetic Energy (AKE) and Available Mixing Energy (AME)

During MJO1 active and calm phases, the available kinetic energy (AKE) at both mooring locations is relatively small at the early stage of the monsoon transitional season (Figure 2.8c). The AKE at the equator increases abruptly during the MJO2 active phase, presumably caused by the strong Wyrtki Jet and vertical shear, both are driven by the strong westerly wind. The AME at the equator is positive during the MJO2 active phase (Figure 2.8d), suggesting available mixing energy (AME) to erode the barrier layer. This positive AME is a result of an abrupt increase of AKE coincident with relatively unchanged BLPE. In contrast, no positive AME is

present during the MJO3 active phase at the equator, illustrating a case of strong BLPE resisting the complete erosion of the barrier layer by the vigorous but insufficient AKE.

During the MJO2 active phase at equator, both residual heat flux and AME are large despite the presence of the barrier layer (Figure 2.7a, 2.8d). Subcritical values of Ri (< ¼) above the ILD (Figure 2.8e) are common, suggesting shear instability. The combination of subcritical Ri and positive AME implies that the negative heat flux at the base of the surface mixed layer is transported from the thermocline through the barrier layer; the shear is sufficiently strong to overcome the barrier layer stratification. This explains the strong turbulent heat flux at the base of the surface mixed layer despite the presence of a 10–20-m thick barrier layer. During the MJO3 active phase at 1.5°S, the residual flux is also significant and AME is positive in the presence of the barrier layer (not shown). However, the estimates of AKE and AME at 1.5°S are less reliable due to interpolated velocity data between 22 m and 54 m (see 3.2); further discussion of AKE and AME at 1.5°S requires caution.

The occurrence of a temperature inversion below the MLD, commonly associated a barrier layer, is substantially reduced during the MJO2 active phase at the equator. It may be due to the barrier layer (partly) eroded by the vigorous MJO2 atmospheric forcing. Our observations did not capture the barrier layer erosion process either because it was incomplete or occurring at a time scale too short to be resolved by the mooring measurements.

2.6 SUMMARY AND DISCUSSION

We examine the ocean surface mixed layer heat budget during three MJO calm and active phases in the central equatorial Indian Ocean from mid-September 2011 to late January 2012. Observations include mooring measurements taken at the equator and 1.5°S, and satellite SST and precipitation measurements. At both mooring locations, the surface mixed layer is generally

heated during MJO calm phases and cooled during the MJO active phases by the net surface heat flux. During the active phases the cooling is also sometimes driven by the turbulent heat flux at the base of the surface mixed layer. The surface mixed layer is cooled more at the equator than at 1.5°S during the three MJO active phases. Throughout the MJO2 calm phase, the surface mixed layer at equator is gradually warmed by 1 K and is followed by the strongest MJO active phase (MJO2) observed during DYNAMO. The magnitude of the net surface heat flux to wind/rain events is generally similar at the two mooring locations, and between local wind/rain events and those associated with MJO active phases. In contrast, the advective and turbulent heat fluxes at the base of the surface mixed layer vary greatly among different MJO active phases and between the equator and 1.5°S locations, suggesting the important and complicated roles of oceanic processes in the surface mixed layer heat budget.

The competition between the barrier layer strength (or BLPE) and the available kinetic energy (AKE) determines whether the cooler water below the isothermal layer would be entrained into the surface mixed layer. The sign of available mixing energy (AME) with a reasonable mixing efficiency and small Richardson number provides a way to diagnose and evaluate the contribution of the turbulent heat flux at the base of the surface mixed layer that is rarely measured, except by special microstructure platforms. This method suggests that the large residual flux at the equator during the MJO2 active phase is likely contributed by turbulent heat flux at the base of the surface mixed layer even in the presence of a barrier layer. Although it is suggested that a thick barrier layer may limit the turbulent heat transfer between the surface mixed layer and the thermocline, the background vertical shear might be, at times, strong enough to erode the barrier layer. During the MJO1 and MJO3 active phases at the equator, AME is negative, consistent with the estimate of weaker turbulent heat flux at the base of the MLD.

Atmosphere and ocean are coupled through heat, momentum, and freshwater fluxes. In the central equatorial Indian Ocean where SST is close to the necessary threshold for atmospheric deep convection [e.g., Graham and Barnett, 1987], small variations or errors in SST estimation can lead to large uncertainties in surface heat exchange. An SST change of 1 K in the DYNAMO mooring data could lead to an air–sea heat flux change of 41 to 48 W m^{-2}. The error is estimated using COARE 3.5 with the range of air–sea measurements at the moorings. This underscores accurate SST measurements and surface mixed layer heat budgets to estimate the air–sea heat flux. Here, we find that oceanic processes, including advection and turbulent processes, may contribute considerably to the surface mixed layer heat budget, and thus to the SST. For example, the residual flux, most likely the turbulent heat flux at the base of the surface mixed layer, is -66 ± 69 W m^{-2} during the three observed MJO active phases. The large mean values and large variations suggest that oceanic processes are important for the surface mixed layer heat budget and air–sea interaction during MJO active phases. A coupled atmosphere–ocean model with an accurate surface mixed layer parameterization is needed to improve the model prediction of the MJO and oceanic responses. Furthermore, the effects of the barrier layer and vertical shear should be simulated or parameterized properly to predict the turbulent heat flux at the base of the surface mixed layer accurately.

Table 2.1. Components of heat fluxes and cumulative change of the surface mixed layer temperature in the surface mixed layer heat budget during the three MJO calm phases. The unit of the surface mixed layer heat budget ($\bar{Q}$) and the cumulative change of the surface mixed layer temperature ($\overline{\partial T}$) is W m^{-2} and K respectively.

	MJO1 calm phase (2011/10/6~10/22)		MJO2 calm phase (2011/11/4~11/20)		MJO3 calm phase (2011/12/4~12/16)	
	Equator	1.5°S	Equator	1.5°S	Equator	1.5°S
$\overline{\partial T}_{\text{Mixed layer}}$	0.44	0.59	0.96	0.24	–0.55	-0.28
($\bar{Q}_{\text{Mixed layer}}$)	(42)	(48)	(77)	(15)	(–52)	(-18)
$\overline{\partial T}_{\text{Net surface heat flux}}$	0.16	0.48	1.06	0.69	0.05	0
($\bar{Q}_{\text{Net surface heat flux}}$)	(20)	(34)	(41)	(46)	(2)	(11)
$\overline{\partial T}_{\text{Advective heat flux}}$	0.22	0.19	0.07	0.19	–0.14	0.07
($\bar{Q}_{\text{Advective heat flux}}$)	(18)	(12)	(1)	(14)	(–6)	(2)
$\overline{\partial T}_{\text{Residual flux}}$	0.06	–0.08	–0.17	–0.64	–0.46	–0.35
($\bar{Q}_{\text{Residual flux}}$)	(4)	(2)	(35)	(–45)	(–48)	(–31)

Table 2.2. As in Table 2.1 but for MJO active phases.

	MJO1 active phase (2011/10/25~11/1)		MJO2 active phase (2011/11/23~12/1)		MJO3 active phase (2011/12/19~12/24)	
	Equator	1.5°S	Equator	1.5°S	Equator	1.5°S
$\overline{\partial T}_{\text{Mixed layer}}$	–0.4	–0.11	–1.06	–0.62	–0.46	–0.54
$(\bar{Q}_{\text{Mixed layer}})$	(–91.3)	(–24.1)	(–267.4)	(–118.9)	(–224.1)	(–153.9)
$\overline{\partial T}_{\text{Net surface heat flux}}$	–0.29	–0.43	–0.42	–0.50	–0.27	–0.31
$(\bar{Q}_{\text{Net surface heat flux}})$	(–80.2)	(–69.5)	(–97.4)	(–94.2)	(–102.1)	(–92.4)
$\overline{\partial T}_{\text{Advective heat flux}}$	0.03	0.26	–0.07	-0.15	–0.12	0.18
$(\bar{Q}_{\text{Advective heat flux}})$	(13.8)	(43.4)	(–17.4)	(-35.9)	(–58.2)	(56.6)
$\overline{\partial T}_{\text{Residual flux}}$	–0.14	0.06	–0.57	0.03	–0.07	–0.42
$(\bar{Q}_{\text{Residual flux}})$	(–24.8)	(1.9)	(–152.6)	(11.3)	(–63.8)	(–118.1)

Table 2.3. Meteorological instrument random error and systematic errors, and random errors on the estimate of the surface mixed layer depth. The random instrument error is the largest values between the instrument accuracy provided by the instrument company and white noise level of the spectra. The systematic instrument error accounts for the mean difference between the nearby shipboard measurements (Appendix B).

	Random instrument error	**Systematic instrument error**
Δh (h: surface mixed layer depth)	5 m (2-min)	N/A
u_a or v_a (a: average in the surface mixed layer)	0.057 m s^{-1} (2-min)	N/A
T_a	0.006°C (10-min)	N/A
Wind speed	0.03 m s^{-1} (10-min)	N/A
Air Temperature	0.17°C (10-min)	1.35°C
RH	5 % (10-min)	6.58 %
T_{bulk}	0.03°C (10-min)	N/A
$T_{satellite\ (near\ moorings)}$	0.1°C (day)	N/A
Long wave radiation	1.2 W m^{-2}	10.2 W m^{-2}

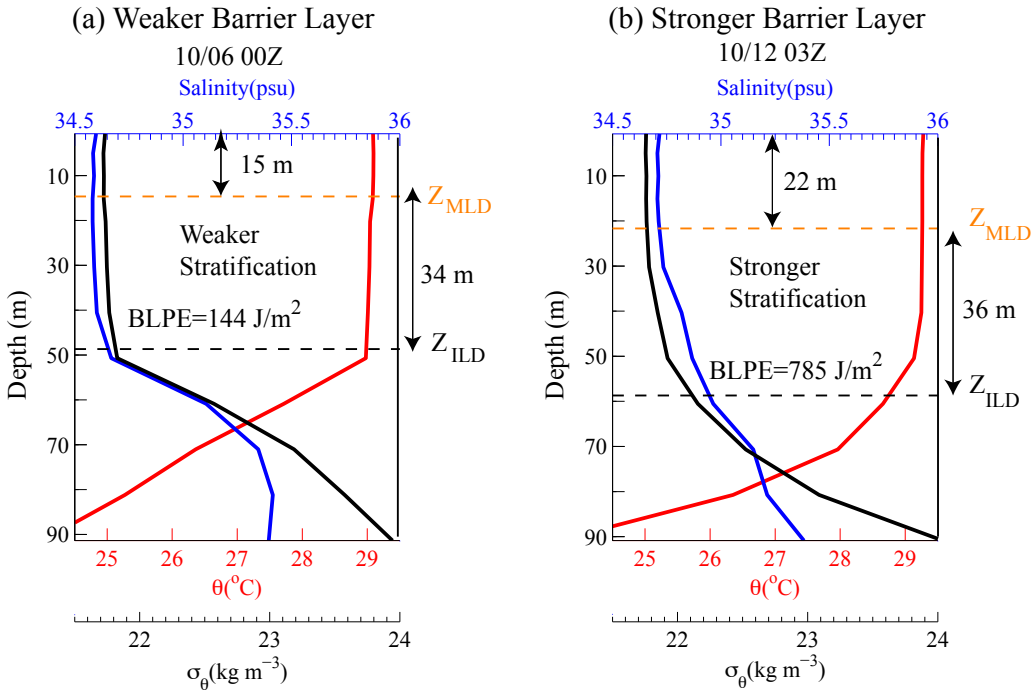

Figure 2.1. Two examples of the barrier layer from the equator mooring.

(a) at 00Z on 6 October 2011 and (b) at 03Z on 12 October 2011. Black profiles are potential density (σ_t). Red and blue profiles are their corresponding potential temperature and salinity. The orange dashed horizontal lines mark the surface mixed layer depth, i.e., Z_{MLD}, MLD. The black dashed horizontal lines mark the isothermal layer depth, i.e., Z_{ILD}, ILD. The layer between MLD and ILD is the barrier layer. The barrier layer potential energy (BLPE), discussed in section 2.2.2, is labeled.

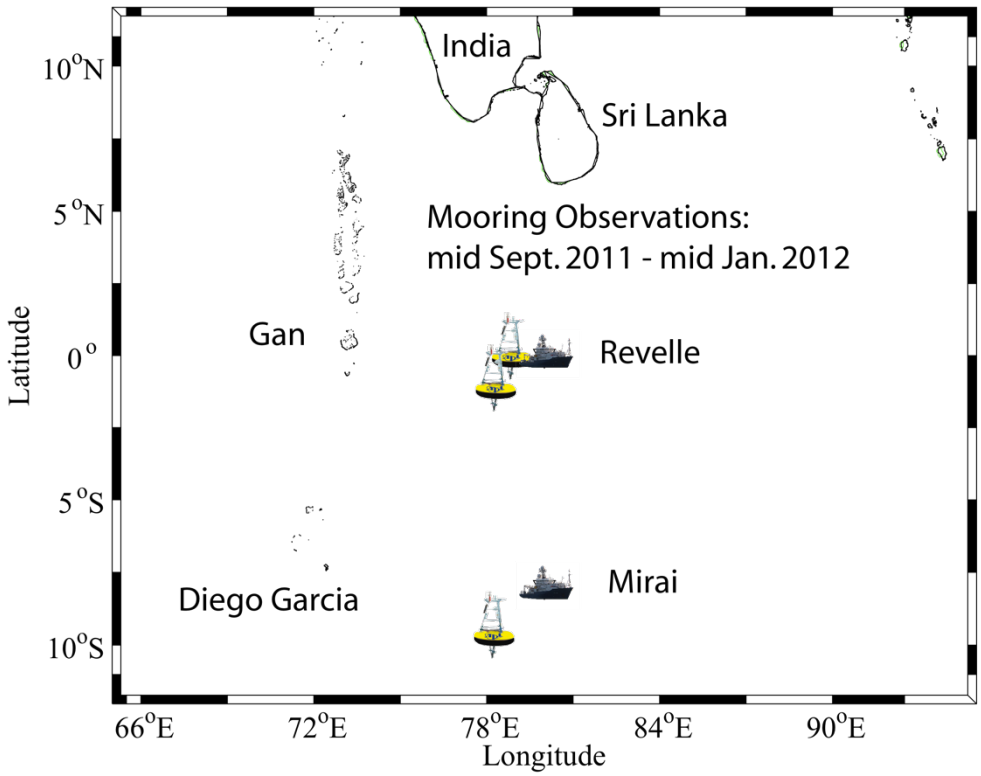

Figure 2.2. A schematic plot of DYNAMO field experiment assets.

Surface moorings along ~79°E longitude (yellow donuts with towers), the R/V Revelle and R/V Mirai, and two island radar stations at Gan and Diego Garcia.

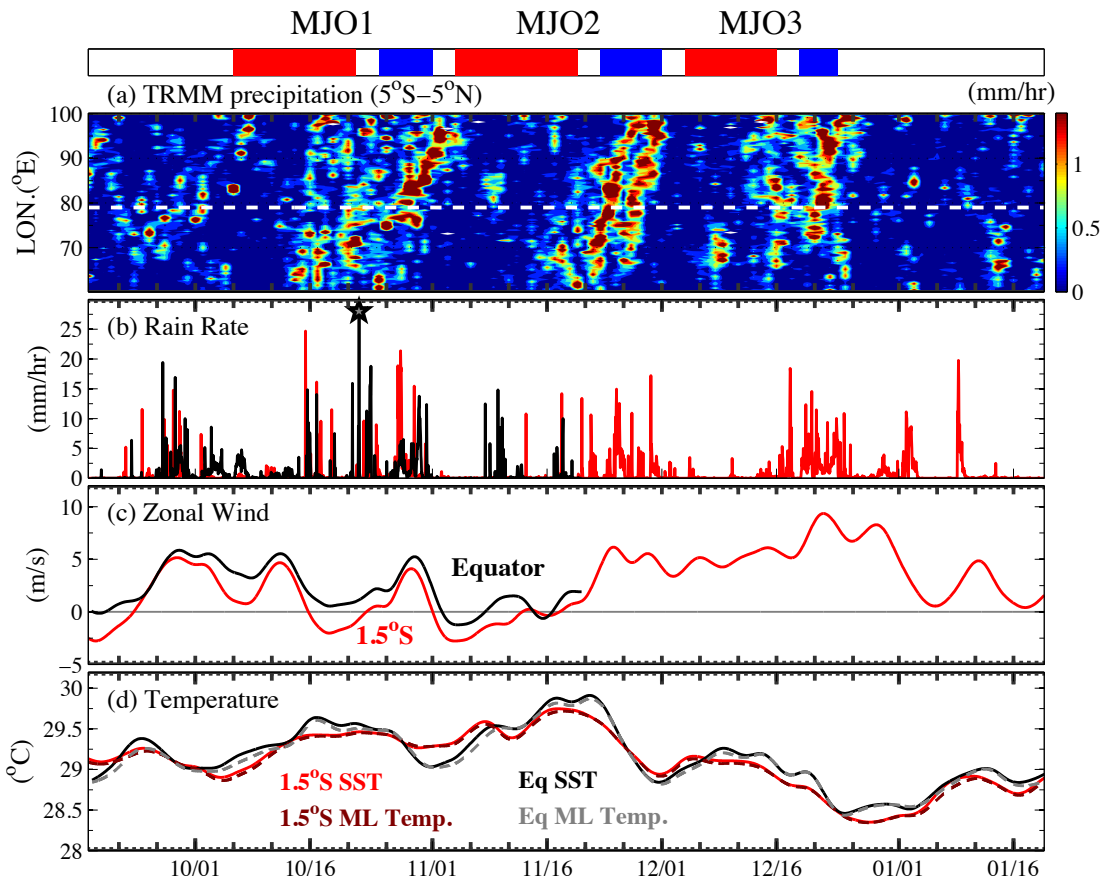

Figure 2.3. Time series of TRMM precipitation and rain-rate, 7-day low-pass filtered zonal wind, 7-day low-pass filtered 5m and ML sea temperature at the equator and 1.5°S moorings.

(a) Time longitude plot of TRMM precipitation averaged between 5°S and 5°N latitude. (b) The 10-min rain rate at the equator (black) and 1.5°S (red) moorings. (c) The 7-day low-pass filtered zonal wind at the equator (black) and 1.5°S (red) moorings. (d) The 7-day low-pass filtered 5 m sea temperature at the equator (solid black) and 1.5°S (solid red) moorings, and 7-day low-pass filtered surface mixed layer temperature at the equator (dashed gray) and 1.5°S (dashed dark brown) moorings. The choice of the 7-day low-pass filter is described in Appendix D. The three MJO active phases are labeled with blue horizontal bars and calm phases are labeled with red horizontal bars above (a). White dashed line in (a) is longitude of the moorings.

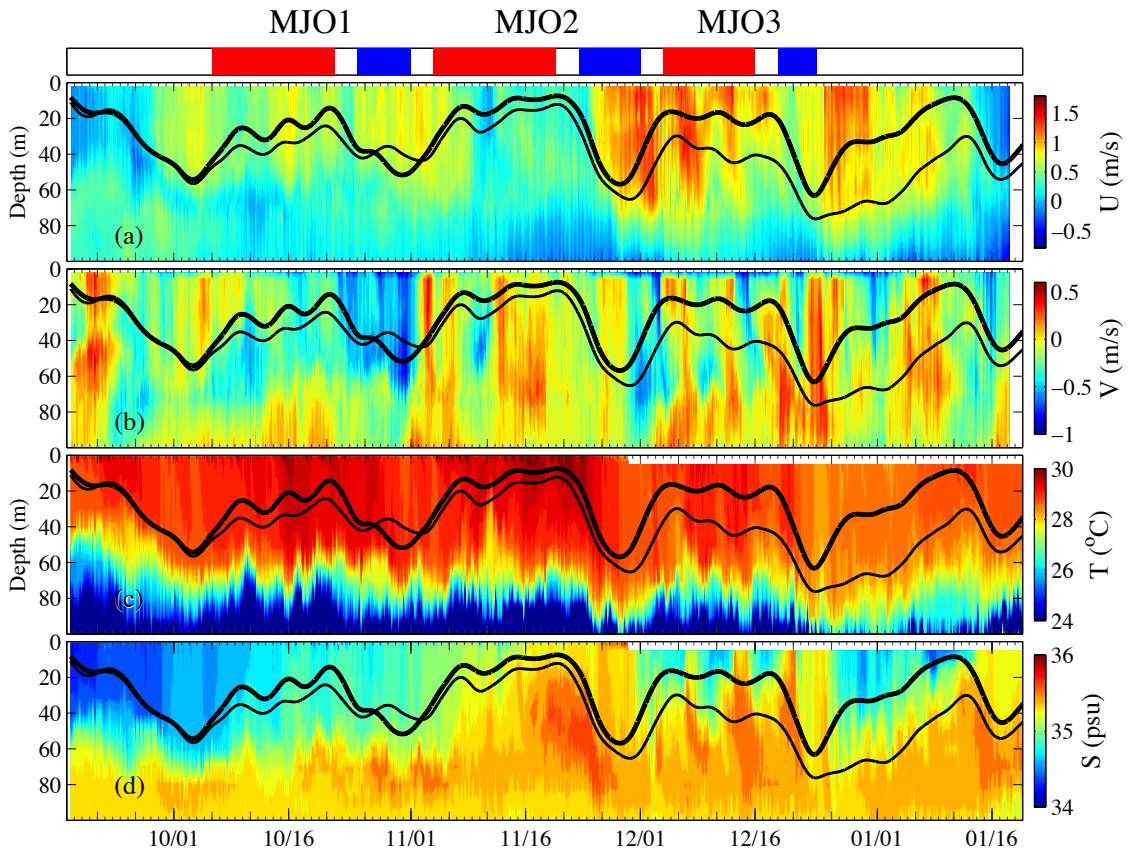

Figure 2.4. The hourly averaged time series of current velocity, temperature and salinity in the upper 100 m at the equator mooring.

The hourly averaged (a) zonal velocity, (b) meridional velocity, (c) temperature and (d) salinity in the upper 100 m at the equator mooring. The three MJO active and calm phases are labeled as in Figure 2.3. Temporal variation of the 7-day low-pass filtered surface mixed layer depth (thick line) and the isothermal layer depth (thin line) at the equator are superimposed.

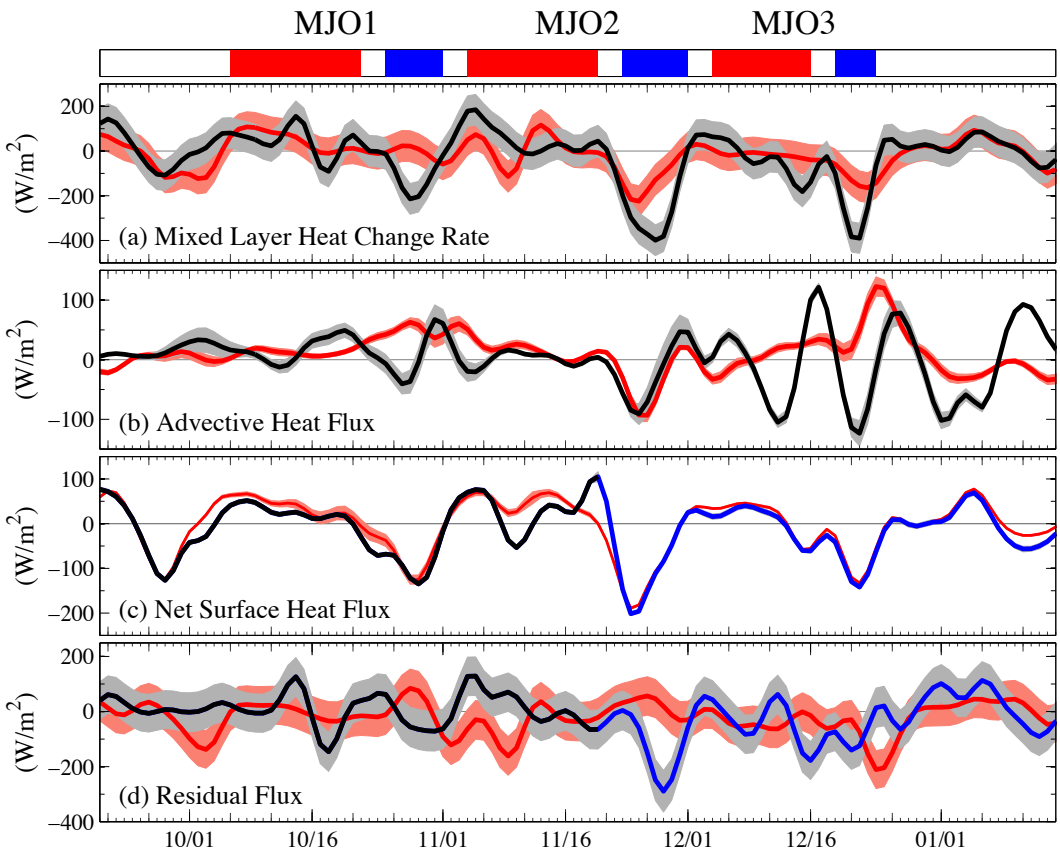

Figure 2.5. The 7-day low-pass filtered surface mixed layer heat components at the equator and 1.5°S moorings.

The 7-day low-pass filtered surface mixed layer heat components at the equator (black and blue lines) and 1.5°S (red lines) moorings as described in (7). (a) The surface mixed layer heat storage rate. (b) Advective heat flux. (c) Net surface heat flux: surface heat flux corrected by penetrative shortwave radiation through the base of the surface mixed layer. (d) Residual flux. The blue line in (c) is the surrogate of the net surface heat flux at the equator mooring using that measured at the 1.5°S mooring corrected by a constant offset. The blue line in (d) is the corresponding residual flux at the equator mooring using the surrogate net surface heat flux. Gray and pink shades are one standard deviation of the error estimates of heat fluxes at the equator and 1.5°S

moorings, respectively. The errors of the advective heat flux and the net surface heat flux are sometimes too small to see. The three MJO active and calm phases are labeled as in Figure 2.3.

(a) Equator

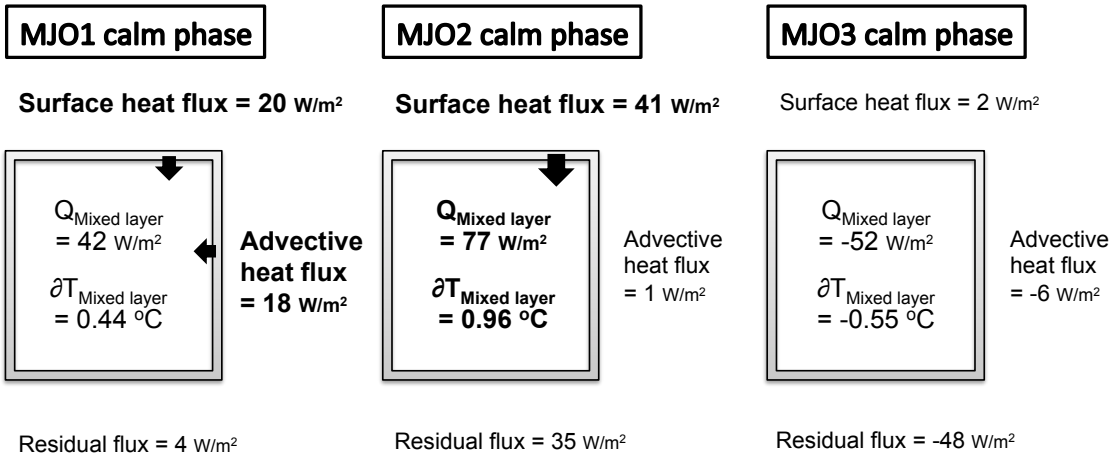

(b) 1.5°S

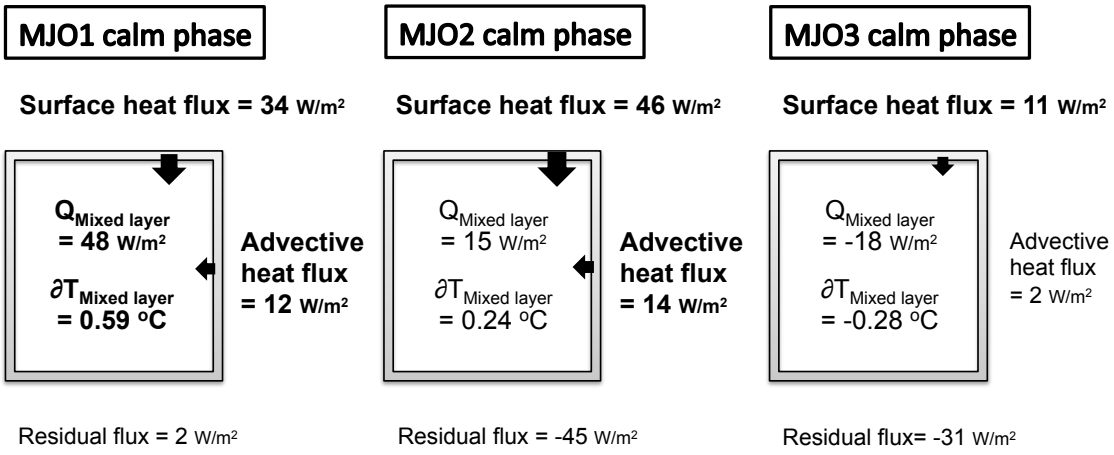

Figure 2.6. Cartoon summarizing the mean surface mixed layer heat budget during three MJO calm phases at the equator and 1.5°S moorings.

(a) at the equator and (b) at 1.5°S. Filled arrows outward from the boxes represent cooling of the surface mixed layer. Filled arrows into the boxes represent warming of the surface mixed layer. The area of the arrows is scaled by the magnitude of the heat flux. When the magnitude of the heat components in (7) is smaller than the error, no arrow is shown.

(a) Equator

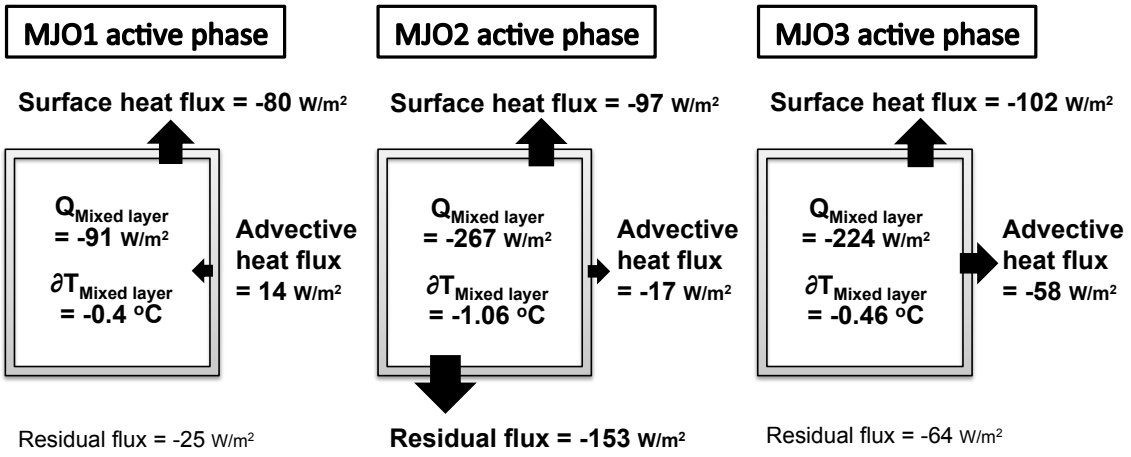

(b) 1.5°S

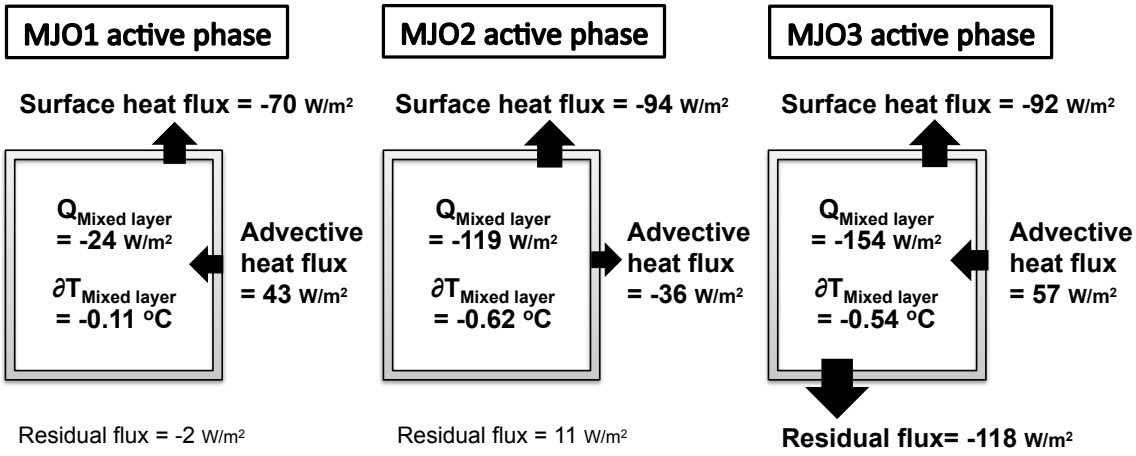

Figure 2.7. As in Figure 2.6 but for MJO active phases.

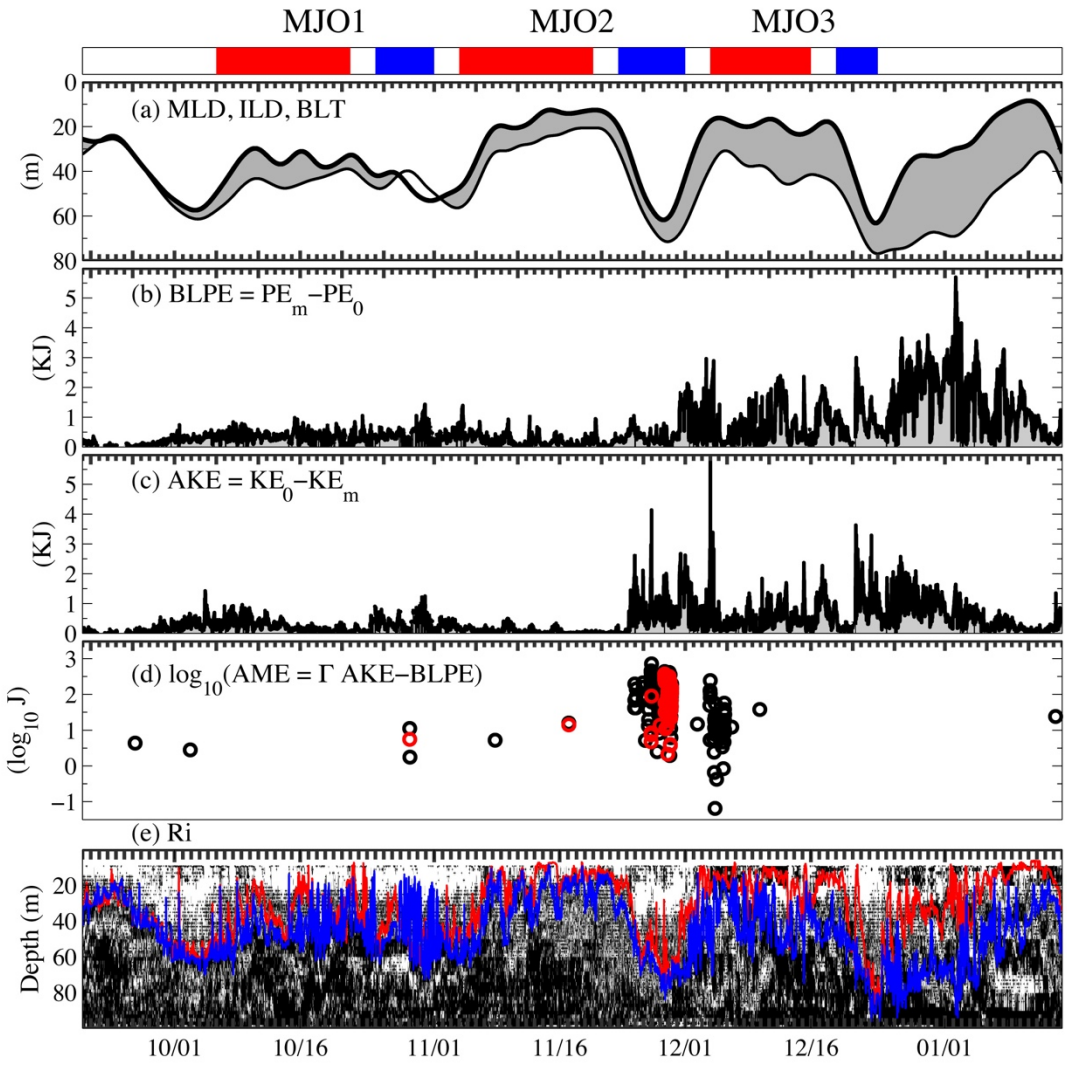

Figure 2.8. The time series of the 7-day low-pass filtered surface mixed layer depth, isothermal layer depth, barrier layer, BLPE, AKE, AME, and Ri at the equator mooring.

The equator mooring results of (a) the 7-day low-pass filtered surface mixed layer depth (thick line) and the isothermal layer depth (thin line). The shading represents the barrier layer. (b) The 10-min barrier layer potential energy (BLPE). (c) The 10-min available kinetic energy (AKE). (d) The logarithm scale of the available mixing energy, $log_{10}(\Gamma\ AKE - BLPE)$, where Γ is the mixing efficiency, shown only for $\Gamma\ AKE - BLPE > 0$. The black dots are for $\Gamma = 0.25$ and the red dots are for $\Gamma = 0.1$. (e) White pixels are for Ri < 0.25, indicating shear instability. Black

pixels are for Ri > 0.25. The red line is the hourly surface mixed layer depth and the blue line is the hourly isothermal layer depth. The BLPE and AKE are discussed in section 2.2. The three MJO active and calm phases are labeled as in Figure 2.3.

Chapter 3. THE MIXED LAYER SALINITY BUDGET IN THE CENTRAL EQUATORIAL INDIAN OCEAN

This study investigates the oceanic surface mixed layer salinity (MLS) budget in the central equatorial Indian Ocean using measurement taken by two DYNAMO and two RAMA moorings during September 2011 to January 2012. Turbulent salinity mixing rates measured by the shipboard microstructure profiler are from Pujiana et al. (2018). The MLS in broader central to eastern equatorial Indian Ocean in boreal fall and winter between 2011 to 2015 is derived using satellite products including TRMM, Aquarius, and data products including OSCAR, OAFlux and Argo mixed layers. In this study, boreal fall is referred to as September to November and boreal winter is referred to as December to February.

In boreal fall the equatorial mooring MLS increases due to zonal and meridional advection and turbulent mixing, despite the excess of precipitation over evaporation that often associated with MJOs. From December to January (early boreal winter) the equatorial and 1.5°S mooring MLS are roughly unchanged despite of large sub-seasonal variation. It is balanced between negative zonal advection and precipitation versus positive meridional advection and turbulent flux at the equator, and between negative meridional advection and precipitation versus positive zonal advection and turbulent flux at 1.5°S. The increase of the central to eastern equatorial MLS accompanied by the decrease off the equator creates the high equatorial salinity tongue in boreal fall, while in boreal winter the maximal MLS decrease at the equatorial band resembles the retrogression of the high equatorial salinity tongue. On sub-monthly to seasonal time scales, the strength and timing of the zonal advection determine the development and retrogression of the seasonal high salinity tongue centered at the central to eastern equatorial Indian Ocean. The surface freshwater flux is secondary, and the meridional shift of maximal freshening effect with season is associated with migration of the ITCZ. Therefore, to better

simulate and predict the MLS changes in the equatorial Indian Ocean, models should properly predict the strength and timing of the equatorial currents as well as the salinity gradients at least on one-degree resolution every few days.

3.1 Introduction and Motivation

3.1.1 Why are we interested in the upper ocean salinity variation?

The ocean has long been considered as a rain gauge for its clear relation between the ocean salinity and global hydrological cycle. In addition to the impacts of river runoff near coastal regions and ice melting in high latitudes, ocean dynamics complicates relationship between surface freshwater flux (evaporation and precipitation) and the surface mixed layer salinity (MLS) in the open ocean [e.g., Yu, 2011; Ponte and Vinogradova, 2013]. Observational studies conclude that MLS variation impacts the ocean general circulation, water mass formation, oceanic surface buoyancy, and oceanic mixing, etc. [e.g., Dickson et al., 1988; Lukas and Lindstrom, 1991; Kumar and Prasad, 1999; Rudnick and Ferrari, 1999]. One of the impacts on ocean dynamics by MLS variation is through the salinity stratification above the thermocline. The salinity stratification above the thermocline, which partially controlled by MLS, determines the existence and the strength of the barrier layer [e.g., Chi et al., 2014]. The salinity-stratified isothermal layer is frequently observed in the deep tropics of each ocean [e.g., Sprintall and Tomczak, 1992; Lukas and Lindstrom, 1999; De Boyer Montegut et al., 2007; Mignot et al., 2007]. This near surface halocline prevents turbulent mixing from entraining cold thermocline water into the warm isothermal layer [e.g., Godfrey and Lindstrom, 1989; Chi et al., 2014] and retards the instantaneous thermal coupling between the atmosphere and ocean surface [e.g., Joseph et al., 2017]. Therefore, the MLS variation modulates the upper ocean processes that may lead to profound consequences on the air-sea interaction and hence potential climate impacts.

3.1.2 Background of the Tropical Indian Ocean

Recently more attention has been drawn to the tropical Indian Ocean for the discovery of much greater impacts on climate than previously thought [e.g., Saji et al., 1999; Cherchi et al., 2007; Abram et al., 2008; Roxy et al., 2014; Zhang et al., 2018]. The central to eastern equatorial Indian Ocean, as part of the Indo-Pacific warm pool, is a region characterized by high sea surface temperature (SST) and light mean annual winds. Atmospheric deep convections with large rainfall rates and quasi-permanent barrier layers are frequently found in the central to eastern tropical Indian Ocean and Bay of Bengal [e.g., Schott et al., 2009; de Boyer Montegut et al., 2007]. On the other hand, the hemispheric asymmetry in landmass surrounding the Indian Ocean drives the strongest monsoon on the Earth, which the wind direction reverses almost 180° north of 10°S between southwest summer monsoon and northeast winter monsoon [e.g., Schott et al., 2009]. The monsoonal winds create intense seasonal variations in surface currents, freshwater flux, transport of the water masses, and many of which exhibits annual or semi-annual directional reversals [e.g., Schott and McCreary., 2001]. Unlike in the other equatorial oceans, the wind forcing generates an annual-mean eastward zonal wind stress and surface currents over equatorial Indian Ocean so that the equatorial upwelling, eastern equatorial cold tongue and permanent EUCs are absent in Indian Ocean [e.g., Iskandar et al., 2009; Schott and McCreary, 2001]. In-situ observation indicates that surface currents in the equatorial Indian Ocean reverse directions four times a year [e.g., Schott et al., 2009]. During the inter-monsoon season in boreal spring and fall, the strong eastward surface jets, commonly referred to as Wyrtki jets, appear and center at the equatorial Indian Ocean owing to the semi-annual westerly equatorial winds [e.g., Wyrtki, 1973; Han et al., 1999; Schott and McCreary, 2001]. These equatorial jets serve as a major conduit for mass and heat transfer between the eastern and western sides of the basin which mitigates the salinity difference between Arabian Sea and Bay of Bengal [McPhaden et al., 2015; Wijeskera et al., 2015, Gordon et al., 2016, Jensen

et al., 2016]. Therefore, the semi-annual Wyrtki jets could impact the MLS, mixed layer depth, thermocline slope and the ocean-atmosphere interaction.

3.1.3 What impacts MLS variation in the tropical Indian Ocean?

The central to eastern tropical Indian Ocean receives an excess of freshwater from precipitation and river runoff while the far western basin is subject to excess evaporation annually. However, the distribution of freshwater input does not correspond to the observed sea surface salinity (SSS) distribution in the tropical Indian Ocean [e.g., Yu, 2011; Nyadjro and Subrahmanyam, 2016]. Previous studies suggest the horizontal salinity advection and turbulent mixing (diffusion) are important in maintaining the large-scale SSS variabilities in the central to eastern equatorial Indian and western equatorial Pacific Oceans [Guan et al., 2014; Ponte and Vinogradova, 2016; Köhler et al., 2017]. Nyadjro and Subrahmanyam (2016) suggested that the zonal advection of salty water pulses, along with the Intertropical Convergence Tropical Zone (ITCZ)-driven precipitation, ocean currents and fresh water from Pacific via Indonesian Throughflow (ITF), control the zonally-oriented meridional SSS fronts in the equatorial Indian Ocean.

On interannual time scales, recent satellite and data products studies indicate that the oceanic dynamics dominates the salinity dipole mode in tropical Indian Ocean [Du and Zhang, 2015; Zhang et al., 2018]. On seasonal time scales, satellite observation and model suggest that the MLS changes is largely controlled by ITCZ-driven freshwater flux south of the equator and horizontal advection dominates the MLS changes in the equatorial regions [Köhler et al., 2017]. On sub-monthly time scales the MJO, the dominant component of the tropical intraseasonal variabilities [e.g., Madden and Julian, 1971, 1972, 1994; Zhang, 2005; Zhang, 2013], places significant effects in regulating the SST, SSS and upper-ocean current in the tropical Indian and western Pacific Oceans [e.g., Sengupta et al., 2007; Iskandar and McPhaden, 2011; Matthews et al., 2010; Drushka et al., 2012; Chi et al., 2014; Pujiana et al., 2018]. Furthermore, in tropical

Indian Ocean the MLS has an overall larger contribution to surface density and potential energy anomalies than SST associated with MJOs [Guan et al., 2014] and associated with seasonality [Köhler et al., 2017].

Results from the previous studies indicate the necessity for further understanding and confirming the mechanisms that controls the MLS variabilities in the equatorial Indian Ocean, in particular the horizontal MLS advection since it has not been quantified using in-situ observations.

3.1.4 What causes the development and retreat of the equatorial high salinity tongue?

Aquarius SSS observations reveal a zonal strip of salty surface water developing along the equator in boreal fall and usually a second peak in boreal spring (Figure 3.1, 3.2). The equatorial high salinity maximum extends from the central equatorial Indian Ocean (65°~75°E) to off the west coast of Sumatra (85°~90°E) in the boreal fall and retreats westward in the boreal winter. The concurrent Wyrtki jets from OSCAR and satellite SSS suggest that the horizontal salinity advection contributes to the zonal development and retreat of the high salinity tongue along the equator. The meridional extent of the eastward Wyrtki jets in boreal fall is roughly 5° of latitude centered at the equator (Figure 3.3). Just north of the equatorial jets, the surface currents change from Southwest Monsoon Currents (SMC) in boreal summer to Northwest Monsoon Currents (NMC) in boreal winter associated with monsoonal winds in northern Indian Ocean [e.g., Schott et al., 2009]. The reversal between eastward to westward flowing surface currents north of the central equatorial region is accompanied by the freshening of surface salinity during boreal fall to early winter. Just south of the equatorial Wyrtki jets, the surface current flows westward referred to as South Equatorial Current (SEC) in boreal fall when the southeast trades shift northward. In boreal winter the surface current just south of the equatorial region flows eastward referred to as the South Equatorial Countercurrent (SECC) while the westward flowing SEC

shifts southward [e.g., Schott and McCreary, 2001; Schott et al., 2009]. The boreal fall westward SEC carries fresh surface water from the Southeast tropical Indian Ocean, to a large part supplied by the Indonesian Throughflow (ITF). In boreal fall to early winter, this sets up a mean positive (negative) meridional salinity gradient south (north) of the equator (Figure 3.3) where the salinity maximum lies a few degrees north of the equator in the central to eastern tropical Indian Ocean. The situation changes in the boreal winter when the equatorial Wyrtki jets cease and flow westward, which marks the westward retreat of the equatorial high salinity tongue. On the other hand, Zhang (2001) and Sato et al. (2007) suggest that the two precipitation belts north and south of the equator create the maximum salinity at the equator. In boreal winter, the ITCZ shifts southward off the equatorial region and is against the westward retreat of the equatorial high salinity tongue. Therefore, here we hypothesize that the meridional variation of horizontal advection and ITCZ-driven precipitation pattern in the tropical Indian Ocean determine the development of the equatorial high salinity tongue in boreal fall. In boreal winter the meridional distribution of the horizontal advection determines the retrogression of the equatorial high salinity tongue.

The authors compute the surface MLS budgets using in-situ observation as well as satellite/ data products to examine whether the meridional variation of horizontal advection or the surface freshwater flux or the combination of both control the development of the equatorial high salinity tongue in boreal fall. We also examine if the meridional variation of the horizontal advection controls the westward retreat of the equatorial high salinity tongue in boreal winter.

Data is described in section 3.2. The equation describing the surface MLS budget and the definition of surface mixed layer are presented in section 3.3. Method and results of each component estimated in the MLS budgets are described in section 3.4. The discussion and summary are described in section 3.5.

3.2 DATA

3.2.1 In-situ moorings

The analysis is conducted using primarily the moored buoy data collected from four moorings in two field experiments in the tropical Indian Ocean: The **DYNA**mics of the **M**adden–Julian **O**scillation (DYNAMO) [Yoneyama et al., 2013] and **R**esearch Moored **A**rray for African-Asian-Australian **M**onsoon **A**nalysis and Prediction (RAMA) [McPhaden et al., 2009]. The two DYNAMO surface moorings, at 0°N 79°E (referred to as D1 hereafter) and 1.5°S 79°E (referred to as D2 hereafter), were deployed in mid-September 2011 and recovered in late January 2012. A complete list of the atmospheric and oceanic observation platforms is described in Moum et al. (2014) and Yoneyama et al. (2013). The detailed specifications of meteorological and oceanic measurements at D1 (0°N 79°E) is summarized in Table 3.1. Meteorological sensors at D1 were vandalized and the CTD sensor at 1 m depth was damaged on 20 November 2011. The two RAMA surface moorings, at 0°N 80.5°E (referred to as R1 hereafter) and 1.5°S 80.5°E (referred to as R2 hereafter), has longer but intermittent record since 2005. Observations obtained from these four moorings (D1, D2, R1, R2) are used for computing the salinity changes, surface freshwater flux, horizontal salinity advection or comparisons with satellite or data products.

3.2.2 Satellite and data products for regional purposes

SSS from Aquarius instrument aboard the SAC-D spacecraft is used to describe the intraseasonal and seasonal salinity variability in the tropical Indian Ocean (https://podaac.jpl.nasa.gov/aquarius). V5.0 of Level-3 7-day mapped SSS with one-degree spatial resolution and rain mask is selected for computing the regional salinity changes. The SSS accuracy after temporal averaging over a month is 0.2 psu on 150km scale. When the rain rate is large (> 0.25 mm/hr), the SSS data are filtered out due to the large biases [Kao et al., 2018; and

personal communication with Hsun-Ying Kao]. Precipitation rate from Tropical Rainfall Measuring Mission (TRMM) 3B42 product with 3-hour temporal resolution and 0.25° spatial resolution (https://pmm.nasa.gov/data-access/downloads/trmm) is used to estimate the surface freshwater flux at the mooring sites and regional area. The monthly oceanic evaporation of the tropical Indian Ocean is obtained from Objectively Analyzed air-sea Fluxes (OAFlux; http://oaflux.whoi.edu/). It is used to estimate the regional surface freshwater flux. The climatology of mixed layer depths is obtained from Argo Mixed Layers (http://mixedlayer.ucsd.edu/). The density threshold, mean mixed layer depth (MLD) product is selected for the use of computing the regional surface freshwater flux. The density threshold for MLDs follows de Boyer Montégut et al. (2004) – 0.03 kg m^{-3} with a reference depth of 2.5 m in the equatorial regions. The near surface current data in the tropical Indian Ocean from Ocean Surface Current Analyses – Real time (OSCAR) is used for describing broader spatial and temporal variations of surface current and for comparing with mooring observations. OSCAR is a processing system and data center to provide operational ocean surface velocity fields from satellite altimeter and vector wind data. The 5-day mean, 1° longitude/ latitude filtered vector current velocity is used in this study.

3.3 Surface Mixed Layer Salinity Budget

3.3.1 Equation of the Salinity Budget

MLS balance is derived based on the heat balance equation described by Moisan and Niiler (1998) and is adapted from Cronin and McPhaden (1998):

$$\frac{\partial S_a}{\partial t} = \frac{1}{h}S_0(E-P) - \vec{v}_a \cdot \nabla S_a - \frac{1}{h}F_{-h} - \frac{1}{h}\nabla \cdot \int_{-h}^{0} \hat{v}\hat{S}\, dz - \frac{1}{h}(S_a - S_{-h})\left(\frac{dh}{dt} + w_{-h}\right) \quad (1).$$

Equation (1) represent the local time rate change of MLS as calculated from the surface freshwater flux (the effect of evaporation minus precipitation in the open ocean), the zonal and

meridional advective salinity fluxes averaged in the surface mixed layer, the turbulent salinity flux at the base of the surface mixed layer h, the divergence of stratified shear eddy flux, and the entrainment [Cronin and McPhaden, 1998; Foltz et al., 2004]. $h = Z_{MLD}$ is the surface mixed layer depth (MLD) which will be defined in 3.2. S_0 is salinity at the ocean surface, which will be represented by observations at 5-m depth for moorings or Aquarius SSS for regional purposes. S_{-h} and S_a are salinity at the base of the surface mixed layer (z = -h) and the average salinity of the surface mixed layer, respectively; E and P are the rates of evaporation and precipitation; $\vec{v}_a$ and $\hat{v}$ are the vertically average velocity of the surface mixed layer and the deviation of velocity from the mean, respectively; F_{-h} is the vertical turbulent diffusion at z = -h; and ∇ is the horizontal gradient operator. Averaged salinity and velocity of the layer are defined according to $X_a(t) = \frac{1}{h}\int_{-h}^{0} X(z,t)\,dz$ at time t.

The time rate change of MLS, surface freshwater flux and horizontal salinity advection are estimated using in-situ moorings except for precipitation from TRMM satellite product described in 3.2.1 and 3.2.2. The zonal average (70°~90°E) of MLS changes, surface freshwater flux and zonal advection in central to eastern Indian Ocean (10°S~5°N) are also estimated from satellites and data products. The turbulent salinity flux at the base of the mixed layer depth during 6~28 October 2011 and 11 November~2 December 2011 is cross referenced with the results of Pujiana et al. (2018), measured by the shipboard Chameleon microstructure profiler close to R1 (0°N 80.5°E). The last two terms in (1) cannot be estimated by the field measurements. Therefore, the actual salinity balance equation applied in this study is expressed as follows:

for the equatorial moorings:

$$\frac{\partial S_a}{\partial t} = \frac{1}{h}S_0(E - P) - \vec{v}_a \cdot \nabla S_a + -\frac{1}{h}F_{-h} + R \qquad (2)$$

for the 1.5°S moorings:

$$\frac{\partial S_a}{\partial t} = \frac{1}{h} S_0 (E - P) - \vec{v}_a \cdot \nabla S_a + R \quad (3)$$

and, for the MLS budget of the zonal average between 70°~90°E:

$$\frac{\partial S_a}{\partial t} = \frac{1}{h} S_0 (E - P) - \vec{u}_a \frac{\partial S_a}{\partial x} + R \quad (4)$$

$\vec{u}_a$ is the vertically average zonal velocity of the surface mixed layer. R is the residual including the un-estimated terms and errors in the computation of estimated terms. For example, R in (4) includes the meridional advection, turbulent mixing at the base of the mixed layer, divergence of stratified shear eddy flux, entrainment and the errors of the estimated terms in (4). The meridional advection is omitted for MLS budget using satellite and data products due to the poor data quality of OSCAR meridional current velocity which will be discussed in 3.4.3.3.

3.3.2 Mixed Layer Depth (MLD)

The base of the surface mixed layer, denoted as $z = -h(t)$, is estimated as the depth where the density is 0.1 kg m^{-3} greater than at 5-m depth for the mooring data. We use observation at 5-m as the reference depth at D1, D2 and R1 instead of using the shallowest instrument depth (1-m). 10-m is chosen as the reference depth for R2 because R2 has no 5-m observation. Using a deeper reference depth would avoid salinity noise due to sharp movement of the surface buoys by surface waves which could cause the 1-m sensor exposed in the air. Furthermore, the 1-m CTD sensor at equator was damaged on 20 November 2011. The choice of using 5-m data as the reference will keep a consistent MLD definition throughout the entire period. This definition is also consistent with that used in Chi et al. (2014) where the surface mixed layer heat budget is described. The surface MLD defined by the 5-m and 10-m reference depths yield similar results for the moorings D1, D2 and R1. The mean difference of the MLD and standard deviation of the MLD difference between the two different reference depths is less than 3.5-m and less than 5.1-

m using hourly temperature and salinity data. On the other hand, Argo MLD described in 3.2.2 is chosen for multi-year MLS budget in deep tropics of the central to eastern Indian Ocean.

3.4 METHODS AND RESULTS

3.4.1 Local Time Rate of Change of Mixed Layer Salinity

The local time rate change of the MLS ($\frac{\partial S_a}{\partial t}$) at the equator are computed as the finite difference of two adjacent daily mean values for D1 and R1 moorings, and at 1.5°S the finite difference of two adjacent daily mean values for D2 and R2 moorings. The zonal average between 70°E~90°E of the time rate change of Aquarius SSS from latitude between 10°S~5°N is also estimated to show the upper ocean salinity changes on monthly to seasonal time scales in the deep tropics of central to eastern Indian Ocean. North of 5°N in Indian Ocean, the landmass of India and Sri Lanka separating the contrasting haline water masses between Arabian Sea and Bay of Bengal (Figure 3.1), hence the zonal averages of the salinity changes are not applied at these latitudes.

3.4.1.1 By Mooring Measurements

At the equator, the local time rate change of MLS is mostly positive in boreal fall from September to November (Figure 3.4), i.e., the mixed layer becomes saltier with time, with large positive pulses of MLS changes every 5~10 days. The peak of the pulses of positive time rate of change is 0.03~0.075 psu/day. Accumulating over the events, it generally leads to an increase of 0.1~0.2 psu over ~1-week period. From December 2011 to early January 2012, the equatorial MLS decreases, and the amplitude of the negative MLS tendency is two to four-fold (0.4~0.7 psu/week) larger than that in boreal fall 2011.

At 1.5°S, the MLS also increases, getting saltier, in boreal fall with the positive pulses every 5~10 days as observed at the equator (Figure 3.4, 3.5). However, these positive pulses cease a few weeks before it does at the equator. The peak for each salty salinity pulses in boreal

fall varies between 0.02~0.07 psu/day, leading to an accumulated increase of 0.1~0.3 psu in a week. Starting around the active phase of the 2nd MJO in late November to around December 11, the MLS decreases by 1 psu within 3 weeks. From January 10 to January 16, the MLS increases drastically by 1 psu in a week. From January 17 to January 21, the MLS decreases quickly by 0.55 psu in 5 days.

The boreal fall MLS increase and boreal winter decrease then increase is consistent with Aquarius SSS from 2011 to 2015 (Figure 3.6a, 3.6c) as well as the long-term, but intermittent RAMA mooring observation at R1 and R2 from 2005-2018 (Figure 3.6b, 3.6d). This boreal fall increase appears to be at all depths above the upper ocean salinity maximum, which can be seen in boreal fall of 2011, 2012, 2014 at R1 and R2 (Figure 3.6b, 3.6d). The Aquarius SSS has a seasonal increase with two small intraseasonal local maxima except for boreal fall 2013 to early 2014 – one sub-seasonal maxima in boreal fall and another in early winter. The Aquarius SSS shows very robust peak near the end of each year, followed by a few months drop, and increases in boreal spring. The in-situ moorings and Aquarius SSS suggest that the equator and 1.5°S MLS correlate well on seasonal time scales and with similar amplitude of changes in MLS. The sub-seasonal variation differs in terms of timing and amplitude between the equator and 1.5°S. Therefore, this suggests that they might be governed by different mechanisms for sub-aseasonal time scales between just 1.5° latitude apart. Interannual variations of the strength of the boreal fall salinity increase and the time of the maximum change rate have been reported, which are presumably associated with the interannual variation of the Wyrtki Jets in the equatorial Indian Ocean [Duan et al., 2016].

3.4.1.2 By Satellite product: Aquarius SSS

In boreal fall, the zonal average of MLS tendency between 70°E~90°E is positive and becomes saltier only within 2° latitude from the equator (Figure 3.7q). The maximal MLS change

increases are located slightly north of the equator, while the rest of deep tropical Indian Ocean freshens. In boreal fall 2011 the equatorial positive MLS change is shifted northward relative to the multi-year average, between 1°S~4°N (Figure 3.7i). The increase in the equatorial ocean and the freshening off the equator depicts the eastward development of the high salinity tongue centered at the central to eastern equatorial Indian Ocean. Moreover, the increase of equatorial MLS from September to November suggests that the high salinity tongue develops more rapidly with time in boreal fall. From September to November, the peak of the positive MLS tendency shifts from north to south of the equator and the positive MLS tendency becomes broader in the latitude span. In boreal winter, except for north of 2°N, the MLS decreases everywhere in the deep tropics with one local maximal MLS decrease in the equatorial band and the another to the south of 4°S. The larger decrease of equatorial MLS resembles the retreat of the high salinity tongue centered at the equator. The freshening to the south of 4°S in boreal fall and winter echoes the a westward developing zonally-oriented freshening band from boreal fall to winter (Figure 3.1).

3.4.2 Surface Freshwater Flux

The evaporation rate is estimated using COARE 3.5 bulk flux algorithm [Fairall et al., 1996; Edson et al., 2013] at the mooring locations and using OAFlux products for the broader area in the tropical Indian Ocean. The precipitation rate for the mooring locations and for the deep tropics of central to eastern Indian Ocean are both obtained from TRMM 3B42 3-hour product with 0.25° spatial resolution. This is a better approach for the estimates of the precipitation at mooring locations because neither of the two equator moorings successfully record the evaporation and precipitation rates after the latter half of November 2011. Monthly precipitation rate measured at the RAMA moorings in the deep tropics (longitude range from 67°E to 95°E

and latitude range from 10°S to 10°N) correlates with TRMM 3B42 products similar to the tropical Pacific TAO/TRITON buoys and TRMM 3B42 [Huffman et al., 2007]. This suggests that the scatters between in-situ and satellite precipitation rates in Indian Ocean is similar to those in the Pacific.

3.4.2.1 At the Moorings

The intraseasonal variability of surface freshening due to freshwater flux is apparent. At both the equator and 1.5°S moorings, the larger freshening effects are associated with active phase of MJOs, which are roughly separated by one month in boreal fall to winter 2011 (Figure 3.4, 3.5). The freshening effect also occurs at the end of September 2011 during rain events that is unrelated to MJOs. Precipitation slightly precedes the arrival of the active phase of MJOs. The evaporation rate is usually two-fold larger during active phase of MJOs than in other periods. However, the precipitation rate increases during active phase of MJOs and overwhelms the evaporation increase so that the combined effect freshens the surface MLS during the active phase of MJOs. Outside of the active phase of MJOs, the evaporation sometimes exceeds precipitation so as to slightly reduce the freshening effects during the suppressed phases of MJOs.

The surface freshwater flux also varies between boreal fall and winter. The mean negative freshwater flux for December 2011 to January 2012 is less than 20% of the negative mean for September to November 2011. That is, at least during the DYNAMO field campaign, the freshwater input in boreal winter is less than boreal fall. One reason for the seasonal difference is that there is only one MJO events in boreal winter while there are two MJO events plus more local rain events in boreal fall. The accumulated evaporation effect is also larger in boreal fall but the amount of difference does not compensate the larger precipitation effect in boreal fall. Even though the surface freshwater flux acts to freshen the MLS throughout most of

the boreal fall and winter in 2011, the MLS still increases. Therefore, other oceanic processes such as horizontal advection and turbulent mixing may play significant roles in rising the MLS.

3.4.2.2 By Satellite and Data Products: OAFlux, TRMM and Argo Mixed Layer

The deep tropical central to eastern Indian Ocean is within the warm Indo-Pacific warm pool, extending from roughly 60°E to the dateline that covers most of the tropical Indian ocean as well as the western tropical Pacific [Raymond and Fuchs, 2018]. In the central to eastern equatorial Indian Ocean, precipitation often exceeds the evaporation for time scales longer than a few days. In boreal fall and winter, the latitude bands receiving more precipitation do not coincide with the larger evaporation (Figure 3.7e~f, 3.7n~o). In other words, the meridional distribution of the evaporation rate does not match the distribution of the precipitation rate in both boreal fall and winter. In boreal fall, the precipitation rate in the deep tropics is quite homogeneous in meridional direction compared to boreal winter (Figure 3.7e, 3.7n). It is consistent with the weak signals of the double ITCZ over the tropical Indian Ocean that only exists during November [Zhang, 2001]. The precipitation rate is slightly larger at 4°S and 2°N with a precipitation minimum near the equator. In boreal winter the higher precipitation shifts southward in the deep tropics while decreases in the equatorial region. The meridional shifts of the larger precipitation with season in the deep tropics of central to eastern Indian Ocean echoes the southward migration of the ITCZ [Nyadjro and Subrahmanyam, 2016]. The evaporation rate is larger in boreal fall than winter everywhere in the deep tropics (Figure 3.7f, 3.7o), yet the magnitude is in general two to four-fold smaller than the precipitation rate. Therefore, the meridional distribution of the surface freshwater flux is primarily determined by the distribution of the precipitation rate. The surface freshwater flux freshens the MLS homogeneously in boreal fall and freshens more in the southern deep tropics while less in the equatorial region (Figure 3.7g, 3.7p).

3.4.3 Vertically Averaged Horizontal Advective Salinity Flux

3.4.3.1 Methods by Mooring Measurements

The horizontal salinity gradient, $\nabla \cdot S_a = (\frac{\partial S_a}{\partial x}, \frac{\partial S_a}{\partial y})$, is estimated as the finite difference of salinity between the mooring pairs separated by 1.5° longitude or latitude. $\frac{\partial S_a}{\partial x}$ at the equator is estimated using observations taken by the two moorings at D1 (0°N 79°E) and R1 (0°N 80.5°E). $\frac{\partial S_a}{\partial x}$ at 1.5°S is computed using observations taken from the two moorings at D2 (1.5°S 79°E) and R2 (1.5°S 80.5°E). $\frac{\partial S_a}{\partial y}$ at 79°E is estimated using observations taken from the two mooring at D1 (0°N 79°E) and D2 (1.5°S 79°E). $\frac{\partial S_a}{\partial y}$ at 80.5°E is estimated using observations taken from the two moorings at R1 (0°N 80.5°E) and R2 (1.5°S 80.5°E). The horizontal salinity advective flux is the dot product of the horizontal velocity vector and the salinity gradient vector. The zonal advection along the equator (1.5°S) is computed as the product of the mean zonal current velocity at the equator (1.5°S) and the zonal MLS gradient at the equator (1.5°S) mentioned above. The meridional advection at the equator moorings (1.5°S moorings) is the mean of two separate estimates: one is the product of the meridional velocity at 0°N 79°E (1.5°S 79°E) and $\frac{\partial S_a}{\partial y}$ along 79°E, and another is the product of the meridional velocity at 0°N 80.5°E (1.5°S 80.5°E) and $\frac{\partial S_a}{\partial y}$ along 80.5°E. Since the four moorings only provide the meridional gradient, $\frac{\partial S_a}{\partial y}$, between the equator and 1.5°S, this is linearly adjusted to the $\frac{\partial S_a}{\partial y}$ centered at the equator and at 1.5°S. Using a linear regression of $\frac{\partial S_a}{\partial y}$ from Aquarius SSS between 1° separation south of the equator to a 1° separation centered at the equator (Figure 3.8a, b). In a similar fashion, the linear adjustment of the $\frac{\partial S_a}{\partial y}$ at 1.5°S is from the linear regression of $\frac{\partial S_a}{\partial y}$ from the 1° separation $\frac{\partial S_a}{\partial y}$ north

of 1.5°S to $\frac{\partial S_a}{\partial y}$ centered at 1.5°S. This approach in estimating horizontal gradients is better than just using Aquarius directly because the error of individual Aquarius salinity measurements (O(0.2 psu)) is larger than the salinity gradients (O(0.1 psu) or less) on 1° spatial scale. The reduced magnitude of $\frac{\partial S_a}{\partial y}$ after linear adjustment also illustrates that the mean salinity maximum in the deep tropical central to eastern Indian Ocean is slightly north of the equator (Figure 3.1, 3.3).

3.4.3.2 Mixed Layer Currents, Horizontal MLS Gradients and Advection Estimates Using mooring measurements For September 2011 – January 2012

3.4.3.2.1 Mixed Layer currents

In boreal fall, the mixed layer current mostly flows eastward at the equator and 1.5°S moorings (Figure 3.9, 3.10, also see Chi et al., 2014) while the meridional velocities oscillate with a magnitude larger than the weak southward meridional mean flow. The magnitude and direction of the upper ocean currents vary richly at sub-monthly time scales. The equatorial zonal currents increased from ~0 to ~0.6 m/s in late September. From October to mid-November, the equatorial zonal current oscillates about 0.6 m/s with 10~15-day cycle that could be due to bi-weekly waves [Sengupta et al., 2004; Miyama et al., 2006]. The equatorial zonal current then decreases to ~0.3 m/s before the active phase of MJO2 in late November. On the top of the bi-weekly variability in October to mid-November, the two equatorial zonal currents are out of phase and oscillating with a higher frequency than one week. The direction of the meridional currents between the two equatorial moorings are also out of phase and sometimes opposite in direction at times, suggesting small-scale features appearing at scales of a few hundred kilometers. The two 1.5°S zonal currents increases from ~0 m/s in late September to ~0.8 m/s in early November with 10~15-day cycle that could also due to bi-weekly waves (Figure 3.10). However, the zonal current oscillations with a cycle less than one week do not appear at 1.5°S currents. The zonal

currents decrease in the first half of November to a minimum ~0.25 m/s before the active phase of MJO2. In meridional direction the two 1.5°S moorings agree with one another in terms of magnitude and trend. This contrasts with the two equator meridional currents, suggesting that in meridional direction horizontal scales are small and dynamics are partially different with just 1.5° apart. That is, the small-scale feature affecting the equatorial moorings has meridional scale smaller than 1.5°.

From the end of boreal fall to the early boreal winter, the equatorial and 1.5°S zonal current accelerates from ~0.25 m/s to ~1.3 m/s. The mean meridional current at the 1.5°S moorings is accelerated northward. The equatorial zonal current increases by ~1 m/s during the week of active phase of MJO2, associated with the active phase of the MJO2 when strong surface eastward winds accelerate the surface ocean (Chi et al., 2014; Pujiana et al., 2018). The 1.5°S zonal currents do not increase as much as the equatorial zonal currents during the active phase of MJO2 in a week. Within a month between the active phase of MJO2 to mid-December, zonal currents at 1.5°S increase by ~1 m/s with a large amplitude of 0.4~0.5 m/s, 10~12-day sub-monthly oscillation.

In the following 2~3 weeks in December, the equatorial mooring locations are affected by the 6~7-day wave activities excited by the northwest moving tropical storm. Therefore, these waves are likely inertial gravity waves [e.g., Price et al., 1994]. This storm is number 9 of 2011 in North Indian Ocean according to NOAA IBTrACS. During the first 2~3 weeks of the wave activities in December, the equatorial zonal and meridional velocities oscillated with a cycle of 6~7 days. Both zonal and meridional velocities between D1 and R1 are out of phase, suggesting that the zonal scale of the wave activities is a few hundred kilometers. Unlike the equatorial mooring locations in the first 3 weeks of December, the 1.5°S mooring locations are not clearly affected by the 6~7-day waves excited by the northwest moving tropical storms. Later in

December, the equatorial and 1.5°S eastward currents start decreasing and eventually reverse direction in late January.

3.4.3.2.2 Horizontal MLS Gradients

In boreal fall, the mean zonal MLS gradient at the equator and 1.5°S moorings are negative (Figure 3.9, 3.10), i.e., fresher to the east in the central equatorial Indian Ocean. The zonal MLS contrast, i.e., negative zonal MLS gradient, decreases with the progress of boreal fall (Figure 3.2). The meridional MLS gradients at the southern flank of the equator, between D1 and D2 as well as R1 and R2, are mostly positive in boreal fall for the high salinity tongue develops along the equator. The sub-monthly variation of the zonal MLS gradient is larger than the mean zonal MLS gradient. However, the sub-monthly variation of the meridional MLS gradient is of same order of magnitude as the mean meridional MLS gradient. At the equator, the MLS zonal gradients are in general negative in boreal fall with occasionally a few days of positive MLS zonal gradients. In the first three weeks of October, the zonal MLS gradient at 1.5°S is small and positive and it becomes large and negative in November. The mean meridional MLS gradient increases in October and decreases in November before the active phase of MJO2.

Starting from the last week of November 2011, the magnitude of the equatorial zonal MLS gradient increases two to three-fold with large amplitude of 6~7-day oscillation. This large oscillation of equatorial horizontal gradients is due to small-scale wave activities mentioned in section 3.4.3.2.1. During the small-scale wave activities in December, the mean meridional gradients increase and the gradients between R1 and R2 (80.5°E) lags the gradients between D1 and D2 (79°E) by 1~2 days. However, the variation of zonal MLS gradient at 1.5°S is different from the equator. The magnitude of zonal MLS gradient at 1.5°S decreases from positive to negative from mid-November to December. It does not show the robust 6~7-day oscillation in the first three weeks of December as at the equator.

In boreal winter, the mean equatorial zonal MLS gradient becomes an order of magnitude smaller than in boreal fall but the intraseasonal oscillation magnitude increases significantly. The oscillation cycle of the equatorial zonal MLS gradient increases from 6~7 days in the first three weeks of December to 10~12 days in late December to January. The 1.5°S zonal MLS gradient is more negative than at the equator. The 1.5°S mean meridional MLS gradient becomes three-fold more negative, consistent with the fact that the meridional MLS gradient reaches the annual maximum later in boreal fall to early winter (Figure 3.3).

3.4.3.2.3 Horizontal Advection

Throughout the boreal fall, the equatorial zonal advection increases the MLS despite a few periods of drop when the small-scale zonal MLS gradient is positive, and currents flow eastward (Figure 3.4, 3.9). The zonal advection contributes to an increase of ~0.4 psu MLS, which is ~40% of the MLS increase in boreal fall. The meridional advection contributes another ~40% of MLS increase in boreal fall by the combination of pulses of southward currents and positive meridional gradients, which transports saltier water from the north when the high salinity tongue is centered slightly north of the equator. At the 1.5°S moorings, the zonal advection is small and negative for the first half of the boreal fall due to a positive mean zonal MLS gradient (Figure 3.5, 3.10). It becomes large and positive for the first 2~3 weeks of November. The zonal advection contributes to an increase of ~0.65 psu MLS from September to mid-November, which is ~100% of the boreal fall MLS increase. The meridional advection is relatively small.

In mid-November to the first half of December, the horizontal advection acts differently between the equator and 1.5°S. The equatorial zonal advection continues to become saltier until the middle of the active of MJO2 when it starts to freshen the MLS and be affected by the small-scale wave activities excited by the tropical storm mentioned in section 3.4.3.2.1. The equatorial zonal advection correlates with the MLS tendency with 1~2 days lag in time. However, the 1.5°S

zonal advection acts to freshen the MLS by ~ 1 psu in one month, which is ~80% of the MLS decrease in this period. The 6~7-day oscillation in the equatorial zonal advection is persistent in the first three weeks of December but the oscillation is not seen at 1.5°S.

The reverse of the equatorial zonal advection (freshens the MLS) in December 2011 is consistent with the locally positive zonal SSS gradient for the multi-year mean of December (Figure 3.1). Throughout boreal winter, the equatorial zonal advection on average contributes negatively to MLS but the 1.5°S zonal advection still contributes positively to MLS. It is out of phase with the MLS tendency from late December to January. The mean equatorial meridional advection transports saltier water from the north, equivalent to 0.1~0.2 psu of MLS increase, except during the period when the mean meridional current flows northward. However, in winter the meridional advection at 1.5°S contributes to ~ 1 psu decrease of MLS, opposite to but of the same magnitude as the 1.5°S zonal advection. The large freshening effect by the meridional advection is due to the combination of larger mean northward flow and mean positive meridional gradient at 1.5°S.

Overall in boreal fall, the horizontal advection at equator transports saltier water from west by the developing eastward Wyrtki Jet, and from north by the mean southward but reversing meridional component. The direction of the equatorial zonal advection is determined by the local zonal gradient as the zonal current is eastward until the seasonal eastward Wyrtki Jet ceases in January. However, the direction of the meridional advection is determined by the direction of the meridional currents for the meridional gradients are mostly positive. The mean equatorial meridional current is southward while the 1.5°S meridional current becomes stronger in boreal winter. The large oscillation of the equatorial horizontal advection in December 2011 is affected by local wave activities excited by a tropical storm travelling northwest. However, the

result suggests that the meridional scale of the wave activities is small and the dynamics that contributing to the local MLS budgets with 1.5° apart is different.

3.4.3.3 By Satellite and Data Products: Aquarius Sea Surface Salinity and OSCAR

Figure 3.7 summarizes 70°~90°E zonal average of the monthly mean, boreal fall and winter averages for near surface currents, SSS, zonal SSS gradient, equivalent MLS changes due to zonal advection, precipitation, evaporation, equivalent MLS changes due to surface freshwater flux, and MLS tendency. Here MLS is assumed to be equivalent to SSS. The meridional MLS advection is excluded because of the poor quality of the OSCAR meridional currents in the deep tropics of central to eastern Indian Ocean compared to the RAMA moorings (Figure 3.8d).

In boreal fall, the eastward jet is centered at the equator (Figure 3.1) while the center of the eastward jet for individual years might deviate slightly off the equator (Figure 3.7a, 3.7j). The equatorial eastward jet is roughly 5° wide and is more developed in October to November. In December the meridional span of the eastward jet increases and the center of the jet shifts slightly to south of the equator. South of the equatorial the eastward jet, the zonal current flows westward, referred as to SEC. The zonal SSS gradient is mostly negative and the contrast increases towards the north for the closeness to the salty Arabian Sea and fresh Bay of Bengal (Figure 3.7c, 3.7l). Therefore, the zonal advection brings saltier water to the equatorial regions with the maximum around 2°N (Figure 3.7d, 3.7m) and otherwise relatively small for the combination of the currents and smaller zonal MLS gradients.

In boreal winter, the zonal currents in the deep tropical central to eastern Indian Ocean reverse. The equatorial eastward current ceases and reverses roughly between the end of December to early January. To the north of the equatorial band the zonal currents flow westward as the winter monsoon kicks in. South of the equatorial band between 1°S and 6°S, the zonal currents flows eastward, referred as to SECC. To the south of 6°S in the southern tropical Indian

ocean the zonal currents flow westward, which is the South Equatorial Current (SEC) as identified in the previous studies. The zonal MLS gradient does not change much from the boreal fall except that the magnitude for those north of the equator decreases. The resulting zonal advection within the equatorial band no longer contributes positively to MLS but instead slightly contributes negatively to MLS in the equatorial band and northern side of the deep tropics (Figure 3.7d, 3.7m).

3.4.4 Turbulent Flux at the Base of Mixed Layer and Residual

The results of Pujiana et al. (2018), measured by the shipboard Chameleon microstructure profiler, are used to estimate the equatorial turbulent flux at the base of mixed layer. Their results are converted and added on Figure 3.4 whenever available (Figure 3.4). The cumulative MLS change due to turbulent mixing at the base of mixed layer usually acts to transport saltier water from below the mixed layer. In the three weeks of October 2011, mid-November and the last week of November 2011, the turbulent mixing contributes to ~0.26, ~0.13 and ~0.28 psu increase to the MLS. On the other hand, the residual during the 3 periods when turbulent flux is cross referenced is ~0.18, ~0.08, and ~0.14 psu of increase to the MLS. Note the residual in Figure 3.4 consists of the un-estimated terms (i.e., turbulent mixing at the base of the mixed layer, divergence of stratified shear eddy flux, and entrainment) and the errors from the estimated terms in (2) (i.e. MLS tendency, surface freshwater flux, and horizontal advection). The accumulation of the residual flux for the three period in boreal fall 2011 is consistent with the turbulent flux at the base of the mixed layer although the residual 30~50% less than the turbulent flux at the base of the mixed layer. The difference between the two is less than the errors from the turbulent mixing estimation, which is often the same order as the estimated values (e.g.,

Perlin and Moum, 2012). Therefore, the turbulent flux at the base of the mixed layer could be responsible for the residual of the equatorial mooring budget in boreal fall.

3.4.5 The Mixed Layer Salinity Budget

3.4.5.1 At the moorings

In boreal fall 2011, the equatorial MLS budget is roughly closed evaluated using in-situ measurements and the satellite precipitation rate (Figure 3.4). In boreal fall 2011, the equatorial MLS increases by the combined effects of horizontal advection and turbulent mixing at the base of the mixed layer despite the surface freshwater flux continuously acting to freshen to MLS. The 1.5°S MLS budget in boreal fall 2011 cannot be closed (Figure 3.5). The budget does not identify the cause of the MLS increase in September and October 2011 when horizontal advection and surface freshwater effects are relatively small and act to decrease the MLS. One of the candidates could be turbulent mixing at the base of the mixed layer. In the first three weeks of November, the MLS increases by zonal advection.

In boreal winter, the turbulent mixing flux at mooring locations are not known and therefore the budget cannot be closed. In addition, in the first 2~3 weeks in December 2011 the equatorial mooring locations are affected by small-scale wave activities excited by a tropical storm slightly north of the equator and drives very large variation in current velocities and horizontal MLS gradients (Figure 3.9). The spatial sampling resolution of the moorings is not adequate to capture the horizontal advection induced by the small-scale wave activities. Despite the fact that equatorial MLS budget cannot be closed in boreal winter, the equatorial MLS decreases partially due to the reverse zonal advection and the surface freshening effect while the meridional advection still acts to make the mixed layer saltier. From the last week of November to the first half of December, the 1.5°S MLS decreases primarily by the horizontal advection. From the second half of December to January, both zonal and meridional advection are large but

in opposite sign and therefore compensate one another while the surface freshwater effect still acts to freshen the MLS. However, the sharp increase in mid-January 2012 is unexplained by the estimated horizontal advection nor surface freshwater effect. Again, one of the candidates could be turbulent mixing at the base of the mixed layer.

3.4.5.2 By Satellite and Data Products (S/DP)

The qualitative conclusion between the boreal fall mooring estimates and S/DP estimates in the equatorial region are consistent: the MLS increase in boreal fall is partially due to zonal advection in the equatorial region yet the surface freshwater effects acts to freshen the MLS (Figure 3.11a, c). In boreal fall, the zonal average between 70°E and 90°E MLS budget in the deep tropics is roughly closed south of ~1°N by zonal advection and surface freshening effects using S/DP data. The MLS increase at the equatorial region and MLS decrease to the south is determined by the sign of zonal advection (Figure 3.7d, 3.7m). However, the MLS decrease north of ~1°N cannot be fully explained by the zonal advection and surface freshening effects using S/DP data. Although the MLS budget is closed in the equatorial region using S/DP data, the relative strength of S/DP MLS tendency and zonal advection is opposite of the equatorial mooring results. The S/DP equatorial zonal advection is twice of the MLS tendency while the mooring equatorial zonal advection only explain less than half of the MLS tendency in the boreal fall. The S/DP MLS budget at 1.5°S is more consistent with the 1.5°S mooring MLS budget in terms of the relative strength of the dominant processes. The boreal fall MLS budget is closed at 1.5°S by the positive zonal advection, negative surface freshening effects and a relatively small residual. Therefore, the S/DP observation are only adequate for qualitative understanding of the MLS tendency, zonal advection and surface freshwater flux in the equatorial region in boreal fall.

The qualitative conclusion between the boreal winter mooring estimates and S/DP estimates are not consistent in the equatorial region (Figure 3.11b, d). In boreal winter, the S/DP MLS budget in the deep tropics does not close by zonal advection and surface freshening effects alone. Compared to boreal fall, the winter equatorial zonal advection is reduced (~0) but do not contribute to the MLS decrease as estimated at the equatorial moorings. The residual slightly to the south of the equator for the S/DP MLS budget is negative and almost as large as the negative MLS tendency. Therefore, the major freshening effect in boreal winter is missing for the S/DP MLS budget. The 1.5°S mooring budget result suggests that the large residual slightly to the south of the equator from the S/DP MLS budget is due to the exclusion of the large and negative meridional advection in boreal winter. The MLS decreases to the south of ~5°N yet small is contributed by the increased surface freshening effects in boreal winter and negative zonal advection plus the positive residual consisting of un-estimated terms or errors. In the deep tropics, the meridional variation of the MLS tendency in boreal winter is largely determined from those are not estimated, such as meridional advection and turbulent mixing at the base of the mixed layer or errors. Therefore, in boreal winter the S/DP observation are only adequate for qualitative understanding of the MLS tendency and surface freshening effects in the equatorial region. The estimated zonal advection to MLS tendency ratio using S/DP data is too large compared to the in-situ estimation. The exclusion of the large meridional advection could result in large negative residual in boreal winter MLS budget.

3.5 Discussion and Summary

3.5.1 MLS Budgets and moorings and S/DP products

We estimate the oceanic surface MLS budget in the central equatorial Indian Ocean using four in-situ moorings from DYNAMO and RAMA during September 2011 to January 2012 and the

turbulent mixing results are from Pujiana et al. (2018) for several weeks in October and November 2011. We also use the satellite (Aquarius, TRMM) and data products (OSCAR, OAFlux, Argo mixed layer) to estimate the MLS budget in the deep tropics of central to eastern Indian Ocean in boreal fall and winter between 2011 to 2015. Unlike the quasi-one-dimensional controlled surface mixed layer temperature and heat variation in the boreal fall and winter in the central equatorial Indian Ocean, the three-dimensional processes are all crucial to the surface MLS variation in this region. In boreal fall, the in-situ observation and satellite/ data products conclude that the MLS increases at the central to eastern equatorial Indian Ocean by horizontal advection and turbulent mixing yet the surface freshwater effects acting to reduce the MLS. In boreal winter 2011, the MLS decreases in the equatorial band but the mechanisms differ between the equator and slightly south of the equator at 1.5°S. At the equator, the reverse of zonal advection drives the MLS decrease while the meridional advection and surface freshwater effects act indifferently between boreal fall and winter season. At 1.5°S, the meridional advection drives the MLS decrease while zonal advection and surface freshwater effects contributes similarly between boreal fall and winter season.

The MLS budget at the equatorial moorings is closed in boreal fall by the positive horizontal advection and turbulent fluxes and the opposing surface freshening effects. In boreal winter the equatorial MLS budget can qualitatively be explained by the reverse of the zonal advection but is complicated by the small-scale wave activities excited by the northwest moving tropical storm passed by at the end of November 2011. The MLS budget at 1.5°S moorings cannot be closed in early boreal fall nor winter 2011. One of the possible candidates for the positive accumulation of the residual in early boreal fall and in January 2012 is the turbulent mixing at the base of the mixed layer. The 1.5°S mooring budget roughly closes in the first half

of the boreal winter, presumably because this area is not affected by the small-scale wave activities as at the equator and the turbulent flux at the base of the mixed layer is minor.

The zonal advection at the equatorial region is the key to the boreal fall development of the zonally-oriented high salinity tongue when seasonal eastward Wyrtki Jet centered at the central to eastern equatorial Indian Ocean is accelerated. The mean zonal MLS gradient is negative, with MLS decreasing eastward across the basin scale salinity difference. The zonal MLS difference increases northward toward the salty Arabian Sea and fresh Bay of Bengal so that the boreal fall high salinity tongue is slightly north of the equator.

The retreat of the equatorial high salinity tongue in boreal winter is contributed by different mechanisms at the equator and 1.5°S moorings. At the equator, the westward retreat is due to the reverse of the zonal advection that transports fresher westward water at the equator region. In late December to January when the eastward equatorial jets begin to deaccelerate, the local zonal salinity gradient is positive since the two equatorial moorings locate at the eastern side of a mean zonally local minimum salinity region on the equatorial high salinity tongue (Figure 3.1). The spatial sampling for computing the zonal salinity gradient becomes sensitive when there are local salinity extreme values. The horizontal advection estimated by local small-scale measurements in the vicinity of salinity extreme values may only explain the local phenomena for the short period of time (e.g., sub-monthly time scales). Temporal averaging is needed for further interpreting the zonal MLS advection for the central equatorial Indian Ocean. At the 1.5°S, the boreal winter MLS decrease is due to negative meridional advection that transports fresher water from the southern side when the seasonally meridional current flows north. Slightly south of the equator, the seasonal meridional surface currents are expected to flow northward for the prevalent equatorial westerly winds and some are associated with MJOs in boreal fall and winter. In addition, the seasonal ITCZ becomes more centralized and moves

southward in boreal winter. The boreal winter ITCZ locates at 5°S~10°S so it contributes to positive meridional salinity gradient between the equator and the seasonal ITCZ. However, because of the poor quality of OSCAR meridional current in the deep tropics of central to eastern Indian Ocean, we exclude estimating the S/DP meridional advection. Therefore, the boreal winter S/DP MLS budget does not capture the mechanisms which contribute to the westward retreat of the high salinity tongue slightly south of the equator. The turbulent mixing is also crucial to the variation of MLS at the equatorial Indian Ocean albeit sparsely measured.

The distribution of salt in the equatorial Indian Ocean and its variability may potentially affect the upper ocean stratification hence the air-sea interaction, and the development of eastward Wyrtki Jet (Han et al., 1999; Masson et al., 2003). However, it is challenging to quantify the causes for the development and retreat of the zonally-oriented high salinity tongue as well as the effects in the upper ocean stratification in boreal fall and winter using the satellite and data products with the spatial resolution in the order of 100 km. The zonal MLS advection estimated by satellite and data products only qualitatively explain the development of the high salinity tongue in boreal fall. In addition, local small-scale events could also complicate the attempt to close the MLS budget at sub-seasonal time scales due to inadequate spatial sampling resolution. The sub-seasonal and seasonal surface MLS is largely determined by the internal oceanic processes such as horizontal advection and turbulent mixing at the base of the layer, while the surface mixed layer temperature and heat is controlled mostly by one-dimensional boundary processes at the surface and the base of the mixed layer. Therefore, for data products and models to be accurate, they should properly express the strength and timing of the Wyrtki Jets and the horizontal salinity gradient and should have spatial resolutions at least one-degree and temporal resolution of a few days in order to simulate and predict the MLS changes and therefore the upper ocean stratification in the equatorial Indian Ocean.

3.5.2 The barrier layer formation in late fall-early winter at central equatorial Indian Ocean

The upper ocean undergoes large variations in its temperature and salinity structures in boreal fall and winter in the central equatorial Indian Ocean (Figure 3.12). It is mostly owing to the large horizontal advection. In boreal winter 2011-2012, these changes increase the salinity stratification in the upper 20~30 m while decreases the temperature stratification everywhere above the deepened isothermal layer. Therefore, the barrier layer becomes quasi-permanent in boreal winter and increases to 20-40 m thick after the MJO2 at the end of November to early December 2011 [Chi et al., 2014]. During the MJO2, the mixed layer heat budget is dominant by one-dimensional process that cools the layer by the surface heat flux and the turbulent flux at the base of the layer [Chi et al., 2014]. The upper ocean is vigorously turbulent and the mixed layer becomes deeper of which the temperature and salinity is well mixed. In late boreal fall to early boreal winter, the thermocline also becomes deeper. During this period, the upper ocean above the upper thermocline has little temperature stratification and sometimes appears to have temperature inversion, which is consistent with the multi-year RAMA T-S plots (Figure 3.12). In contrast, the MLS budget is controlled by three-dimensional processes so that the horizontal advection is also important. Therefore, we expect that the horizontal advection is important to the formation and erosion of the barrier layer in late boreal fall to early winter in the central equatorial Indian Ocean.

There are several possible reasons that the barrier layer in the central equatorial Indian Ocean becomes persistent in boreal winter [Cronin and McPhaden, 2002]. The first candidate that helps to form the barrier layer is the horizontal advection ($-U \cdot \nabla S_z$ and $-U \cdot \nabla T_z$). The equatorial mooring MLS budget indicates that the zonal advection changes from eastward to westward while the meridional MLS advection transports fresher water from south of the equator. When the saltier and heavier water mass to the northwest meets the fresher and lighter

water in the central equatorial Indian Ocean, it could turn the horizontal salinity gradient into vertical salinity gradient and shoals the halocline within the isothermal layer. The second candidate that helps to form the barrier layer is related to vertical velocity and the vertical derivative of salinity and temperature stratification ($-wS_{zz}$ and $-wT_{zz}$). The mean vertical velocity in this season moves downward due to the Ekman convergence induced by prevalent westerly winds along the equatorial Indian Ocean (Figure 3.13). And the temperature stratification decreases towards the sea surface while the salinity stratification increases toward the sea surface. The third candidate that helps to form the barrier layer is the surface freshening effect (precipitation) that creates the near surface halocline. There are several possible mechanisms for the barrier layer erosion. The first candidate that hinders the barrier layer formation is the tilting effect ($-U_z \cdot \nabla S$ and $-U_z \cdot \nabla T$). When westerly wind stress accelerates the eastward surface currents and increases sheared flow that leads to surface-intensified salty water advection. The second candidate that hinders the barrier layer formation is the stretching effect ($-w_z S_z$ and $-w_z T_z$). The vertical divergence is positive for the downward velocity increases with depth. And the temperature stratification is small or sometimes inversed while the salinity stratification is always negative above the isothermal layer. Albeit further investigation needs to confirm the relative contribution of the mechanisms in controlling the barrier layer formation and erosion, the MLS budget result suggests that the formation and erosion of the barrier layer are related to three-dimensional processes.

Table 3.4. The mooring specification with more details on the D1 (0°N 79°E), D2 (1.5°S 79°E), R1 (0°N 80.5°E), R2 (1.5°S 80.5°E).

Note that only the information down to 100 m depth and between September 2011 to February 2012 is stated here. Temperature and salinity are measured by CTD*. Oceanic currents are measured by ADCP** and DVS*** at DYNAMO moorings and by ADCP and Doppler current meter at RAMA moorings.

<table>
<tr><th></th><th colspan="2">DYNAMO
0° 79°E (D1)</th><th>DYNAMO
1.5°S 79°E (D2)</th><th>RAMA
0° 80.5°E (R1)</th><th>RAMA
1.5°S 80.5°E (R2)</th></tr>
<tr><td>Temperature</td><td colspan="2" rowspan="2">1, 5, 10, 15, 20, 30, 40, 50, 60, 70, 80, 90, 101 m. Available every 2 min.</td><td>1, 5, 10, 13, 20, 40, 43, 60, 80, 100 m. Available every 10 min.</td><td>1, 10, 13, 20, 40, 60, 80, 100 m. Available every day. 1 m is available every 10 m.</td></tr>
<tr><td>Salinity</td><td>1, 5, 10, 20, 40, 60, 100 m. Available every hour.</td><td>1, 10, 20, 40, 60, 100 m. Available every day.</td></tr>
<tr><td>Oceanic currents</td><td colspan="2">Vertical resolution is 0.5 m from 2-19 m (for DVS, 1200-kHz ADCP), 2 m from 20-100 m (for 300-kHz ADCP). Available every 2 min.</td><td>Current-meter: 10, 40 m. ADCP: 5 m vertical resolution from 25-100 m. Available every 20 min-1 hour.</td><td>Current-meter: 10 m. Available every day.</td></tr>
<tr><td>Precipitation</td><td colspan="2" rowspan="4">2-3 m above sea surface. Available every 10 min.</td><td>3.5 m above sea surface. Available every 10 min.</td><td>3.5 m above sea surface. Available every 10 min.</td></tr>
<tr><td>Air temperature, relative humidity, wind</td><td>3-4 m above sea surface. Available every 10 min.</td><td>3-4 m above sea surface. Available every 10 min except for wind available every day.</td></tr>
<tr><td>Incoming solar radiation, incoming long wave radiation</td><td>Same as RAMA precipitation.</td><td>3.5 m above sea surface. Available every 2 min.</td></tr>
<tr><td>Barometric pressure</td><td>3 m above sea surface. Available every hour.</td><td>N/A</td></tr>
</table>

* CTD: Conductivity-Temperature-Depth.
** ADCP: Acoustic Doppler Current Profiler. It consists of an upward-looking 1200-kHz ADCP at 19 m depth, an upward-looking 300-kHz ADCP at 100 m and an upward-looking 75-kHz ADCP at 600 m depth on the subsurface moorings that were 5-15 km away from the DYNAMO surface moorings.
*** DVS: Doppler Volume Sampler. There are DVS at 3 m and 8 m depth on the surface moorings.

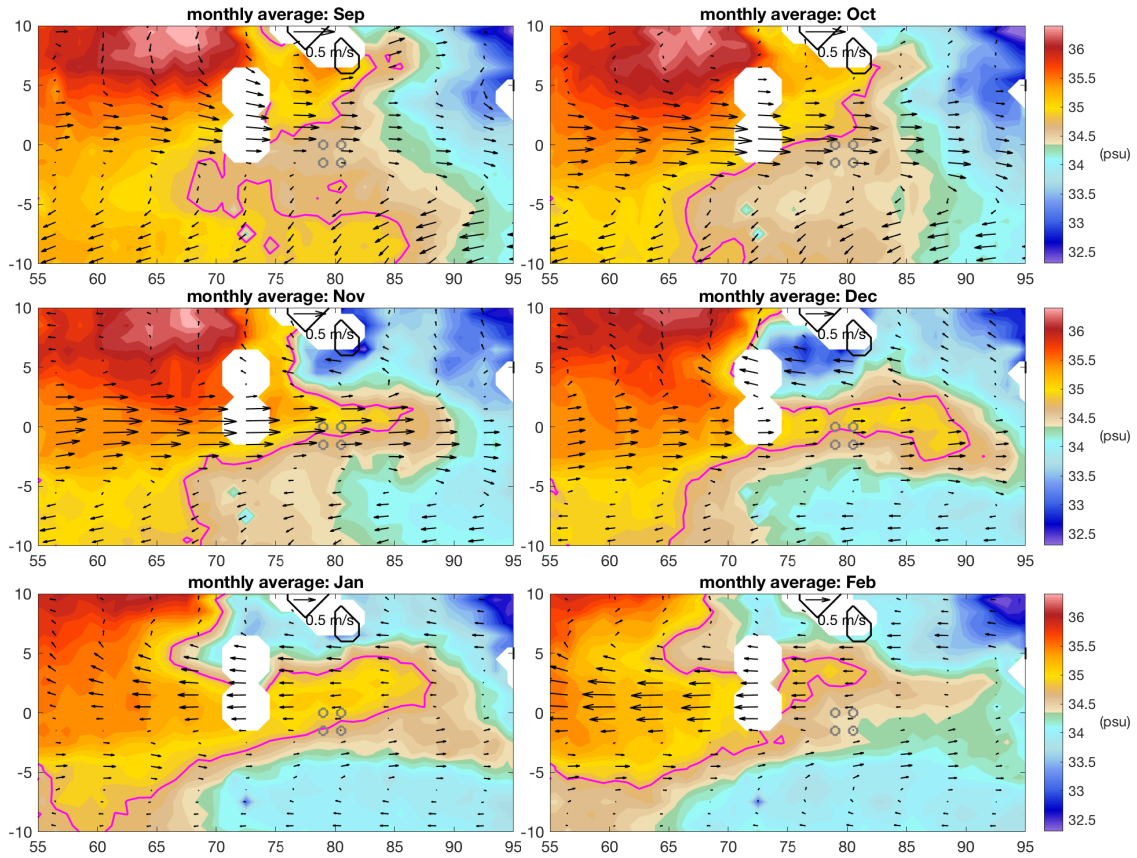

Figure 3.1. Monthly mean Aquarius L3V5 SSS and OSCAR currents.

Monthly mean sea surface salinity (color shading) from Aquarius L3 V5 and OSCAR near surface current velocities (vectors) for September 2011 to June 2015. Gray circles mark locations of DYNAMO and RAMA moorings. A reference velocity vector of 0.5 m s^{-1} is shown. The magenta contour shows 34.8 psu sea surface salinity.

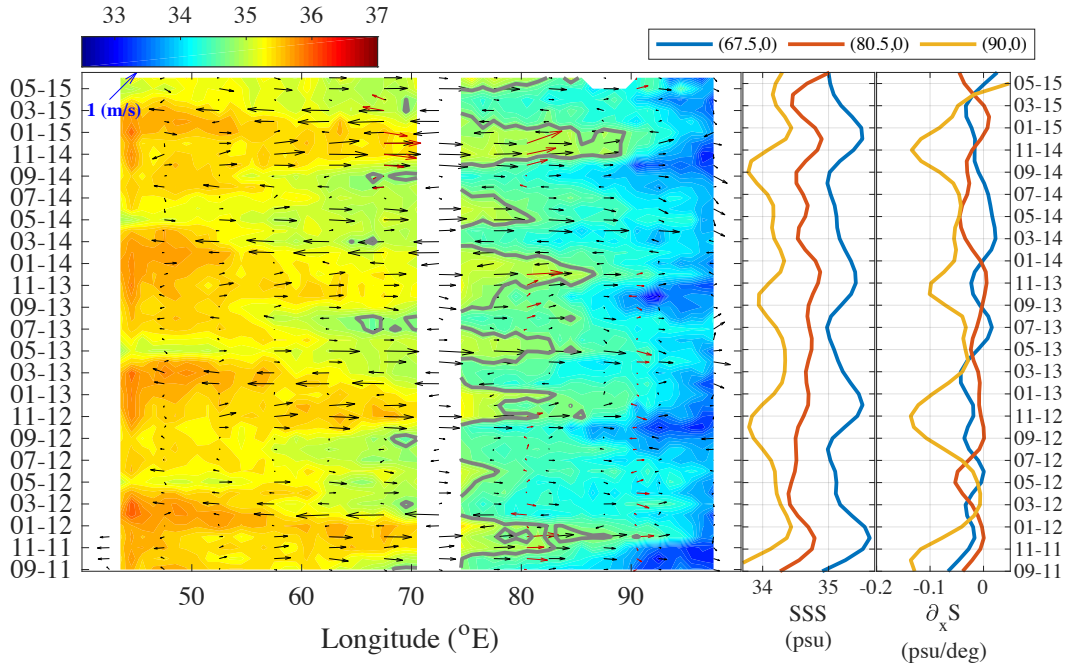

Figure 3.2. Time – longitude plot of Aquarius SSS, OSCAR currents and RAMA moorings currents. Timeseries of Aquarius SSS and zonal SSS gradient at three longitudes along the equator.

The left panel is the time – longitude plot of Aquarius SSS (color shading) and OSCAR near surface current (black vectors) averaged between 0.5°S and 0.5°N. In-situ near surface (10-m depth) monthly current velocities taken from RAMA moorings at 0°N 67°E, 0°N 80.5°E and 0°N 90°E are shown as red arrows. The right panels show the Aquarius SSS at three RAMA mooring locations, and the zonal SSS gradient over 4° longitude centered at three RAMA equatorial mooring locations.

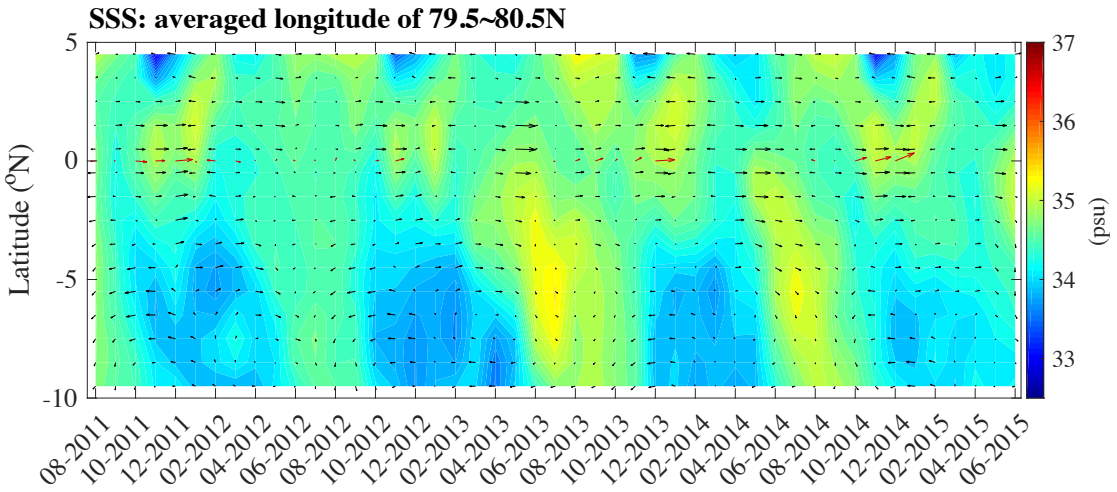

Figure 3.3. Latitude – time plot of Aquarius SSS at the central equatorial Indian Ocean centered at 80°E, OSCAR currents and RAMA 0° 80.5°E mooring currents.

Latitude – Time plot of Aquarius SSS at the central equatorial Indian Ocean centered at 80°E (color shading) and OSCAR near surface current velocities (black vectors). Near surface (10-m depth) monthly current velocities taken from RAMA mooring at 0° 80.5°E are shown as red arrows.

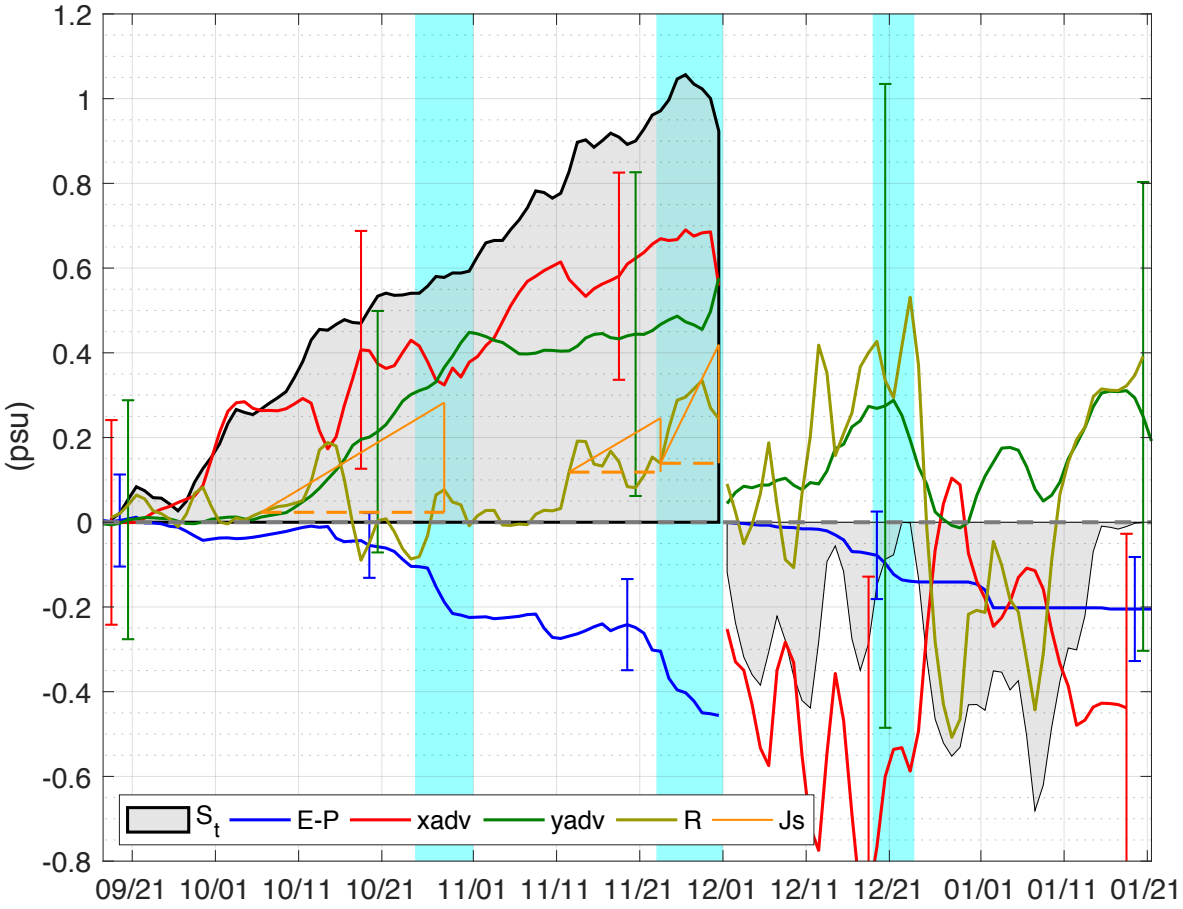

Figure 3.4. The cumulative change of surface mixed layer salinity at two equator moorings during DYNAMO field campaign.

The cumulative change of surface mixed layer salinity (black curves) at two equator moorings at D1 (0°N 79°E) and R1 (0°N 80.5°E) during DYNAMO field campaign. The cumulative change is reset to zero on December 1st, 2018. Blue curve denotes salinity change by the freshwater flux; red and green curves represent the salinity change by zonal and meridional advection; the brown curve represents residual of the salinity budget. Orange triangles show salinity change due to turbulent mixing at the bottom of the mixed layer adopted from Pujiana et al. (2018). Error bars are shown in monthly cumulation of salinity changes under the pessimistic assumption that error

contributions are correlated in the worst possible way. The cyan shading is the three periods of active phases of MJOs in this region according to Chi et al., 2014.

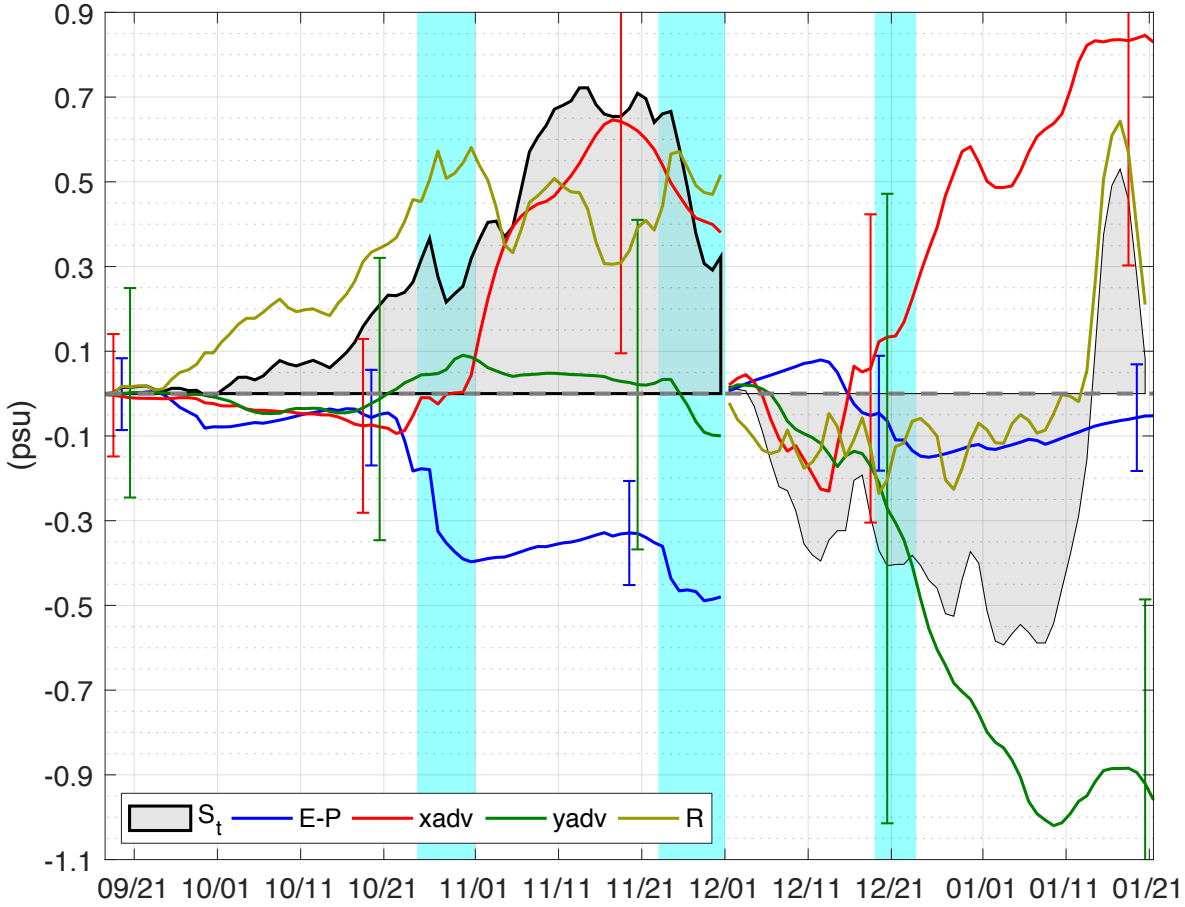

Figure 3.5. Same as Figure 3.4 but for moorings at D2 (1.5S° 79°E) and R2 (1.5S° 80.5°E).

Definitions of colored curves are as described in Figure 3.4.

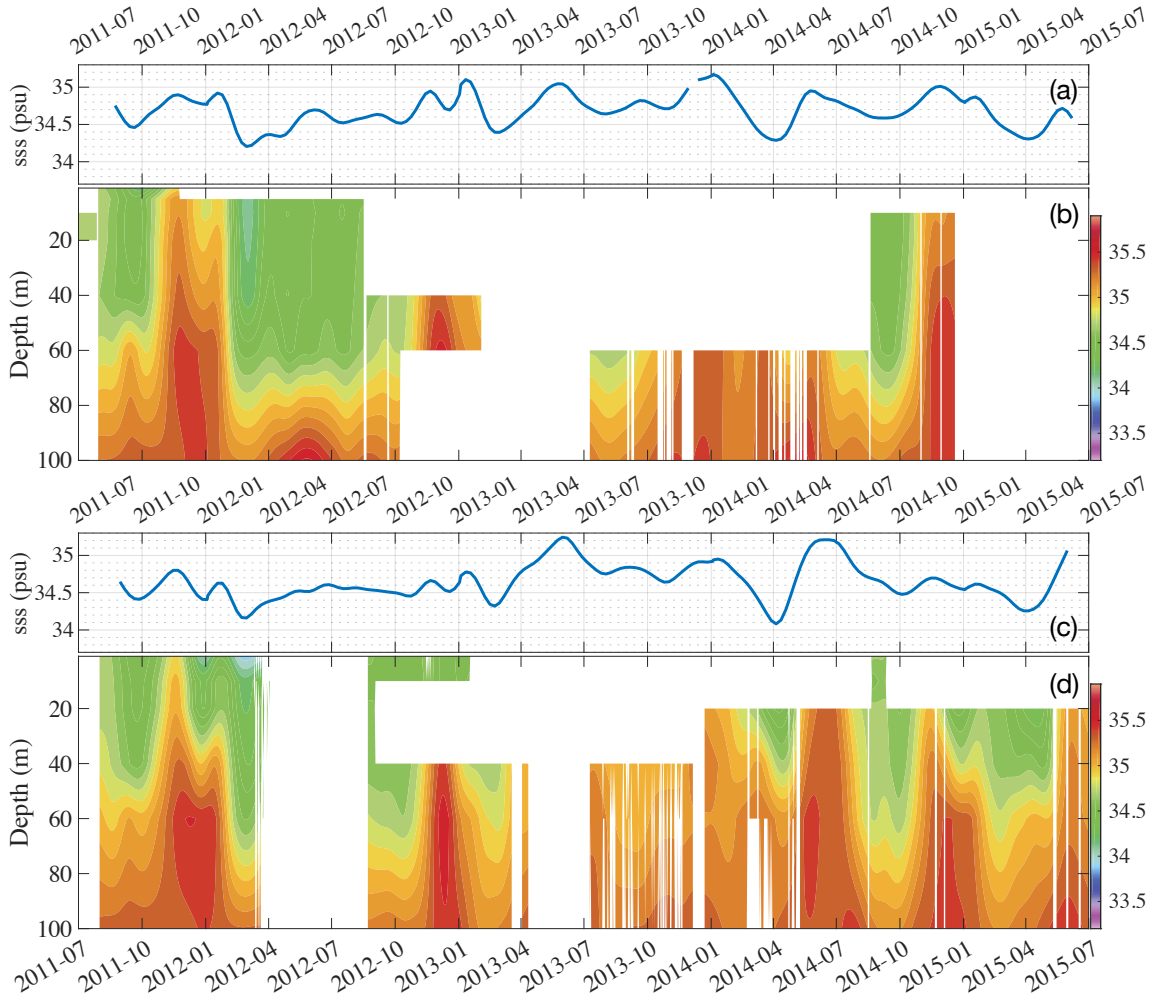

Figure 3.6. Time series of Aquarius SSS and RAMA moorings at 0°N 80.5°E and 1.5°S 80.5°E. Aquarius SSS time series (blue line) at (a) R1 (0°N 80.5°E) and (c) R2 (1.5°S 80.5°E). The upper 100-m salinity measurements (color contours) from RAMA mooring at (b) R1 (0°N 80.5°E) and (d) R2 (1.5°S 80.5°E).

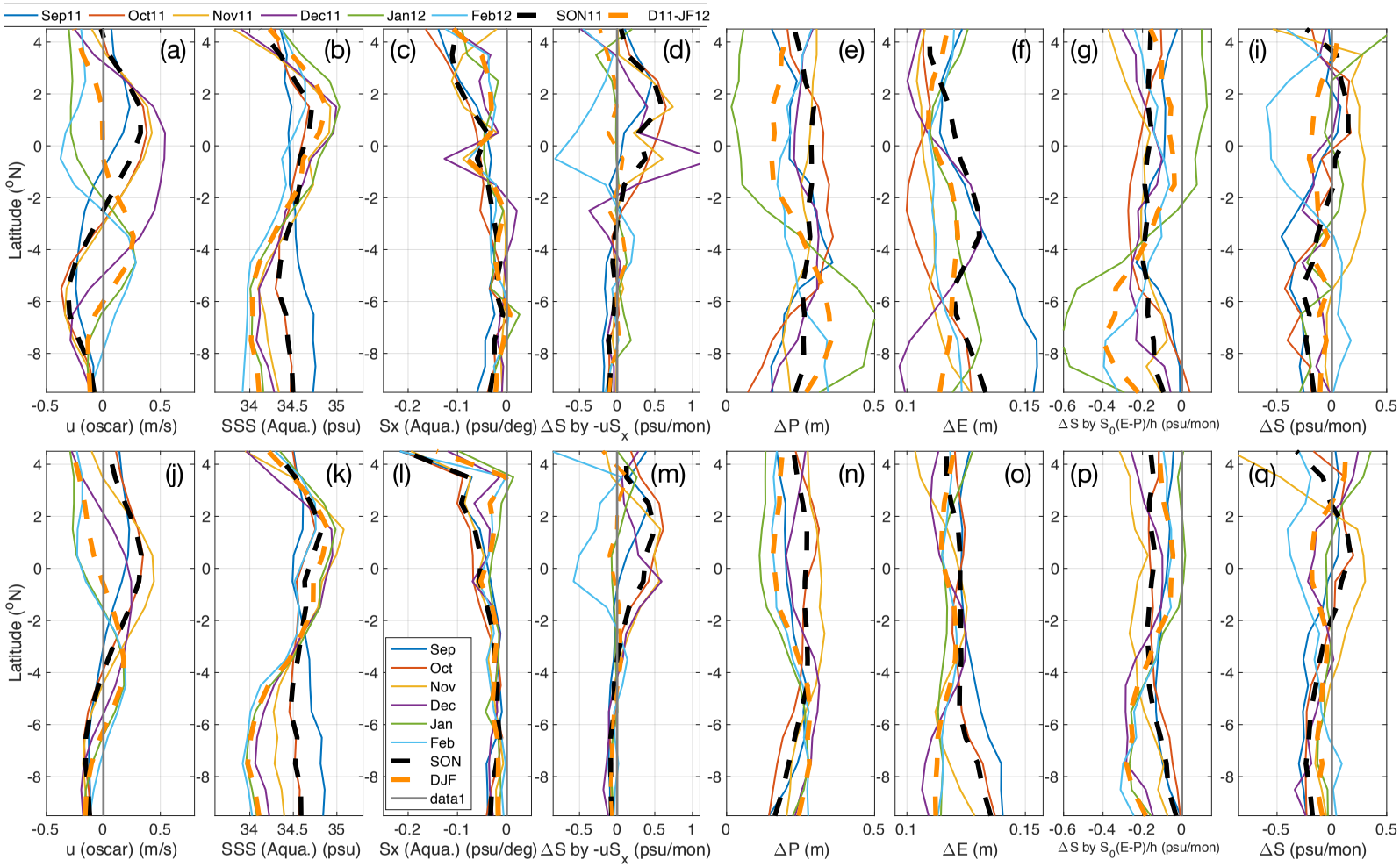
Sep11
Oct11
Nov11
Dec11
Jan12
Feb12
SON11
D11-JF12
(a)
(b)
(c)
(d)
(e)
(f)
(g)
(i)
(j)
(k)
(l)
(m)
(n)
(o)
(p)
(q)
Latitude (°N)
u (oscar) (m/s)
SSS (Aqua.) (psu)
Sx (Aqua.) (psu/deg)
ΔS by -uS$_x$ (psu/mon)
ΔP (m)
ΔE (m)
ΔS by S$_0$(E-P)/h (psu/mon)
ΔS (psu/mon)
Sep
Oct
Nov
Dec
Jan
Feb
SON
DJF
data1

Figure 3.7. Latitudinal structure of zonally averaged (70° – 90°E) satellite and data products derived SSS, SSS gradients, zonal MLS advection, precipitation, evaporation, surface freshwater flux and SSS tendency.

(a, j) OSCAR zonal current, (b, k) Aquarius SSS, (c, l) zonal gradient of Aquarius SSS, (d, m) MLS change due to zonal advection by values in (a, j) and (c, l), (e, n) precipitation, (f, o) evaporation, (g, p) MLS change due to surface freshwater flux, (h, q) Aquarius SSS change. The thick black dash line is the salinity change averaged in boreal fall (September-November) and the orange thick dash line is the salinity changes in boreal winter (December-February). The upper row, a – i, shows measurements from September 2011 to February 2012 and the lower row, j – q, shows measurements from 2011 to 2015.

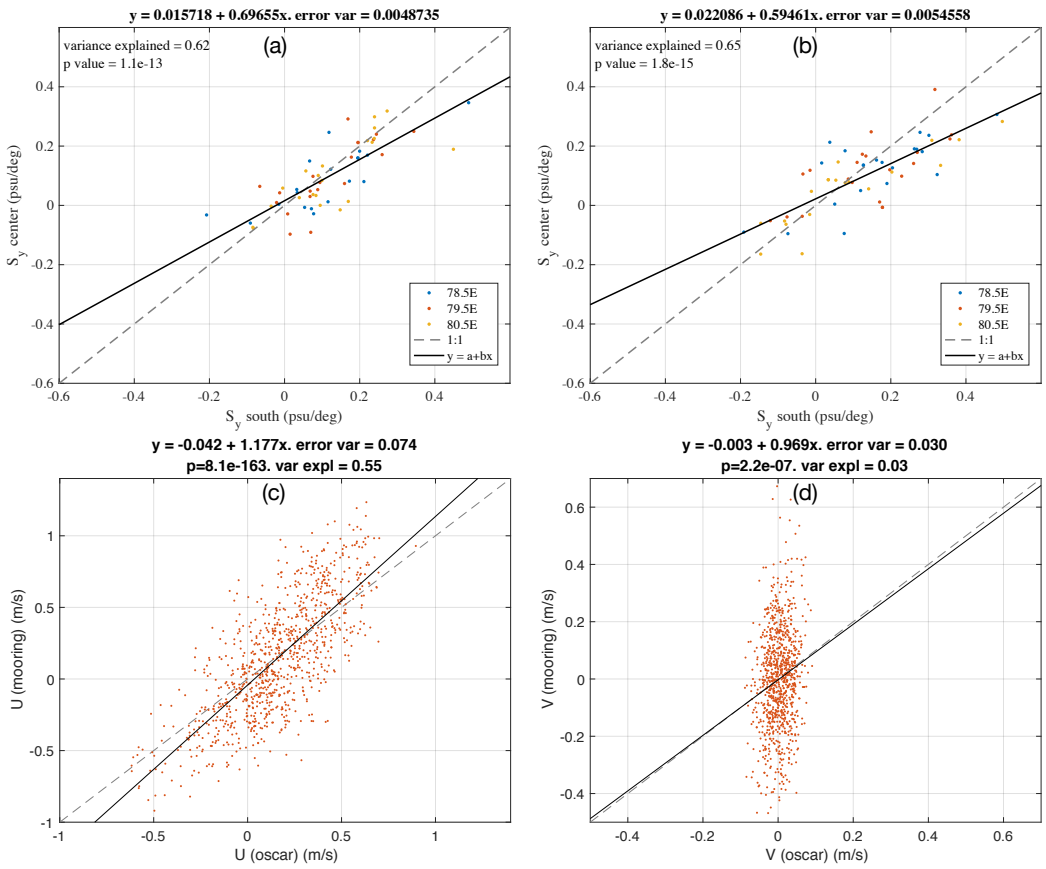

Figure 3.8. The scatter plots of meridional SSS gradients between different locations for the equator and 1.5°S and the scatter plots between OSCAR and RAMA currents.

(a) The scatter plot of the meridional salinity gradient, $\frac{\partial S_a}{\partial y}$, of Aquarius SSS at the equator between the 1° separation to the south of the equator – $\frac{\partial S_a}{\partial y}_{0-1S}$ and the 2° separation centered at the equator – $\frac{\partial S_a}{\partial y}_{1S-1N}$. (b) The scatter plot at the 1.5°S is in a similar fashion but between the 1° separation of $\frac{\partial S_a}{\partial y}$ to the north of 1.5°S and 2° separation of $\frac{\partial S_a}{\partial y}$ centered at 1.5°S. Panels (c) and (d) show scatter plots between OSCAR currents and RAMA mooring currents.

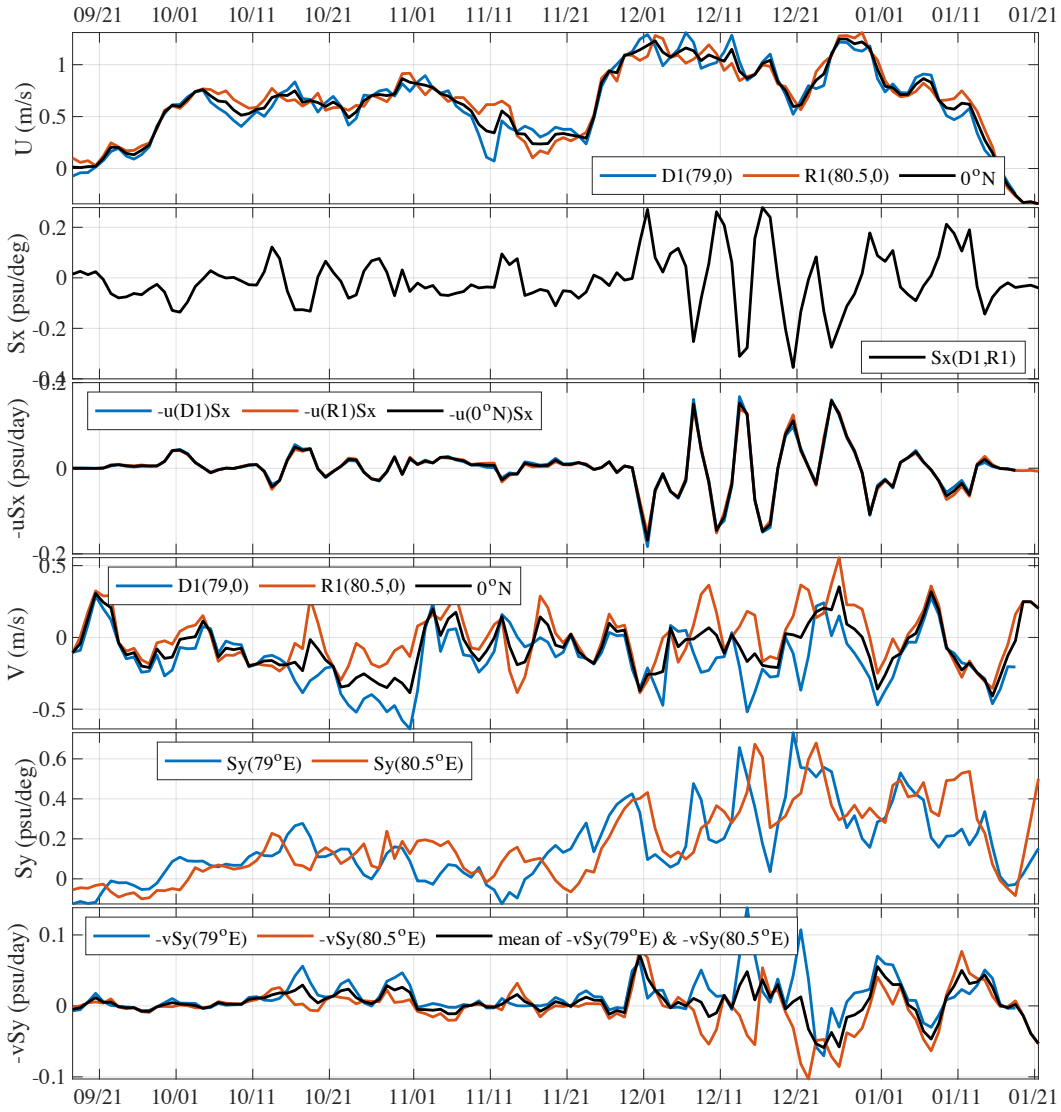

Figure 3.9. The time series of mixed layer mean currents, zonal MLS gradient, zonal advection, meridional MLS gradient and meridional advection at the equator moorings.

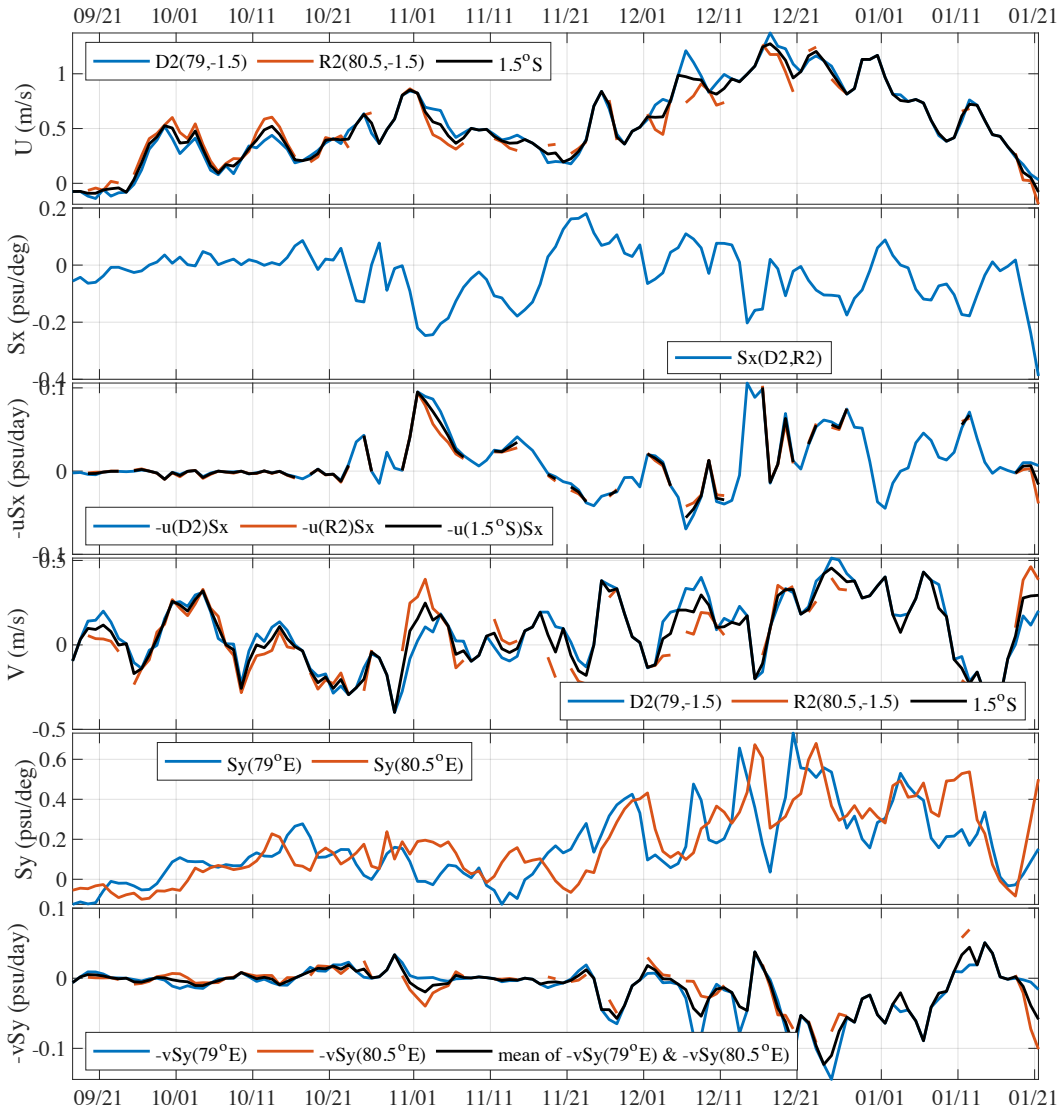

Figure 3.10. Same as Figure 3.9 but for 1.5°S moorings.

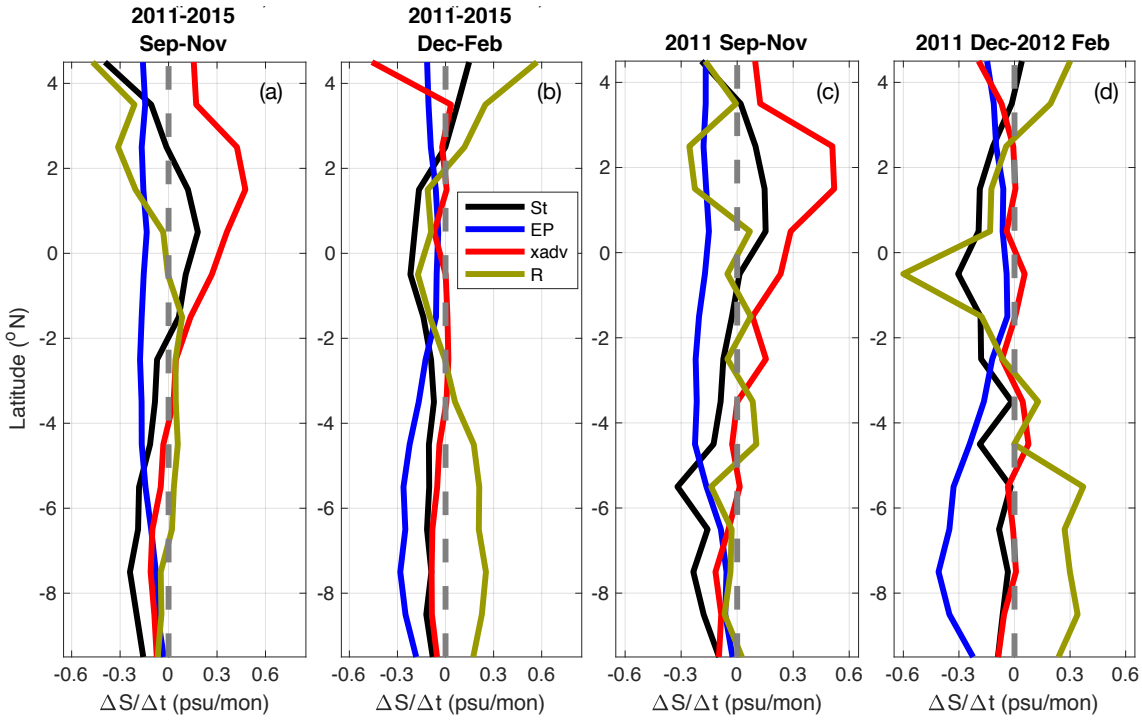

Figure 3.11. The zonal averaged MLS (SSS) budget computing using remote sensing measurements averaged in 70° – 90°E.

(a) in 2011-2015 boreal fall (September-November), (b) in 2011-2015 boreal winter (December-February), (c) in 2011 boreal fall, and (d) in 2011-2012 boreal winter. Meridional advection is excluded because of the large biases in OSCAR meridional currents. The time rate change of MLS, surface freshwater flux (the effect of evaporation minus precipitation), zonal MLS advection and residual are shown in black, blue, red and brown lines respectively.

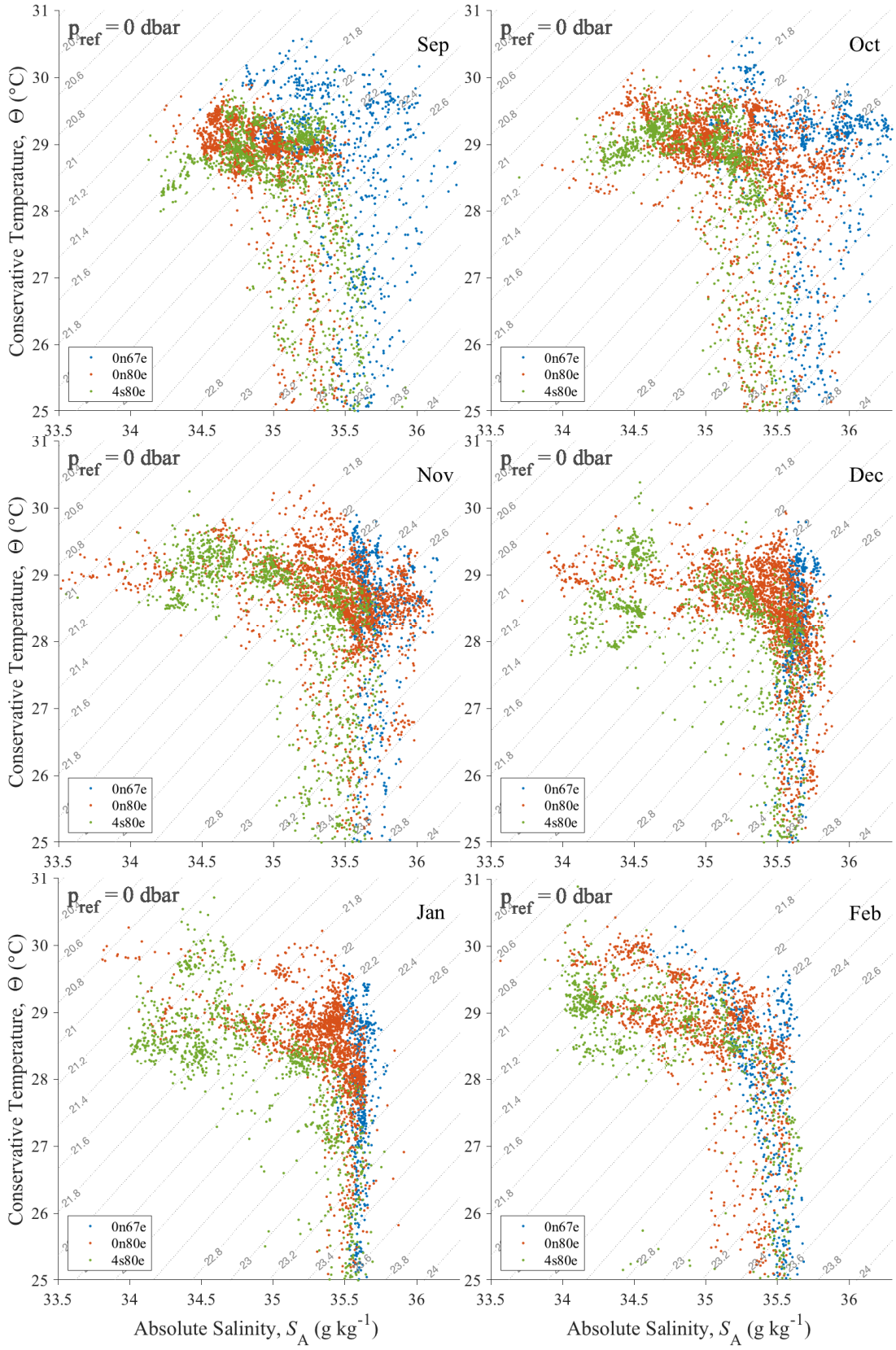
p_ref = 0 dbar
Sep
Oct
Nov
Dec
Jan
Feb
0n67e
0n80e
4s80e
Conservative Temperature, Θ (°C)
Absolute Salinity, S_A (g kg^-1)

Figure 3.12. The temperature-salinity diagrams by three multi-year RAMA moorings at 67°E 0°N, 80.5°E 0°N and 80.5°E 4°S.

67°E 0°N (blue dots), 80.5°E 0°N (red dots) and 80.5°E 4°S (green dots) in boreal fall and winter. Each subplot is all the daily T-S profiles available between 2014~2018 for 67°E 0°N, between 2004~2017 for 80.5°E 0°N and between 2008~2018 for 80.5°E 4°S. Only the upper ocean warmer than 25°C, which is roughly the upper thermocline, is plotted.

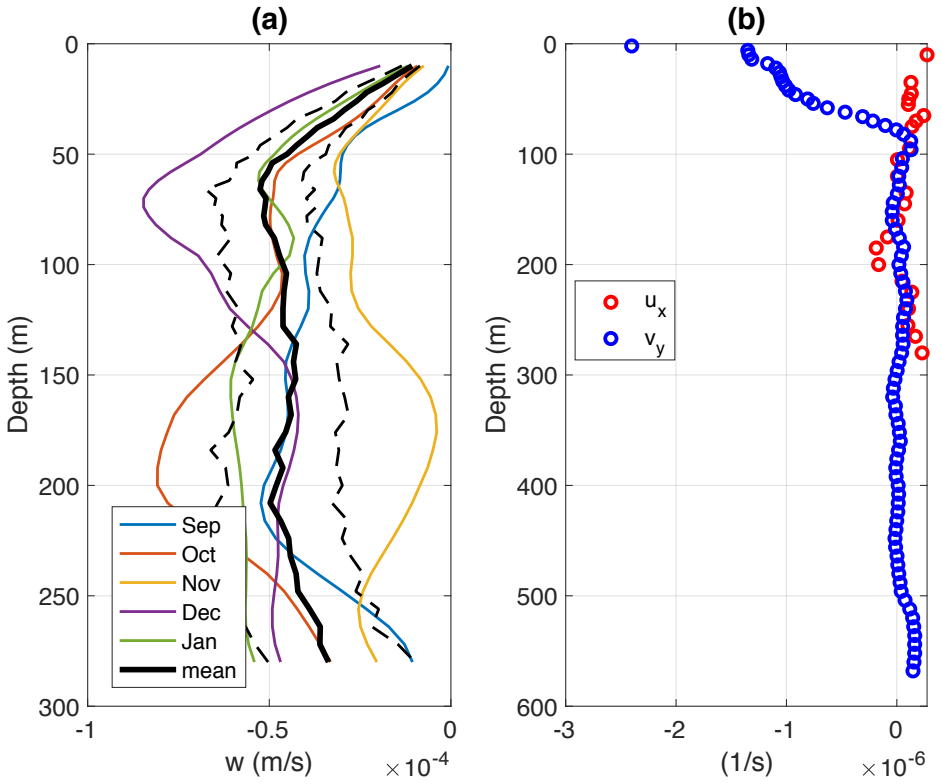

Figure 3.13. The mean vertical velocity and mean horizontal divergence in zonal and meridional directions using three moorings at 79°E 0°N, 80.5°E 0°N and 79°E 1.5°S.

(a) The mean vertical velocity by month between September ~ December 2011 and January 2012 and the mean vertical velocity for the five months in boreal fall and winter 2011-2012. The vertical velocity is estimated by mass convergence using three moorings with multiple current velocity measurements in vertical direction. The zonal convergence, u_x, is computed by D1 (79°E 0°N) and R1 (80.5°E 0°N) moorings. The meridional convergence, v_y, is computed by the D1 (79°E 0°N) and D2 (79°E 1.5°S) moorings. (b) The mean horizontal divergence in zonal (red circles) and meridional (blue circles) directions.

Chapter 4. CONCLUSION

This work evaluates the oceanic surface mixed layer heat and salinity budgets in the central equatorial Indian Ocean, the west flank of the Indo-Pacific warm pool, using two DYNAMO and two RAMA moorings between September 2011 to January 2012, and cross references the turbulent mixing with the results of the microstructure profiler in Pujiana et al. (2018). The oceanic surface MLS budget of the broader central to eastern Indian Ocean is also estimated by the satellite and data products in boreal fall and winter between 2011 to 2015. The ML heat variation is primarily a 1-D problem while the MLS variation is a 3-D problem for intraseasonal to seasonal time scales. These differences are largely derived from the discrepancy between the upper ocean thermal and haline distribution across the horizontal directions. The strong salinity stratification above the bottom of the warm isothermal layer, referred as to the barrier layer, is quasi-permanent in late fall to winter and could exert control on the turbulent heat and salinity fluxes at the base of the surface ML. Therefore, this work also proposes a different measure of the barrier layer strength by "barrier layer potential energy (BLPE)," which depends on the thickness of the barrier layer, the thickness of the ML, and the density stratification across the warm isothermal layer. Whether the cooler water below the warm isothermal layer would be entrained into the surface ML could be determined by the competition between the BLPE and the available kinetic energy (AKE) of the layer of interest.

During the active phases of MJOs, the ML in the central equatorial Indian Ocean is cooled by the net surface heat flux and sometimes by the turbulent heat flux at the bottom of the ML. During the suppressed phases of MJOs, the ML is heated by the net surface heat flux while the turbulent fluxes varies with the stratification of the ML temperature and MLS. While the advective heat flux has relatively minor impact on the intraseasonal ML heat variation, it varies greatly between different MJO events and between the equator and 1.5°S mooring locations. The

seasonal variation of ML temperature and ML heat are comparable to the intraseasonal variation. From boreal fall to winter, the zonal advective heat flux contributes positively to the ML heat budget in the central equatorial Indian Ocean, transporting warmer water from the west. However, the ML is cooled by surface heat flux and turbulent heat flux at the base of the ML associated with multiple MJO events from boreal fall to winter.

On the other hand, the equatorial MLS increases in boreal fall due to the persisting horizontal advection and turbulent mixing, yet the precipitation that often associated with MJOs events freshens the MLS. In boreal winter, the MLS decreases by different mechanisms with meridional direction with just 1.5° apart: the equatorial MLS decreases due to zonal advection and precipitation at the equator, and by meridional advection precipitation at 1.5°S. The multi-year satellite and data products and the long-term RAMA moorings are consistent with the mooring MLS budget results despite it only qualitatively explain the seasonal trend of the equatorial MLS. In boreal fall, the increase of the central to eastern equatorial MLS accompanied by the decrease off the equator creates the boreal fall high equatorial salinity tongue. In boreal winter, the maximal MLS decrease at the equatorial band resembles the retreat of the high equatorial salinity tongue, of which the satellite SSS and data product currents fail to capture the primary mechanisms.

The horizontal advection acts to transport spicier, warmer and saltier, water mass from the west. However, the ML becomes cooler and saltier and therefore denser from boreal fall to winter since the ML heat variation is cooled and dominant by 1-D processes, namely the surface heat flux and turbulent heat flux at the base of the ML. The advective and turbulent fluxes at the base of the surface ML vary greatly in the central equatorial Indian Ocean between different phases of MJOs and seasons, suggesting the important and complicated roles of oceanic processes in the surface ML heat and salinity budgets. Therefore, to better simulate and predict

the ML heat fluxes, models should estimate the oceanic barrier layer potential energy, background shear, stratification, and surface forcing accurately. To better simulate and predict the MLS changes, models should properly predict the strength and timing of the equatorial currents as well as the salinity gradients at least on one-degree resolution every few days.

BIBLIOGRAPHY

Abram, N. J., Gagan, M. K., Cole, J. E., Hantoro, W. S., & Mudelsee, M. (2008), Recent intensification of tropical climate variability in the Indian Ocean. Nature Geoscience, 1(12), 849-853. DOI: 10.1038/ngeo357.

Cherchi, A., S. Gualdi, S. Behera, J.J. Luo, S. Masson, T. Yamagata, and A. Navarra (2007), The Influence of Tropical Indian Ocean SST on the Indian Summer Monsoon. J. Climate, 20, 3083–3105, https://doi.org/10.1175/JCLI4161.1.

Chi, N.-H., R.-C. Lien, E. A. D'Asaro, and B. B. Ma (2014), The surface mixed layer heat budget from mooring observations in the central Indian Ocean during Madden–Julian Oscillation events, J. Geophys. Res. Oceans, 119, 4638–4652, doi: 10.1002/2014JC010192.

Cronin, M. F., and M. J. McPhaden (1997), The upper ocean heat balance in the western equatorial Pacific warm pool during September–December 1992, J. Geophys. Res., 102(C4), 8533–8553, doi: 10.1029/97JC00020.

Cronin, M. F., and M. J. McPhaden (1998), Upper ocean salinity balance in the western equatorial Pacific, J. Geophys. Res., 103(C12), 27567–27587, doi: 10.1029/98JC02605.

Cronin, M. F., and M. J. McPhaden (2002), Barrier layer formation during westerly wind bursts, J. Geophys. Res., 107(C12), 8020, doi: 10.1029/2001JC001171.

de Boyer Montégut, C., J. Mignot, G. Madec, A. S. Fischer, A. Lazar, and D. Iudicone (2004), Mixed layer depth over the global ocean: An examination of profile data and a profile-based climatology, J. Geophys. Res., 109, C12003, doi:10.1029/2004JC002378.

de Boyer Montégut, C., J. Mignot, A. Lazar, and S. Cravatte (2007), Control of salinity on the mixed layer depth in the world ocean: 1. General description, J. Geophys. Res., 112,

C06011, doi: 10.1029/2006JC003953.

Dickson, Robert R., Jens Meincke, Svend Aage Malmberg, and Arthur J. Lee (1988), The "great salinity anomaly" in the Northern North Atlantic 1968–1982, Progress in Oceanography, Vol: 20, Issue: 2, 103-151, doi: 10.1016/0079-6611(88)90049-3.

Drushka, K., J. Sprintall, S.T. Gille, and S. Wijffels (2012), In Situ Observations of Madden–Julian Oscillation Mixed Layer Dynamics in the Indian and Western Pacific Oceans. J. Climate, 25, 2306–2328, https://doi.org/10.1175/JCLI-D-11-00203.1.

Du, Y. and Y. Zhang (2015), Satellite and Argo Observed Surface Salinity Variations in the Tropical Indian Ocean and Their Association with the Indian Ocean Dipole Mode.J. Climate, 28, 695–713, https://doi.org/10.1175/JCLI-D-14-00435.1.

Duan Y., Liu L., Han G., Liu H., Yu W., Yang G., Wang H., Wang H., Liu Y., Zahid, Waheed H. (2016), Anomalous behaviors of Wyrtki Jets in the equatorial Indian Ocean during 2013. Sci Rep. 2016 Jul;6 29688. doi:10.1038/srep29688.

Edson, J.B., V. Jampana, R.A. Weller, S.P. Bigorre, A.J. Plueddemann, C.W. Fairall, S.D. Miller, L. Mahrt, D. Vickers, and H. Hersbach (2013), On the Exchange of Momentum over the Open Ocean. J. Phys. Oceanogr., 43, 1589–1610, https://doi.org/10.1175/JPO-D-12-0173.1.

Fairall, C. W., E. F. Bradley, J. S. Godfrey, G. A. Wick, J. B. Edson, and G. S. Young (1996), Cool-skin and warm-layer effects on sea surface temperature, J. Geophys. Res., 101(C1), 1295–1308, doi: 10.1029/95JC03190.

Fairall, C.W., P.O. Persson, E.F. Bradley, R.E. Payne, and S.P. Anderson (1998), A New Look at Calibration and Use of Eppley Precision Infrared Radiometers. Part I: Theory and Application. J. Atmos. Oceanic Technol., 15, 1229–1242, https://doi.org/10.1175/1520-0426(1998)015<1229:ANLACA>2.0.CO;2.

Farrar, J. T. (2007), Air-sea Interaction at Contrasting Sites in the Eastern Tropical Pacific: Mesoscale Variability and Atmospheric Convection at 10°N, Ph.D. thesis, Massachusetts Institute of Technology and the Woods Hole Oceanographic Institution. Cambridge, Massachusetts, 166 pp.

Ferrari, R., and D. L. Rudnick (2000), Thermohaline variability in the upper ocean, J. Geophys. Res., 105(C7), 16857–16883, doi: 10.1029/2000JC900057.

Flatau, M., P.J. Flatau, P. Phoebus, and P.P. Niiler (1997), The Feedback between Equatorial Convection and Local Radiative and Evaporative Processes: The Implications for Intraseasonal Oscillations. J. Atmos. Sci., 54, 2373–2386, https://doi.org/10.1175/1520-0469(1997)054<2373:TFBECA>2.0.CO;2.

Foltz, G. R., S. A. Grodsky, J. A. Carton, and M. J. McPhaden (2004), Seasonal salt budget of the northwestern tropical Atlantic Ocean along 38°W, J. Geophys. Res., 109, C03052, doi:10.1029/2003JC002111.

Foltz, G.R., J. Vialard, B. Praveen Kumar, and M.J. McPhaden (2010), Seasonal Mixed Layer Heat Balance of the Southwestern Tropical Indian Ocean. J. Climate, 23, 947–965, https://doi.org/10.1175/2009JCLI3268.1.

Gill, A. E., P. P. Niller (1973), The theory of the seasonal variability in the ocean, Deep Sea Research and Oceanographic Abstracts, 20, 2, 141-177, ISSN 0011-7471, https://doi.org/10.1016/0011-7471(73)90049-1.

Godfrey, J. S., and E. J. Lindstrom (1989), The heat budget of the equatorial western Pacific surface mixed layer, J. Geophys. Res., 94(C6), 8007–8017, doi: 10.1029/JC094iC06p08007.

Gordon, A.L., E.L. Shroyer, A. Mahadevan, D. Sengupta, and M. Freilich (2016), Bay of Bengal: 2013 northeast monsoon upper-ocean circulation. Oceanography 29(2):82–

91, https://doi.org/10.5670/oceanog.2016.41.

Graham, N., and T. Barnett (1987), Sea surface temperature, surface wind divergence, and convection over tropical oceans, Science, 238(4827), 657-659, doi: 10.1126/science.238.4827.657.

Guan, B., T. Lee, D. J. Halkides, and D. E. Waliser (2014), Aquarius surface salinity and the Madden-Julian Oscillation: The role of salinity in surface layer density and potential energy, Geophys. Res. Lett., 41, 2858–2869, doi: 10.1002/2014GL059704.

Han, W., J.P. McCreary, D.L. Anderson, and A.J. Mariano (1999), Dynamics of the Eastern Surface Jets in the Equatorial Indian Ocean. J. Phys. Oceanogr., 29, 2191–2209,https://doi.org/10.1175/1520-0485(1999)029<2191:DOTESJ>2.0.CO;2.

Holte, J. and L. Talley (2009), A New Algorithm for Finding Mixed Layer Depths with Applications to Argo Data and Subantarctic Mode Water Formation. J. Atmos. Oceanic Technol., 26, 1920–1939, https://doi.org/10.1175/2009JTECHO543.1.

Horii, T., Y. Masumoto, I. Ueki, S. P. Kumar, and K. Mizuno (2011), Intraseasonal vertical velocity variation caused by the equatorial wave in the central equatorial Indian Ocean, J. Geophys. Res., 116, C09005, doi: 10.1029/2011JC007081.

Huffman, G.J., D.T. Bolvin, E.J. Nelkin, D.B. Wolff, R.F. Adler, G. Gu, Y. Hong, K.P. Bowman, and E.F. Stocker9 (2007), The TRMM Multisatellite Precipitation Analysis (TMPA): Quasi-Global, Multiyear, Combined-Sensor Precipitation Estimates at Fine Scales. J. Hydrometeor., 8, 38–55, https://doi.org/10.1175/JHM560.1.

Iskandar, I., Y. Masumoto, and K. Mizuno (2009), Subsurface equatorial zonal current in the eastern Indian Ocean, J. Geophys. Res., 114, C06005, doi: 10.1029/2008JC005188.

Iskandar, I., and M. J. McPhaden (2011), Dynamics of wind-forced intraseasonal zonal current variations in the equatorial Indian Ocean, J. Geophys. Res., 116, C06019,

doi:10.1029/2010JC006864.

Jensen, T.G., H.W. Wijesekera, E.S. Nyadjro, P.G. Thoppil, J.F. Shriver, K.K. Sandeep, and V. Pant (2016), Modeling salinity exchanges between the equatorial Indian Ocean and the Bay of Bengal. Oceanography 29(2):92–101, https://doi.org/10.5670/oceanog.2016.42.

Joseph, S., Ravichandran, M., Kumar, B.P. et al. Clim Dyn (2017), 49: 575. https://doi.org/10.1007/s00382-016-3359-1.

Kao, H.-Y., G. Lagerloef, T. Lee, O. Melnichenko, P. Hacker (2018), Aquarius Salinity Validation Analysis (Data Version 5.0). AQ-014-PS-0016, http://dx.doi.org/10.5067/DOCUM-AQR02.

Köhler, J., Serra, N., Bryan, F. O., Johnson, B. K., & Stammer, D. (2018), Mechanisms of mixed-layer salinity seasonal variability in the Indian Ocean. Journal of Geophysical Research: Oceans, 123, 466–496. https://doi.org/10.1002/2017JC013640.

Kumar, S. P., and T. G. Prasad (1999), Formation and spreading of Arabian Sea high-salinity water mass, J. Geophys. Res., 104(C1), 1455–1464, doi: 10.1029/1998JC900022.

Li, Y., F. Wang (2015), Thermocline spiciness variations in the tropical Indian Ocean observed during 2003-2014, Deep Sea Res. Part 1: Oceanog. Res. Papers, 97, 52-66. https://doi.org/10.1016/j.dsr.2014.12.004.

Liebmann, B., H. H. Hendon, and J. D. Glick (1994), The relationship between tropical cyclones of the western Pacific and Indian Oceans and the Madden–Julian oscillation, J. Meteor. Soc. Japan, 72, 401-411, https://doi.org/10.2151/jmsj1965.72.3_401.

Lombardo, C. P., and M. C. Gregg (1989), Similarity scaling of viscous and thermal dissipation in a convecting surface boundary layer, J. Geophys. Res., 94(C5), 6273–6284, doi:10.1029/JC094iC05p06273.

Lukas, R., and E. Lindstrom (1991), The mixed layer of the western equatorial Pacific Ocean, J.

Geophys. Res., 96(S01), 3343–3357, https://doi.org/10.1029/90JC01951.

Madden, R.A. and P.R. Julian (1971), Detection of a 40–50 Day Oscillation in the Zonal Wind in the Tropical Pacific. J. Atmos. Sci., 28, 702–708,https://doi.org/10.1175/1520-0469(1971)028<0702:DOADOI>2.0.CO;2.

Madden, R.A. and P.R. Julian (1972), Description of Global-Scale Circulation Cells in the Tropics with a 40–50 Day Period. J. Atmos. Sci., 29, 1109–1123,https://doi.org/10.1175/1520-0469(1972)029<1109:DOGSCC>2.0.CO;2.

Madden, R.A. and P.R. Julian (1994), Observations of the 40–50-Day Tropical Oscillation—A Review. Mon. Wea. Rev., 122, 814–837, https://doi.org/10.1175/1520-0493(1994)122<0814:OOTDTO>2.0.CO;2.

Masson, S., C. Menkes, P. Delecluse, and J.-P. Boulanger (2003), Impacts of salinity on the eastern Indian Ocean during the termination of the fall Wyrtki Jet, J. Geophys. Res., 108, 3067, doi: 10.1029/2001JC000833, C3.

Matthews, A. J., Singhruck, P., and Heywood, K. J. (2010), Ocean temperature and salinity components of the Madden-Julian oscillation observed by Argo floats. Climate Dynamics, 35 (7-8). pp. 1149-1168. ISSN 0930-7575.

McPhaden, M.J. (2002), Mixed Layer Temperature Balance on Intraseasonal Timescales in the Equatorial Pacific Ocean. J. Climate, 15, 2632–2647, https://doi.org/10.1175/1520-0442(2002)015<2632:MLTBOI>2.0.CO;2.

McPhaden, M.J., G. Meyers, K. Ando, Y. Masumoto, V.S. Murty, M. Ravichandran, F. Syamsudin, J. Vialard, L. Yu, and W. Yu (2009), RAMA: The Research Moored Array for African–Asian–Australian Monsoon Analysis and Prediction*. Bull. Amer. Meteor. Soc., 90, 459–480, https://doi.org/10.1175/2008BAMS2608.1.

McPhaden, M. J., and G. R. Foltz (2013), Intraseasonal variations in the surface layer heat

balance of the central equatorial Indian Ocean: The importance of zonal advection and vertical mixing, Geophys. Res. Lett., 40, 2737–2741, doi: 10.1002/grl.50536.

McPhaden, M. J., Y. Wang, and M. Ravichandran (2015), Volume transports of the Wyrtki jets and their relationship to the Indian Ocean Dipole, J. Geophys. Res. Oceans, 120, 5302–5317, doi: 10.1002/2015JC010901.

Mignot, J., C. de Boyer Montégut, A. Lazar, and S. Cravatte (2007), Control of salinity on the mixed layer depth in the world ocean: 2. Tropical areas, J. Geophys. Res., 112, C10010, doi:10.1029/2006JC003954.

Moisan, J.R. and P.P. Niiler (1998), The Seasonal Heat Budget of the North Pacific: Net Heat Flux and Heat Storage Rates (1950–1990). J. Phys. Oceanogr., 28, 401–421,https://doi.org/10.1175/1520-0485(1998)028<0401:TSHBOT>2.0.CO;2.

Moum, J.N., S.P. de Szoeke, W.D. Smyth, J.B. Edson, H.L. DeWitt, A.J. Moulin, E.J. Thompson, C.J. Zappa, S.A. Rutledge, R.H. Johnson, and C.W. Fairall (2014), Air–Sea Interactions from Westerly Wind Bursts During the November 2011 MJO in the Indian Ocean. Bull. Amer. Meteor. Soc., 95, 1185–1199, https://doi.org/10.1175/BAMS-D-12-00225.1.

Nagura, M., and M. J. McPhaden (2008), The dynamics of zonal current variations in the central equatorial Indian Ocean, Geophys. Res. Lett., 35, L23603, doi:10.1029/2008GL035961.

Nyadjro, E. S., and B. Subrahmanyam (2016), Spatial and temporal variability of central Indian Ocean salinity fronts observed by SMOS, Remote Sensing of Environment, 180, 146-153, ISSN 0034-4257, https://doi.org/10.1016/j.rse.2016.02.049.

Ponte, R. M., and N. T. Vinogradova (2016), An assessment of basic processes controlling mean surface salinity over the global ocean, Geophys. Res. Lett., 43, 7052–7058, doi:10.1002/2016GL069857.

Price, J. F., T. B. Sanford, and G. Z. Forristall (1994), Forced stage response to a moving hurricane, J. Phys. Oceanogr., 24, 233–260, https://doi.org/10.1175/1520-0485(1994)024<0233:FSRTAM>2.0.CO;2

Pujiana, K., J. N. Moum, and W. D. Smyth (2018), The Role of Turbulence in Redistributing Upper-Ocean Heat, Freshwater, and Momentum in Response to the MJO in the Equatorial Indian Ocean, J. Phys. Oceanogr., 48, 197–220, https://doi.org/10.1175/JPO-D-17-0146.1.

Raymond, D. J., and Fuchs, Ž. (2018), The Madden-Julian oscillation and the Indo-Pacific warm pool. Journal of Advances in Modeling Earth Systems, 10, 951–960. https://doi.org/10.1002/2017MS001258.

Roundy, P.E. and G.N. Kiladis (2006), Observed Relationships between Oceanic Kelvin Waves and Atmospheric Forcing. J. Climate, **19**, 5253–5272, https://doi.org/10.1175/JCLI3893.1.

Roxy, M.K., K. Ritika, P. Terray, and S. Masson (2014), The Curious Case of Indian Ocean Warming. J. Climate, 27, 8501–8509, https://doi.org/10.1175/JCLI-D-14-00471.1

Saji, N. H., B. N. Goswami, P. N. Vinayachandran, and T. Yamagata (1999), A dipole mode in the tropical Indian Ocean, Nature, 201, 360-363, doi:10.1038/43854.

Sato, N., K. Yoneyama, M. Katsumata, R. Shirooka, and Y. N. Takayabu (2007), An ITCZ-like convergence zone over the Indian Ocean in boreal late autumn, Geophys. Res. Lett., 34, L10811, doi: 10.1029/2006GL028341.

Schneider, N. (2000), A decadal spiciness mode in the tropics. Geophys. Res. Lett., 27 257-260.

Schott, F. and McCreary, J. P. (2001), The Monsoon Circulation of the Indian Ocean. Progress in Oceanography, 51, 1-123. http://dx.doi.org/10.1016/S0079-6611(01)00083-0.

Schott, F. A., S.-P. Xie, and J. P. McCreary Jr. (2009), Indian Ocean circulation and climate

variability, Rev. Geophys., 47, RG1002, doi: 10.1029/2007RG000245.

Sengupta, D., R. Senan, B.N. Goswami, and J. Vialard (2007), Intraseasonal Variability of Equatorial Indian Ocean Zonal Currents. J. Climate, 20, 3036–3055, https://doi.org/10.1175/JCLI4166.1.

Sprintall, J., and M. Tomczak (1992), Evidence of the barrier layer in the surface layer of the tropics, J. Geophys. Res., 97(C5), 7305–7316, doi: 10.1029/92JC00407.

Tian, B., D.E. Waliser, E.J. Fetzer, B.H. Lambrigtsen, Y.L. Yung, and B. Wang (2006), Vertical Moist Thermodynamic Structure and Spatial–Temporal Evolution of the MJO in AIRS Observations. J. Atmos. Sci., 63, 2462–2485, https://doi.org/10.1175/JAS3782.1.

Thorpe, S. A. (2005), The Turbulent Ocean. New York, Cambridge University Press, 439 pp, https://doi.org/10.1017/CBO9780511819933.

Turner, J. S. (1973), Buoyancy Effects in Fluids. 1st ed. Cambridge University Press, https://doi.org/10.1017/CBO9780511608827.

Vinogradova, N. T., and R. M. Ponte (2013), Clarifying the link between surface salinity and freshwater fluxes on monthly to interannual time scales, J. Geophys. Res. Oceans, 118, 3190–3201, doi: 10.1002/jgrc.20200.

Webber, B. G., Matthews, A. J. and Heywood, K. J. (2010), A dynamical ocean feedback mechanism for the Madden–Julian Oscillation. Q.J.R. Meteorol. Soc., 136: 740-754. doi:10.1002/qj.604.

Webber, B. G. M., A. J. Matthews, K. J. Heywood, J. Kaiser, and S. Schmidtko (2014), Seaglider observations of equatorial Indian Ocean Rossby waves associated with the Madden-Julian Oscillation, J. Geophys. Res. Oceans, 119, 3714–3731, doi:10.1002/2013JC009657.

Wheeler, M.C. and H.H. Hendon (2004), An All-Season Real-Time Multivariate MJO Index:

Development of an Index for Monitoring and Prediction. Mon. Wea. Rev., 132,1917–1932, https://doi.org/10.1175/1520-0493(2004)132<1917:AARMMI>2.0.CO;2.

Wijesekera, H. W., and M. C. Gregg (1996), Surface layer response to weak winds, westerly bursts, and rain squalls in the western Pacific warm pool, J. Geophys. Res., 101(C1), 977–997, doi: 10.1029/95JC02553.

Wijesekera, H. W., T. G. Jensen, E. Jarosz, W. J. Teague, E. J. Metzger, D. W. Wang, S. U. P. Jinadasa, K. Arulananthan, L. R. Centurioni, and H. J. S. Fernando (2015), Southern Bay of Bengal currents and salinity intrusions during the northeast monsoon, J. Geophys. Res. Oceans, 120, 6897–6913, doi: 10.1002/2015JC010744.

Wyrtki K. (1973), An equatorial jet in the Indian Ocean, Science, 181 (4096), 262-264, doi: 10.1126/science.181.4096.262.

Yoneyama, K., Zhang, C., and Long, C. N. (2013), Tracking pulses of the Madden-Julian oscillation. Bulletin of the American Meteorological Society, 94(12), 1871-1891. DOI: 10.1175/BAMS-D-12-00157.1.

Young, H. D. (1962), Statistical Treatment of Experimental Data. New York, McGraw-Hill, 172 pp, https://doi.org/10.1002/bimj.19650070123.

Yu, L. (2011), A global relationship between the ocean water cycle and near-surface salinity, J. Geophys. Res., 116, C10025, doi:10.1029/2010JC006937.

Zhang, C. (2001), Double ITCZs, J. Geophys. Res., 106(D11), 11785–11792, doi:10.1029/2001JD900046.

Zhang, C. (2005), Madden-Julian Oscillation, Rev. Geophys., 43, RG2003, doi:10.1029/2004RG000158.

Zhang, C. (2013), Madden–Julian Oscillation: Bridging Weather and Climate. Bull. Amer. Meteor. Soc., 94, 1849–1870, https://doi.org/10.1175/BAMS-D-12-00026.1.

Zhang, Y., Y. Du, and M. Feng 2018: Multiple Time Scale Variability of the Sea Surface Salinity Dipole Mode in the Tropical Indian Ocean. J. Climate, 31, 283–296,https://doi.org/10.1175/JCLI-D-17-0271.1

APPENDIX

A. Net surface heat flux

The net surface heat flux is the sum of latent heat flux, sensible heat flux, sensible heat flux due to rain, net shortwave and net longwave radiation, and penetrative shortwave radiation through the base of the surface mixed layer:

$$Q_0 = Q_{LH} + Q_{SH} + Q_{rain} + Q_{SW} + Q_{LW} + Q_{pen} \quad (8)$$

Latent heat, sensible heat, and sensible heat due to rain are calculated from the mooring data using the Coupled Ocean–Atmosphere Response Experiment (COARE) version 3.5 bulk flux algorithm with cool skin depression and warm layer effects [Fairall et al., 1996]. Net penetrative shortwave heat flux is computed from the measured downward shortwave radiation and the in situ optical profiles obtained from the R/V Revelle ship station 180 km away (provided by Carter Ohlmann and Jim Moum). Because the equator buoy was vandalized on 20 November 2011, the net surface heat flux measured at the 1.5°S moorings is used as a surrogate for the equator buoy after that date with a minor offset.

B. Error Estimates

The error estimate of the heat fluxes is computed based on the theory of propagation of errors under conservative assumptions [Young, 1962; Farrar, 2007]. There are two types of measurement errors: random and systematic instrumental errors that are both summarized in Table 2.3. The error in this study is calculated as the standard deviation of the errors (section 2.5.2).

The standard meteorological sensors on the R/V Revelle were augmented with a suite of specially equipped meteorological sensors to measure the atmospheric turbulent fluxes directly [Moum et al., 2013]. The shipboard meteorological measurements are higher quality than those from the moorings. A comparison of the measurements from the equator mooring with those

from the Revelle 180 km away at the equator, 80°E shows systematic instrument errors on the mooring (Table 2.3). The dome temperature of the pyrgeometer on the equator mooring was not recorded and therefore the temperature effects were not corrected [Fairall et al., 1998]. The downward longwave radiation at the equator mooring is biased high (10.2 W m^{-2} on average) in the daytime. The difference between the downward longwave radiation on the mooring and that on the ship is correlated linearly with the downward shortwave radiation. Therefore, the measured downward longwave radiation on the mooring is adjusted by the downward shortwave radiation to match the shipboard measurement. The measured air temperature and relative humidity (RH) on the equator mooring are biased high (1.35°C, 6.58% on average) in the daytime. We are not able to adjust them. On average, the mooring absolute humidity is 0.35 g/kg less and latent heat flux is 5 W m^{-2} (4%) greater than those measured aboard the R/V Revelle. The sensible heat flux depends on air temperature but it is relatively small compared with other components.

Due to the failure of the 300-kHz ADCP on 9 November 2011, the advective heat flux at 1.5°S is computed using linearly interpolated velocity. To investigate the error introduced by the linear interpolation scheme, we compare the advective heat flux before 9 November using the observed velocity and the linearly interpolated velocity between 22 and 54 m depth. The largest difference in daily advective heat flux and daily surface mixed layer velocity is less than 10 W m^{-2} and 0.15 m s^{-1} in magnitude. The difference in advective heat flux is fortunately small compared to other terms in (7) so the overall results should be reasonable.

C. Sensitivity of MLD Definition to the Surface Mixed Layer Heat Budget

The heat budget components in (7) vary with the definition of MLD. To investigate the sensitivity, we compute and compare the surface mixed layer heat budget using different MLD definitions, with five different density increments ($\Delta\sigma_t = 0.2, 0.15, 0.1, 0.05, 0.01\ kg\ m^{-3}$) from

that at 5 m depth. Heat fluxes computed using the density criterion of $\sigma_t = 0.1\ kg\ m^{-3}$ (section 2.2) are called the "reference." Note that the MLD is a function of time. It is shallower during calm phases and deeper during active phases of MJO events (Figure 2.4).

The MLD defined by the density criterion of $\Delta\sigma_t = 0.05, and\ 0.01\ kg\ m^{-3}$ is shallower than the reference MLD with a strong diurnal cycle, especially for $\Delta\sigma_t = 0.01\ kg\ m^{-3}$. Heat fluxes computed using $\Delta\sigma_t = 0.01\ kg\ m^{-3}$ exhibit strong diurnal variation and therefore do not clearly reveal the intraseasonal variation that is the primary focus of the present analysis. The average of advective heat flux and net surface heat flux for calm and active phases computed using $\Delta\sigma_t = 0.2, 0.15, \text{and } 0.05\ \text{kg m}^{-3}$ do not show significant differences from the reference, with maximum differences of 10 W m^{-2}. The average of surface mixed layer heat storage rate and residual flux for calm and active phases computed using different MLD definitions show moderate differences from the reference with a maximum difference of 40 W m^{-2}.

The MLD defined with a larger density increment criterion yields a deeper mixed layer, as expected. The residual flux computed using a deeper MLD yields greater cooling during MJO active phases and greater variations in magnitude during MJO calm phases. With the definition of deeper MLD, the relative contribution of the residual flux increases during the MJO active phases and remains roughly unchanged during the MJO calm phases.

D. Effects of Low-Pass Filtering

We chose to smooth heat flux estimates with a 7-day low-pass filter to (i) quantify their averages within the active and calm phases, and (ii) minimize high-frequency variations at time scales shorter than days. Because the net surface heat flux shows an intraseasonal spectral peak around a 30-day period, i.e., associated with the MJO events, fluxes averaged over one fourth of the MJO period (~7 days) capture the intra-MJO variations. The 7-day low-pass filtered data

smears the effects of the two atmospheric Kelvin waves during the MJO2 active phase, which is not the primary focus of the present study.

VITA

Nan-Hsun Chi 紀南薰

Updated: November 2018

Contact Information

E-mail: nhchi@uw.edu

Education

University of Washington, Seattle, WA
M.S., Oceanography, 2013

National Taiwan University, Taipei, Taiwan
M.S., Atmospheric Sciences, 2010
B.A., Atmospheric Sciences, 2009

Selected Experience

Graduate Research Assistant, University of Washington
School of Oceanography, 09.2011 ~ 09.2018
Advisor: Dr. Ren-Chieh Lien and Dr. Eric A. D'Asaro

Research Assistant, National Taiwan University
Department of Atmospheric Sciences, 07.2010 ~ 07.2011
Advisor: Dr. I-I Lin

Refereed Publications

Chen, S., M. Flatau, T. G. Jensen, T. Shinoda, J. Cummings, J. Schmidt, P. May, M. Liu, P. E. Ciesielski, C. W. Fairall, R.-C. Lien, D. B. Baranowski, **N.-H. Chi**, S. de Szoeke, J. Edson (2015), A study of CINDY/DYNAMO MJO suppressed phase, J. Atmos. Sci., 72, 3755-3779.

Chi, N.-H., R.-C. Lien, E. A. D'Asaro, and B. B. Ma (2014), The surface mixed layer heat budget from mooring observations in the central Indian Ocean during Madden–Julian Oscillation events, J. Geophys. Res. Oceans, 119, 4638–4652.

Lin, I.-I., P. Black, J. F. Price, C.-Y. Yang, S. S. Chen, C.-C. Lien, P. Harr, **N.-H. Chi**, C.-C. Wu, and E. A. D'Asaro (2013), An ocean coupling potential intensity index for tropical cyclones, Geophys. Res. Lett., 40, 1878–1882.

Selective Presentations

Oceanic surface mixed layer salinity budget in the Central Equatorial Indian Ocean. Ocean Science Meeting, Portland, OR, 2018. Poster.
Oceanic surface mixed layer heat and salinity budget in the Central Equatorial Indian Ocean. American Meteorological Soceity Annual Meeting, Seattle, WA, 2017. Talk.
Surface mixed layer salinity budget in the Central Equatorial Indian Ocean. Ocean Science Meeting, New Orleans, LA, 2016. Talk.
Variability of heat and salinity budget in the Central Equatorial Indian Ocean. Physical oceanography Seminars, National Taiwan University, Taipei, Taiwan, 2016. Talk.
In-situ observation of surface mixed layer heat budget at Central Indian Ocean During MJOs. Physics of Oceans and Atmospheres Seminar, Oregon State University, Corvallis, OR, 2014. Talk.
In-situ observation of surface mixed layer heat budget at Central Indian Ocean During MJOs. Ocean Science Meeting, Honolulu, HI, 2014. Poster.
Variation of surface mixed layer heat budget during DYNAMO. MJO field data and science workshop, Kona, HI, 2013. Poster.
Variations of surface mixed layer heat budget in Central Indian Ocean during DYNAMO. AGU Fall meeting, San Francisco, CA, 2012. Talk.

DYNAMO moorings: Variations of surface mixed layer heat budget during MJOs. ONR DYNAMO Littoral Air-Sea Processes Department Research Initiative meeting, Boston, MI, 2012. Talk.

Teaching Experience

Teaching Assistant, University of Washington, Seattle, WA, 09.2018 ~ 12.2018
Methods of Oceanographic Data Analysis. Instructor: Stephen Riser

Teaching Assistant, University of Washington, Seattle, WA, 03.2018 ~ 06.2018
Physical Processes in the Ocean. Instructor: Curtis Duetsch
Teaching Assistant, University of Washington, Seattle, WA, 09.2015 ~ 12.2015, 01.2013 ~ 03.2013
Physical Processes in the Ocean. Instructor: Mitsuhiro Kawase
National Taiwan University, Taipei, Taiwan, 09.2009 ~ 06.2010
Laboratory of Synoptic Meteorology. Instructor: Cheng-Shang Lee

Fieldwork Experience

USA R/V Roger Revelle, DYANMO Moorings and Seaglider and EM-APEX floats Deployments. Darwin Australia to Phuket Thailand, 09.28,2011 ~ 09.26.2011.

Taiwan R/V Ocean Researcher II, ITOP XBT and CTD casts and launched weather balloons. Kaohsiung Taiwan to South China Sea to Kaohsiung Taiwan, 11.05.2011 ~ 11.07.2011.

Service

Reviewer
Journal of Geophysical Research-Oceans
Climate Dynamics